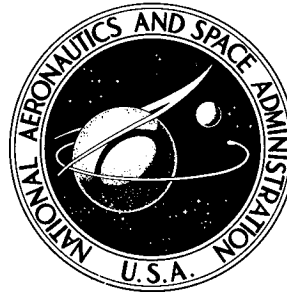


N72-23946

NASA TECHNICAL NOTE



NASA TN D-6792

NASA TN D-6792

**CASE FILE
COPY**

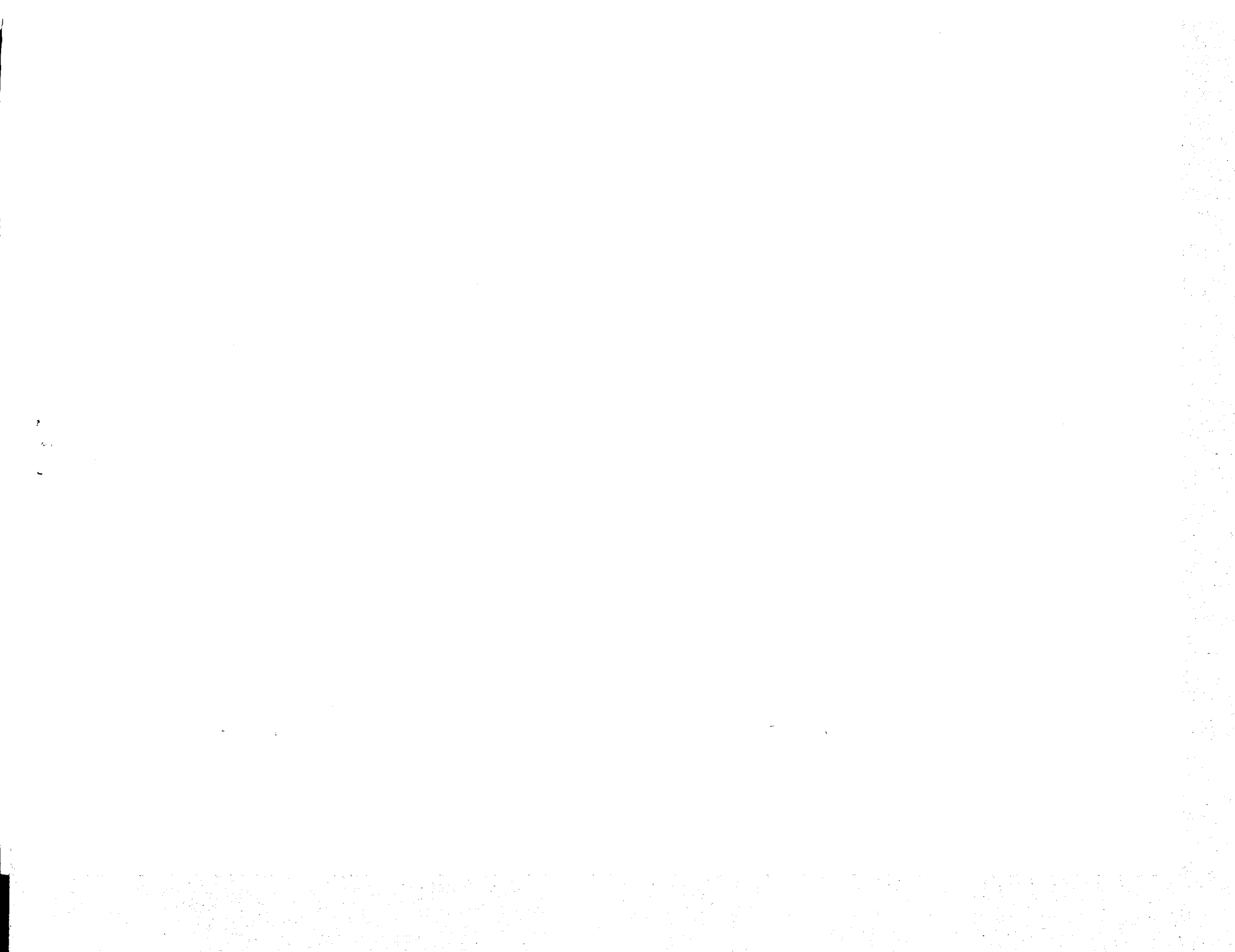
**THE AEROTHERMODYNAMIC ENVIRONMENT
OF THE APOLLO COMMAND MODULE
DURING SUPERORBITAL ENTRY**

by Dorothy B. Lee and Winston D. Goodrich

Manned Spacecraft Center

Houston, Texas 77058

NATIONAL AERONAUTICS AND SPACE ADMINISTRATION • WASHINGTON, D. C. • APRIL 1972



1. Report No. NASA TN D-6792	2. Government Accession No.	3. Recipient's Catalog No.
4. Title and Subtitle THE AEROTHERMODYNAMIC ENVIRONMENT OF THE APOLLO COMMAND MODULE DURING SUPERORBITAL ENTRY		5. Report Date April 1972
		6. Performing Organization Code
7. Author(s) Dorothy B. Lee and Winston D. Goodrich, MSC		8. Performing Organization Report No. MSC S-267
9. Performing Organization Name and Address Manned Spacecraft Center Houston, Texas 77058		10. Work Unit No. 914-11-20-10-72
		11. Contract or Grant No.
12. Sponsoring Agency Name and Address National Aeronautics and Space Administration Washington, D. C. 20546		13. Type of Report and Period Covered Technical Note
		14. Sponsoring Agency Code
15. Supplementary Notes The MSC Director waived the use of the International System of Units (SI) for this Technical Note, because, in his judgment, use of SI Units would impair the usefulness of the report or result in excessive cost.		
16. Abstract Aerothermodynamic measurements were obtained on two Apollo spacecraft during atmospheric entry at near-lunar-return velocities. Histories of measured pressure and of convective and radiative heating rates are compared with theoretical predictions and with wind-tunnel results. The comparisons show that pressures measured in the wind tunnel correspond to those measured in the flight environment of the entry face. Unexplained low pressures were obtained on the conical section. Measured radiative heating rates agree with predictions calculated for both visible and infrared radiation. Good agreement was found between convective heating rates measured in flight and predictions obtained by using cold wall theory adjusted for mass injection from the ablator.		
17. Key Words (Suggested by Author(s)) · Aerothermodynamics · Convective Heating Rate · Pressure · Apollo Flight Data		18. Distribution Statement
19. Security Classif. (of this report) None	20. Security Classif. (of this page) None	21. No. of Pages 87
		22. Price \$3.00



CONTENTS

Section	Page
SUMMARY	1
INTRODUCTION	1
SYMBOLS	2
CONFIGURATION AND FLIGHT TEST	3
Entry Vehicle	3
Instrumentation	3
Entry Trajectory	3
RESULTS AND DISCUSSION	5
Pressure	5
Radiative Heating Rates	6
Convective Heating Rates	7
CONCLUDING REMARKS	10
REFERENCES	11

TABLE

Table		Page
I	LOCATIONS AND RANGES OF PRESSURE TRANSDUCERS, CALORIMETERS, AND RADIOMETERS	4

FIGURES

Figure		Page
1	Apollo Block I entry vehicle	13
2	Sketch of Apollo command module, showing instrumentation locations	13
3	Schematic of the aerothermodynamic instruments. Dimensions are in inches	
	(a) Pressure transducer	14
	(b) Radiometer	14
	(c) Wafer calorimeter. (See ref. 4.)	14
	(d) Asymptotic calorimeter. (See ref. 3.)	14
4	Comparison of flight entry trajectories with heat shield design trajectories	15
5	Entry conditions of spacecraft 017 and 020	
	(a) Spacecraft 017	16
	(b) Spacecraft 020	17
6	Distribution of local to total pressure ratio around Apollo command module for $\alpha = 25^\circ$	18
7	Histories of pressures measured on spacecraft 017	
	(a) $Y_c = -2.0$ in., $Z_c = -2.0$ in., $S/R = 0.004$	19
	(b) $Y_c = 2.74$ in., $Z_c = 39.10$ in., $S/R = 0.513$	19
	(c) $Y_c = 1.50$ in., $Z_c = 55.02$ in., $S/R = 0.732$	20
	(d) $Y_c = 1.82$ in., $Z_c = 64.99$ in., $S/R = 0.872$	20
	(e) $Y_c = 1.50$ in., $Z_c = 71.82$ in., $S/R = 0.969$	21
	(f) $Y_c = -1.15$ in., $Z_c = 74.98$ in., $S/R = 1.038$	21
	(g) $Y_c = -10.59$ in., $Z_c = -48.90$ in., $S/R = -0.663$	22

Figure	Page
(h) Conical section	22
(i) Toroid	23
8 Comparison of spacecraft 017 flight measurement with wind-tunnel data for $\alpha = 25^\circ$	24
9 Histories of pressure measured on spacecraft 020	
(a) Aft compartment	25
(b) Windward conical section	28
(c) Yaw toroid and conical section	29
(d) Toroid	30
10 Radiative heating rates measured at the stagnation point of spacecraft 017 compared with theoretical predictions	31
11 Comparison of measured radiative heating rates on spacecraft 020 with theoretical predictions	
(a) $Y_c = -0.48$ in., $Z_c = 55.0$ in., $S/R = 0.727$	32
(b) $Y_c = 1.02$ in., $Z_c = -48.75$ in., $S/R = -0.643$	32
12 Wind-tunnel distribution of local heating rate for $\alpha = 25^\circ$ divided by zero angle-of-attack stagnation-point heating rate	33
13 Histories of high-range calorimeter wafer temperatures measured on spacecraft 017	
(a) Aft compartment	34
(b) Top four wafers of $Y_c = 4.23$ in., $Z_c = 55.16$ in., $S/R = 0.732$	36
(c) Top three wafers of $Y_c = -4.74$ in., $Z_c = -50.0$ in., $S/R = -0.663$	37
(d) Top three wafers of $Y_c = 50.0$ in., $Z_c = -1.5$ in., $S/R = 0.666$	38
14 Heating rates calculated from wafer calorimeter temperature measurements on spacecraft 017	
(a) $Y_c = -0.48$ in., $Z_c = 0.48$ in., $S/R = 0.004$	39
(b) $Y_c = 0$ in., $Z_c = 39.0$ in., $S/R = 0.512$	40
(c) $Y_c = 4.23$ in., $Z_c = 55.16$ in., $S/R = 0.732$	41
(d) $Y_c = 4.01$ in., $Z_c = 71.72$ in., $S/R = 0.969$	42
(e) $Y_c = 1.31$ in., $Z_c = 74.98$ in., $S/R = 1.038$	43

	(f) $Y_c = -4.74$ in., $Z_c = -50.0$ in., $S/R = -0.663$	44
	(g) $Y_c = 50.0$ in., $Z_c = -1.5$ in., $S/R = 0.666$, $\theta = 0^\circ$	45
	(h) $Y_c = 12.73$ in., $Z_c = -49.47$ in., $S/R = 0.671$, $\theta = 284^\circ$	46
15	High-range calorimeter wafer temperature measured on spacecraft 020	
	(a) $Y_c = -0.48$ in., $Z_c = 0.48$ in., $S/R = 0.004$	47
	(b) $Y_c = 0$ in., $Z_c = 39.0$ in., $S/R = 0.512$	47
	(c) Top wafer of $Y_c = 4.23$ in., $Z_c = 55.16$ in., $S/R = 0.732$	48
	(d) Second wafer of $Y_c = 4.23$ in., $Z_c = 55.16$ in., $S/R = 0.732$	48
	(e) Third wafer of $Y_c = 4.23$ in., $Z_c = 55.16$ in., $S/R = 0.732$	48
	(f) Fourth wafer of $Y_c = 4.23$ in., $Z_c = 55.16$ in., $S/R = 0.732$	49
	(g) $Y_c = 0$ in., $Z_c = 65.0$ in., $S/R = 0.865$	49
	(h) $Y_c = 4.01$ in., $Z_c = 71.72$ in., $S/R = 0.969$	50
	(i) $Y_c = 1.31$ in., $Z_c = 74.98$ in., $S/R = 1.038$	50
	(j) Top wafer of $Y_c = -4.74$ in., $Z_c = -50.0$ in., $S/R = -0.663$	51
	(k) Second wafer of $Y_c = -4.74$ in., $Z_c = -50.0$ in., $S/R = -0.663$	51
	(l) Third wafer of $Y_c = -4.74$ in., $Z_c = -50.0$ in., $S/R = -0.663$	52
	(m) Top wafer of $Y_c = 50.0$ in., $Z_c = -1.5$ in., $S/R = 0.666$, $\theta = 0^\circ$	52
	(n) Second wafer of $Y_c = 50.0$ in., $Z_c = -1.5$ in., $S/R = 0.666$, $\theta = 0^\circ$	53
	(o) Third wafer of $Y_c = 50.0$ in., $Z_c = -1.5$ in., $S/R = 0.666$, $\theta = 0^\circ$	53
	(p) $Y_c = 13.23$ in., $Z_c = -65.18$ in., $S/R = 0.893$	54
	(q) $Y_c = 12.73$ in., $Z_c = -49.47$ in., $S/R = -0.673$	54
16	Heating rates calculated from wafer calorimeter temperature measurements on spacecraft 020	
	(a) $Y_c = -0.48$ in., $Z_c = 0.48$ in., $S/R = 0.004$	55
	(b) $Y_c = 0$ in., $Z_c = 39.0$ in., $S/R = 0.512$	56
	(c) $Y_c = 4.23$ in., $Z_c = 55.16$ in., $S/R = 0.732$	57

Figure	Page
(d) $Y_c = 0$ in., $Z_c = 65.0$ in., $S/R = 0.865$	58
(e) $Y_c = 4.01$ in., $Z_c = 71.72$ in., $S/R = 0.969$	59
(f) $Y_c = -4.74$ in., $Z_c = -50.0$ in., $S/R = -0.663$	60
(g) $Y_c = 50.0$ in., $Z_c = -1.5$ in., $S/R = 0.666$, $\theta = 0^\circ$	61
(h) $Y_c = 12.73$ in., $Z_c = -49.47$ in., $S/R = -0.673$, $\theta = 284^\circ$. . .	62
 17 Asymptotic calorimeter measurements on spacecraft 017 compared with theoretical predictions	
(a) Windward conical section	63
(b) Toroid	65
(c) Leeward conical section	67
 18 Asymptotic calorimeter measurements on spacecraft 020 compared with theoretical predictions	
(a) Windward conical section	69
(b) Toroid	71
(c) Leeward conical section	73
 19 Photograph of dummy umbilical on spacecraft 017	77
 20 Photograph of recovered spacecraft 020 showing umbilical and astro sextant	78
 21 Heating-rate measurements on singularities of spacecraft 017	
(a) Umbilical cavity	79
(b) Umbilical frame	79
(c) Hatch gap	80

THE AEROTHERMODYNAMIC ENVIRONMENT OF THE APOLLO COMMAND MODULE DURING SUPERORBITAL ENTRY

By Dorothy B. Lee and Winston D. Goodrich
Manned Spacecraft Center

SUMMARY

Aerothermodynamic measurements were obtained on two Apollo spacecraft during atmospheric entry at near-lunar-return velocities. Histories of measured pressure and of convective and radiative heating rates are compared with theoretical predictions and with wind-tunnel results. The comparisons show that pressures measured in the wind tunnel correspond to those measured in the flight environment of the entry face. Unexplained low pressures were obtained on the conical section. Measured radiative heating rates agree with predictions calculated for both visible and infrared radiation. Good agreement was found between convective heating rates measured in flight and predictions obtained by using cold wall theory adjusted for mass injection from the ablator.

INTRODUCTION

The aerothermodynamic environment used in the design of the Apollo thermal protection system was based on theory and on wind-tunnel data. This predicted environment compared favorably with data obtained from four flight tests of Apollo unmanned vehicles. These tests were conducted for the purpose of evaluating the thermal protection system in flight. Aerothermodynamic measurements were made to assist in the thermal protection system evaluation. Because of the opportunity to obtain aerothermodynamic information on full-scale vehicles at orbital and superorbital velocities, an effort was made to analyze the measurements. Analysis of aerothermodynamic data obtained during the Apollo 1 and 3 missions, which attained orbital velocities, is reported in reference 1. Analysis of the aerothermodynamic data from the two instrumented spacecraft which entered the atmosphere at velocities equal to or near lunar return conditions is reported herein.

The first test at lunar return velocities (36 628 ft/sec) was conducted with spacecraft 017 on the Apollo 4 mission, which was the first to use the Saturn V launch vehicle. The spacecraft was launched from NASA Kennedy Space Center, Florida, on November 9, 1967, and was recovered in the Pacific Ocean near Hawaii after an 8-1/2-hour flight. The second test flight, launched on April 4, 1968, was conducted with spacecraft 020 on the Apollo 6 mission. The planned entry inertial velocity of 36 500 ft/sec was not achieved by spacecraft 020 because of the unsuccessful attempt

to reignite the Saturn IV engine. However, heat shield performance data and aerothermodynamic data were obtained at the entry velocity of 32 830 ft/sec.

Measurements of pressure and heating rates were obtained on spacecraft 017 and 020 with pressure transducers, radiometers, and surface-mounted calorimeters. The data were obtained at free-stream relative velocities between 35 300 and 3000 ft/sec on spacecraft 017 and between 31 600 and 2700 ft/sec on spacecraft 020. This report presents histories of the measured pressures and heating rates obtained at these lunar return conditions. The flight data are compared with theoretical predictions and with wind-tunnel results.

SYMBOLS

M_{∞}	free-stream Mach number
p	pressure, psia
p_t	stagnation pressure, psia
\dot{q}	heating rate, Btu/ft ² -sec
$\dot{q}_{t, \alpha=0}$	stagnation-point heating rate at zero angle of attack, Btu/ft ² -sec
\dot{q}_{WB}	heating rate adjusted for blowing, Btu/ft ² -sec
R	constant equal to one-half the maximum diameter, 6.417 feet
$R_{\infty, D}$	free-stream Reynolds number based on body diameter
$R_{l, x}$	local Reynolds number based on length from flight stagnation point
S	surface distance from center of aft compartment, feet
V_{∞}	free-stream velocity, ft/sec
X_c, Y_c, Z_c	command module body coordinates, inches
α	angle of attack, degrees
θ	angle about the command module X_c -axis, degrees

CONFIGURATION AND FLIGHT TEST

Entry Vehicle

The heat shield qualification flight tests were conducted with a Block I spacecraft configuration — a predecessor of the lunar mission spacecraft. A sketch of the entry vehicle is shown in figure 1. The heat shield or thermal protection system covers the entire command module and is divided into three parts: the aft compartment that is the blunt entry face, the crew and forward compartments that comprise the conical section, and a toroidal fairing between the aft compartment and the conical section.

Modifications made to the Block I design resulted in a Block II configuration designed for the lunar orbital rendezvous phase of the mission. The changes included (1) truncating the apex of the forward compartment to accommodate the docking capability and (2) removing the scimitar antennas and leeward umbilical housing. A comprehensive discussion of the Apollo design is given in reference 2. Some of the Block II singularities, such as the recessed umbilical and the astro sextant/telescope located on the windward conical section, were tested on spacecraft 017 and 020.

Instrumentation

Pressure transducers, radiometers, and surface-mounted calorimeters were installed on spacecraft 017 and 020 to measure the aerothermodynamic environment during atmospheric entry. The locations of these sensors, which were the same for both vehicles, are shown in figure 2. The sensor ranges and location identifications are given in table I. Schematic diagrams of the various sensors are shown in figure 3. Local pressures were measured through a small hole in the ablator that led to a strain-gage diaphragm pressure transducer located under the substructure. Radiometers, used to measure radiative heating rates, consisted of a thermopile behind a quartz window located at the bottom of a stepped hole in the ablator. Two types of calorimeters were used to measure total heat transfer rates. Asymptotic calorimeters, designed to measure heating rates below $50 \text{ Btu/ft}^2\text{-sec}$, were located on the toroid and the conical section. The design of these instruments is shown schematically in figure 3, and the principle of operation is discussed in reference 3. High-range slug calorimeters, developed specifically for the Apollo Program, were located on the aft compartment to measure heating rates greater than $50 \text{ Btu/ft}^2\text{-sec}$. The slug calorimeters consist of several graphite wafers that are stacked to allow continuous heating measurements during recession of the surrounding ablator. The detail of one such wafer unit is shown schematically in figure 3. The wafer temperature and the rate of change of temperature are used to determine the heat flux to the surface. Operation and design of the calorimeters are discussed in reference 4.

Entry Trajectory

Design of the Apollo thermal protection system was based on two design trajectories: an overshoot, long-range trajectory for the maximum heat load to the vehicle

TABLE I. - LOCATIONS AND RANGES OF PRESSURE TRANSDUCERS, CALORIMETERS, AND RADIOMETERS

Aft compartment									Conical section								
Pressure transducer			Wafer calorimeter			Radiometer			Pressure transducer			Calorimeter			Radiometer		
Y _c , in.	Z _c , in.	Range, psia	Y _c , in.	Z _c , in.	Range, °F	Y _c , in.	Z _c , in.	Range, Btu/ft ² -sec	X _c , in.	θ, deg	Range, psia	X _c , in.	θ, deg	Range, Btu/ft ² -sec	X _c , in.	θ, deg	Range, Btu/ft ² -sec
-2.0	-2.0	10	-0.5	0.5	5000				26.5	91.6	2	26.5	93.7	150			
2.7	39.1	10	0	39.0	5000				50.0	88.5	2	50.0	85.3	100	52.3	88.5	50
1.5	55.0	10	4.2	55.2	5000	-0.5	55.0	1200	83.4	86.9	2	83.4	82.6	100			
1.8	65.0	10	0	65.0	5000				104.0	94.8	2	104.0	101.5	75			
1.5	71.8	10	4.0	71.7	5000				26.3	135.8	2	26.3	137.9	100			
-1.2	75.0	5	1.3	75.0	5000							78.9	137.0	75			
-10.6	-48.9	5	-4.7	-50.0	5000	1.0	-48.8	1200	18.2	176.6	2	18.2	179.4	75			
			12.7	-49.5	5000				18.5	229.5	2	18.5	225.1	75			
			13.2	-65.2	5000				18.5	272.3	2	18.5	264.0	75			
			50.0	-1.5	5000							52.5	179.0	50			
			-59.6	31.9	5000				78.9	185.0	2	78.9	189.0	50			
												104.0	191.5	50			
												50.0	228.8	50			
												78.9	226.2	50			
												50.0	272.0	50	45.0	270.1	50
									78.9	263.9	2	78.9	267.8	50			
												104.0	274.8	50			
												60.0	268.0	10			
												65.0	278.0	10			
												35.0	90	150			
												43.0	90	150			

and an undershoot, high-acceleration trajectory for maximum convective and radiative heat transfer rates to the ablator. Heat shield qualification tests of spacecraft 017 and 020 were conducted in the middle of the design entry corridor to subject the command module to heat loads and heat rates sufficiently high to qualify the heat shield with one mission. (Spacecraft 020 was originally scheduled as a backup mission.) Figure 4 shows both the qualification trajectories and the design trajectories. The theoretical heat load, calculated for a reference location ($S/R = 0.9875$) on spacecraft 017, is 93 percent of the overshoot trajectory heat load, and the maximum heat rate is 62 percent of that calculated for the undershoot trajectory. Histories of the entry parameters of spacecraft 017 and 020 are shown in figure 5. Although spacecraft 020 entered at a velocity 3700 ft/sec less than planned, the test provided valuable heat shield performance data.

RESULTS AND DISCUSSION

Pressure

The two spacecraft were balanced with a center-of-gravity offset such that they entered the atmosphere at a 25° angle of attack (ref. 5). Because an angle-of-attack attitude results in a nonaxisymmetric flow field that is difficult to analyze, wind-tunnel data were necessary for a preflight definition of the local environment around the vehicle. The wind-tunnel pressure values, presented in reference 6 as a ratio of the local pressure to the stagnation pressure behind a normal shock, are given in figure 6 for the Apollo command module at 25° angle of attack. Estimates of the flight pressures were made by using these ratios and normal-shock calculations of total pressure for the actual flight conditions.

Spacecraft 017. - Histories of the pressures measured on spacecraft 017 during entry are compared in figure 7 with those calculated from wind-tunnel measurements. Good agreement can be seen between the flight data and the estimates for the aft compartment measurements (figs. 7(a) to 7(g)). The data obtained on the conical section (figs. 7(h) and 7(i)), however, are considerably lower (about one-third) than the wind-tunnel values during the first peak. The first peak corresponds to the time of maximum heating and thus may be influenced by mass injection into the boundary layer from the aft compartment ablator.

The pressure distribution measured on the aft compartment is compared in figure 8 with the 25° angle-of-attack wind-tunnel distribution. The flight data, shown as bars, were normalized by the maximum pressure measurement obtained at $S/R = 0.732$. The bars indicate the range of pressure ratios when the measured values were at least 50 percent of the full-scale instrument reading. The good agreement between the flight data and the wind-tunnel results supports the use of wind-tunnel data to define the flight pressure environment.

Spacecraft 020. - Histories of the pressures measured on spacecraft 020 are shown in figure 9 and compared with wind-tunnel measurements. As observed with spacecraft 017 flight data, good agreement exists between spacecraft 020 pressure data

and wind-tunnel-based predictions for the aft compartment. However, the flight data are as low as one-half the predictions for the conical section during the time of peak heating.

The pressure deviations on spacecraft 017 and 020 were observed to be directly proportional to the heating associated with their respective trajectories; the higher velocity entry of 017 produced the greater deviation from prediction. This deviation indicates, qualitatively at least, the influence of boundary-layer mass injection on the aerothermodynamic environment of the vehicle.

Radiative Heating Rates

Four radiometers were mounted in each spacecraft — one at the stagnation point, one at the mid lee side of the entry face ($S/R = -0.663$), and two on the conical section (one on the windward side and one on the lee side). Those on the conical section showed no discernible response, which confirmed the prediction of negligible air and ablation product radiation to the conical section. Radiative measurements are presented in this report for completeness of data presentation only.

Spacecraft 017. - The radiometer, located on the lee side of the aft compartment on spacecraft 017, was inoperative at the time of launch, and no data were obtained. However, the radiometer at the stagnation point functioned properly. The stagnation-point radiometer, which had a view angle of 9° , measured only the visible and infrared radiation intensities, including the nonequilibrium intensities. The measured intensities were converted to surface heating rates, by using the ratios of theoretical heating rates and theoretical intensities. A history of the stagnation-point radiative flight measurement is compared with predicted values in figure 10. The analysis assumes that the stagnation-point standoff distance varies like that of a sphere whose radius is 10 feet, which corresponds to the normal shock conditions on the command module at $\alpha = 25^\circ$. Except for a discrepancy at peak heating and after 30 050 seconds, the flight data are in good agreement with predictions. The calculations of equilibrium radiation characteristics of air are based on the theory of reference 7 and include nonadiabatic or radiation cooling effects. The nonequilibrium radiation predictions are based on (1) empirical fits to ground data, falling approximately midway between the data of Allen (ref. 8) and Page et al. (ref. 7), and (2) the first data period of the fire I (ref. 9) and fire II (ref. 10) flight measurements. The nonequilibrium radiation calculations include both binary scaling and consideration of collision limiting.

The discrepancy between the spacecraft 017 flight data and predictions is attributed to the performance characteristics of the radiometer. While a preflight calibration of the radiometer was used for data reduction, an experimental program was conducted in the NASA Manned Spacecraft Center Entry Materials Evaluation Facility to investigate the effects of the ablator material on the sensor, as well as to gage the performance characteristics of the sensor. Two-inch-diameter radiometer models were mounted in Apollo ablator material and subjected to heat pulses simulating a portion of the flight environment. The models were exposed to radiative heating emitted from the end of a constricted arc column. A prominent dip similar to that measured in flight during peak heating was observed in the postflight test. This decrease in intensity is attributed to the attenuation of the infrared wavelengths during the temporary

formation of relatively cool ablation products within the radiometer cavity. When the cavity was heated, the attenuation decreased and the radiometer measured the expected intensity level. The arc jet models exhibited a drift behavior similar to that observed in flight after 30 050 seconds. This phenomenon was also attributed to the temperature excursion of the ablator material that occurred when a change in the radiometer body temperature caused a change in the thermopile heat flux.

Spacecraft 020. - The low entry velocity of spacecraft 020 resulted in radiative heating predictions that were an order of magnitude lower than those for a lunar return velocity. Likewise, the level of the measurements obtained on the aft compartment was low. The data, which are shown in figure 11, had a noise level that was as large as the magnitude of the measurements. A postflight inspection of the radiometer located at the stagnation point revealed a small obstruction in the radiometer port. The obstruction influenced the measurement and may have been the cause of an inconsistent trend between the measured and the predicted heating rates seen in figure 11(a).

Convective Heating Rates

As with the pressures, heating rates to the Apollo configuration also were obtained in wind-tunnel tests (refs. 6 and 11). Figure 12 shows the distribution of the wind-tunnel data measured at $\alpha = 25^\circ$ referenced to the measured zero-angle-of-attack stagnation-point value. The wind-tunnel data were used with the stagnation-point theory of reference 12 to predict the cold wall laminar heating rates to the command module during entry. The stagnation-point theory of reference 12 is based on the Apollo command module radius of 6.417 feet and is adjusted for the spherical-segment shape of the spacecraft according to reference 13. Turbulent heating to the aft compartment and the toroid was estimated by using the theory advanced in reference 14 where the ratio of turbulent to laminar heating is expressed as

$$\frac{\dot{q}_{\text{turbulent}}}{\dot{q}_{\text{laminar}}} = 0.055(R_{t,x})^{0.301} \quad (1)$$

No turbulent flow was predicted to occur on the conical section of spacecraft 017 and 020 because of the relatively low local Reynolds number in this region. The local Reynolds number was calculated with the assumption of an equilibrium isentropic expansion from stagnation conditions behind the normal shock to the local pressures obtained from figure 6. Transition from laminar to turbulent flow was originally predicted to occur at a local Reynolds number of 150 000 in attached flow and at a local Reynolds number of 20 000 in separated flow. Because the data of reference 1 suggested that transition might occur at a Reynolds number lower than 150 000 in the attached flow regions, a value of 80 000 was selected to predict the heating rates.

Aft compartment measurement. - Eleven wafer calorimeters were located on the aft compartment of both spacecraft. Three of the calorimeters provided simultaneous temperature measurements of the top three or four wafers. Only the top wafer temperature was measured for the other calorimeters. The lack of meaningful data from the

wafer calorimeters on the two orbital flights (ref. 1) necessitated a redesign of the sensor. The redesign was completed in time sufficient only for installation and not for preflight calibration. Therefore, heating rates were determined from the wafer temperature measurements with the use of an empirical fit to postflight ground test data. Calibration of the sensors involved ground tests in which the temperature measured in flight was used to control the heat input. The heat flux to the wafer was also monitored with a laboratory standard calorimeter. An energy balance was applied to the wafer-thermocouple assembly that took into account conductive losses and property uncertainties. The losses and uncertainties were as much as 70 percent of the total measurements for the low heating rates and generally 40 to 50 percent of the total for the high heating rates.

Histories of the wafer temperatures measured on spacecraft 017 are given in figure 13. Heating rates were determined from these temperatures until the data became erratic (around 2000° F). The calculated heating rates are shown in figure 14. At most measurement locations, there is good agreement between the flight data and the theoretical radiative plus laminar convective rates adjusted for blowing. Figure 14 also shows the cold wall theoretical convective rates plus radiative rates. The cold wall rates were used as an input to a charring and ablation computer program, designated STAB II (ref. 15), to calculate the amount of heat blockage caused by ablation products injected into the boundary layer.

The wafer temperature measurements obtained on spacecraft 020 are given in figure 15. The heating rates determined from these temperature measurements are compared with theory in figure 16. Some of the wafer temperature measurements on spacecraft 020 had a bias, as much as 200° F, which was corrected to an initial value of 60° F before calculating the heating rates.

Conical section heating rate measurements. - Histories of the heating rates measured with the asymptotic calorimeters on the conical section of spacecraft 017 and 020 are shown in figures 17 and 18, respectively. The data have been corrected to account for a nonablating sensor embedded in the ablating material as presented in reference 16 and for nonisothermal wall effects as discussed in reference 17. These corrections were found to be between 6 to 12 percent of the measured value near the toroid and 2 to 4 percent of the measured value near the apex. Cold wall predictions and predictions adjusted for blowing for the charred regions are included in figures 17 and 18 for comparison with the flight data. For most windward conical locations, the theory overpredicts the measurements. Because flight heating rate and pressure measurements were considerably lower than the predictions on the two spacecraft, the cold wall theoretical heating rates were adjusted to account for the growth of a laminar boundary layer by $\sqrt{p_{\text{measured}}/p_{\text{predicted}}}$. The adjustment lowered the cold wall heating predictions by 60 to 70 percent, which brought the \dot{q}_{WB} into agreement with the measured rates. It must be noted that the phenomenon responsible for the disagreement between wind-tunnel and flight-pressure distributions on the conical section has not been identified. However, the postulate of upstream blowing seems to be sound. The apparent importance of this phenomenon on the accuracy of the heating predictions should make identification and qualification a challenge to the analyst.

The measured heating rates on the toroid were the same level as the cold wall predictions. Thus, when the predictions were adjusted for blowing, they were lower than the measurements. (See figs. 17(b) and 18(b).) However, the ablator temperatures that were predicted with the adjusted heating rates were higher than the thermocouple measurements located in the vicinity of the calorimeters. The inconsistency is unresolved and requires further analysis for resolution. The ablator data analysis is presented in reference 18.

The lee side of the conical section is in separated flow where the heating rate measurements agree well with wind-tunnel data, which indicated that separated flow heating rates were approximately 2 percent of the Apollo stagnation-point theoretical heating rates. In some locations, measured rates were as low as 1 percent of the stagnation-point theory. One percent of the Apollo stagnation-point theory corresponds to 0.27 percent for a 1-foot-radius-sphere stagnation-point theory. No effects of protuberances were observed, and only momentary responses to reaction control engine firings were observed. These firings resulted in negligible heat loads to the affected areas.

Block II singularities investigated on spacecraft 017 and 020 were the recessed umbilical and the hatch door slots, both of which were simulated. Heating rates in and near these singularities were measured with asymptotic calorimeters. Two calorimeters were located on the umbilical frame and the umbilical cavity as shown in figure 19. Two calorimeters were installed in the gap of the hatch door, which is located on the lee side of the conical section. The astro sextant/telescope area was instrumented only with thermocouples; the data from this region are discussed in reference 18. Figure 20 shows the dummy umbilical and astro sextant/telescope on the recovered spacecraft 020.

The heating rates measured on the umbilical and hatch gap of spacecraft 017 are compared in figure 21 with smooth-body predictions for the same locations. The umbilical cavity measurement is significantly less than the smooth-body prediction. The umbilical frame measurement, located downstream of the cavity, is as much as twice the measurement located 7 inches downstream at $X_c = 50$ (fig. 17(a)). The predicted laminar heating for the hatch gap is based on 1 percent of the stagnation-point theory, and the measurements are approximately one-tenth of the predictions.

In general, wind-tunnel-based predictions for the aft compartment and leeward conical sections adequately describe the corresponding spacecraft flight environments. The radiative heating rate flight data are in good agreement with predictions calculated for the visible and infrared radiation, and the convective heating rates measured on the aft compartment and the windward conical section in flight agree with cold wall theory adjusted for blowing. Heating rates measured in and around surface singularities are not severe when compared to undisturbed values, and trends are as expected.

The pressure measurements made on the windward conical section, which is assumed to be in attached flow, are significantly lower than predicted and are presumed to be influenced by mass injection into the boundary layer from the aft compartment.

CONCLUDING REMARKS

Measurements of pressure and heating rates were made on Apollo entry vehicles in flight at near-lunar-return velocities. Comparisons of the flight measurements with theoretical predictions and with wind-tunnel results yield the following observations.

1. Wind-tunnel measurements provide a good description of the pressure on the entry face during hypersonic flight.
2. Measured radiative heating rates on the entry face agree with predictions calculated for the visible and infrared radiation.
3. No radiative heating was experienced on the conical section.
4. Convective heating rates on the entry face agree with cold wall theory adjusted for blowing.
5. Convective heating rates in the charred regions on the conical section agree with the theoretical predictions lowered by $\sqrt{p_{\text{measured}}/p_{\text{predicted}}}$ and then adjusted for blowing. The phenomenon responsible for lower pressures and heating to this region can be attributed to upstream blowing.
6. Heating rates measured in the separated regions of the conical section agree with predictions based on 1 percent, and in some regions 2 percent, of the Apollo stagnation-point theory.

Manned Spacecraft Center
National Aeronautics and Space Administration
Houston, Texas, January 28, 1972
914-11-20-10-72

REFERENCES

1. Lee, Dorothy B. ; Bertin, John J. ; and Goodrich, Winston D. : Heat-Transfer Rate and Pressure Measurements Obtained During Apollo Orbital Entries. NASA TN D-6028, 1970.
2. Erb, R. Bryan; Lee, Dorothy B. ; Weston, Kenneth C. ; and Greenshields, David H. : Aerothermodynamics — The Apollo Experience. Proceedings of the 1967 Heat Transfer and Fluid Mechanics Institute, June 19-21, 1967.
3. Grimaud, John E. ; and Tillian, Donald J. : Heat Transfer Rate Measurement Techniques in Arc-Heated Facilities. Paper presented to ASME 88th Winter Annual Meeting and 2nd Energy Systems Exposition (Pittsburgh, Pa.), Nov. 12-17, 1967.
4. Yanowitz, Herbert; and Beckman, Paul: A Heat-Flux Gage for Use on Recessive Surfaces. ISA Transactions, vol. 6, no. 3, July 1967, pp. 188-193.
5. Hillje, Ernest R. : Entry Aerodynamics at Lunar Return Conditions Obtained From the Flight of Apollo 4 (AS-501). NASA TN D-5399, 1969.
6. Bertin, John J. : The Effect of Protuberances, Cavities, and Angle of Attack on the Wind-Tunnel Pressure and Heat-Transfer Distribution for the Apollo Command Module. NASA TM X-1243, 1966.
7. Page, William A. ; Compton, Dale L. ; Borucki, William J. ; Ciffone, Donald L. ; and Cooper, David M. : Radiative Transport in Inviscid Nonadiabatic Stagnation-Region Shock Layers. AIAA 3rd Thermophysics Conference (Los Angeles, Calif.), June 24-26, 1968.
8. Allen, R. A. : Air Radiation Graphs: Spectrally Integrated Fluxes Including Line Contributions and Self Absorption. Avco-Everett Research Rept. 230, Sept. 1965.
9. Dingeldein, R. C. : Flight Measurements of Reentry Heating at Hyperbolic Velocity (Project Fire). NASA TM X-1053, 1965.
10. Cauchon, D. L. : Radiative Heating Results From the Fire II Flight Experience at a Reentry Velocity of 11.4 Kilometers Per Second. NASA TM X-1402, 1967.
11. Bertin, John J. : Wind-Tunnel Heating Rates for the Apollo Spacecraft (U). NASA TM X-1033, 1965.
12. Detra, R. W. ; Kemp, N. H. ; and Riddell, F. R. : Addendum to "Heat Transfer to Satellite Vehicles Reentering the Atmosphere." Jet Propulsion, vol. 27, no. 12, Dec. 1957, pp. 1256-1257.
13. Stoney, William E. , Jr. : Aerodynamic Heating of Blunt Nose Shapes at Mach Numbers up to 14. NACA RM L58E05a, 1958.
14. Van Driest, E. R. : On Skin Friction and Heat Transfer Near the Stagnation Point. NAA Rept. AL-2267, Mar. 1956.

15. Curry, Donald M. : An Analysis of a Charring Ablation Thermal Protection System. NASA TM X-64429, 1970.
16. Hearn, L. F. ; Chin, J. H. ; and Woodruff, L. W. : Study of Aerothermodynamic Phenomena Associated With Reentry of Manned Spacecraft. NASA CR-65368, 1966.
17. Woodruff, L. W. ; Hearn, L. F. ; and Keliher, T. J. : Interpretation of Asymptotic Calorimeter Measurements. AIAA J., vol. 4, no. 4, Apr. 1967, pp. 795-797.
18. Curry, Donald M. ; and Stephens, Emily W. : Apollo Ablator Thermal Performance at Superorbital Entry Velocities. NASA TN D-5969, 1970.

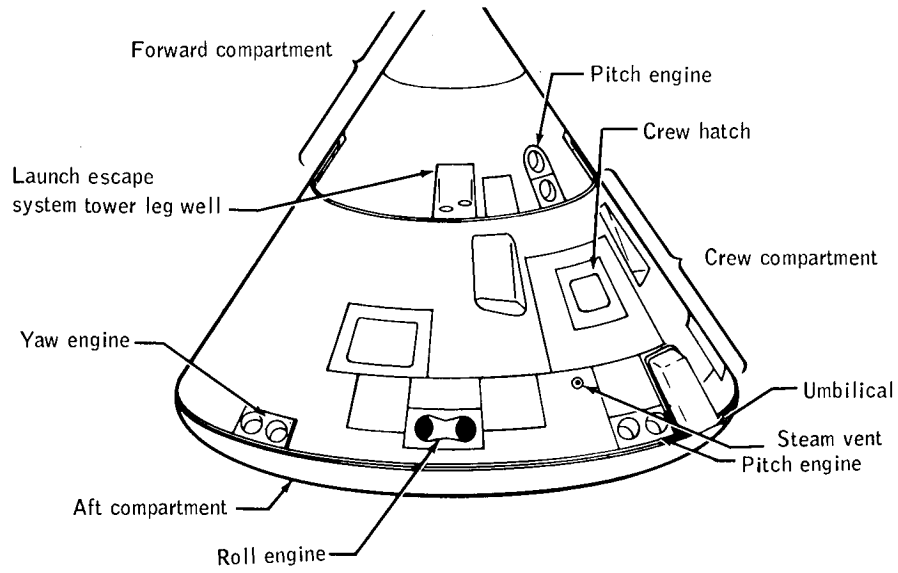


Figure 1. - Apollo Block I entry vehicle.

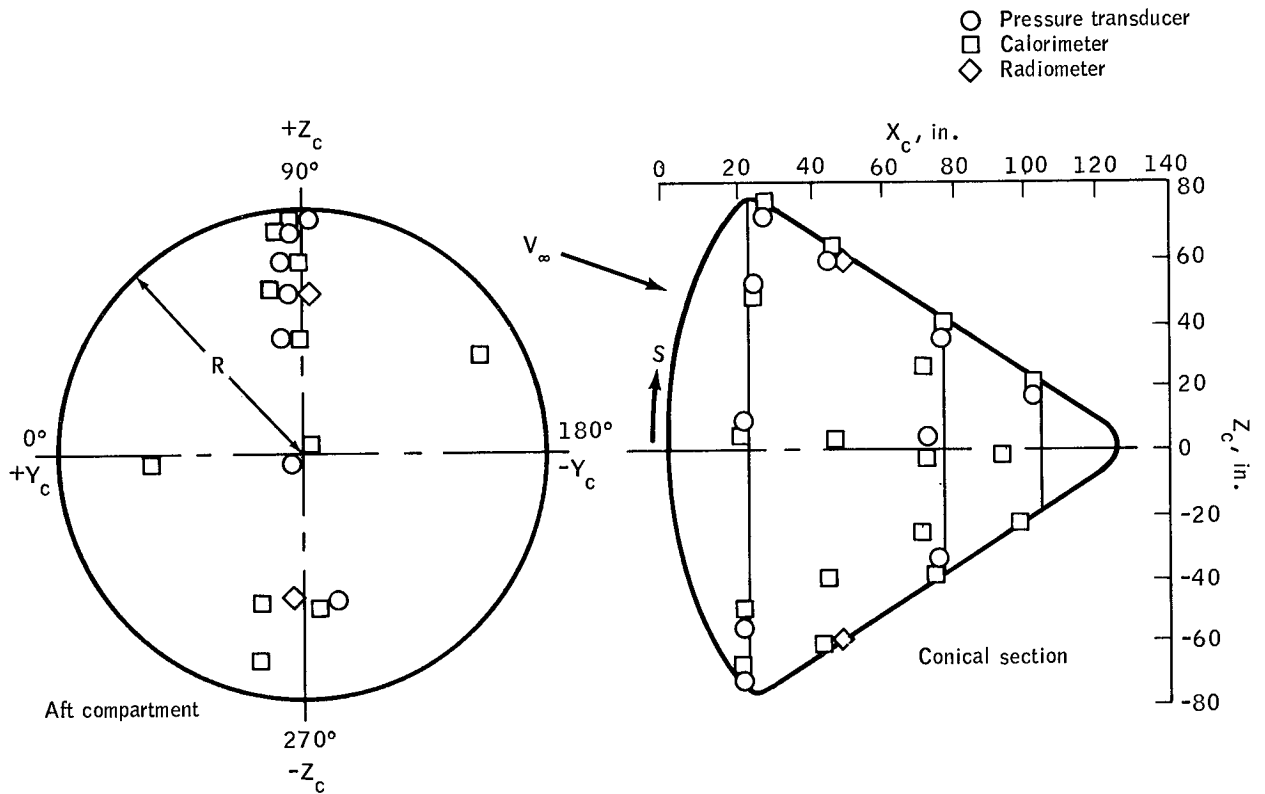
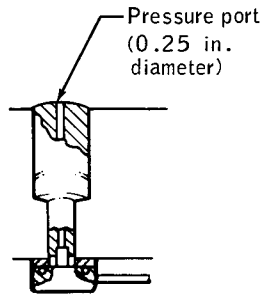
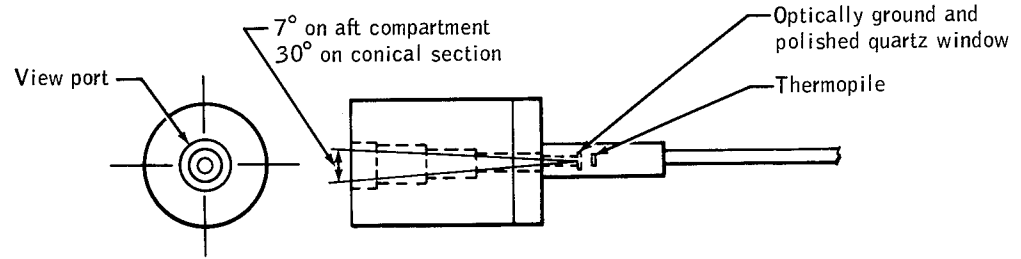


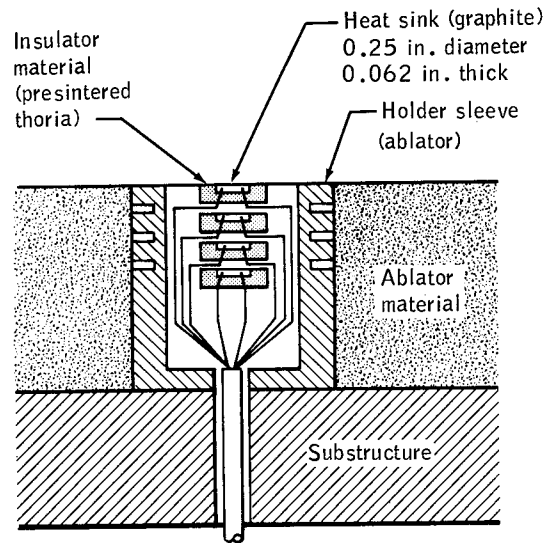
Figure 2. - Sketch of Apollo command module, showing instrumentation locations.



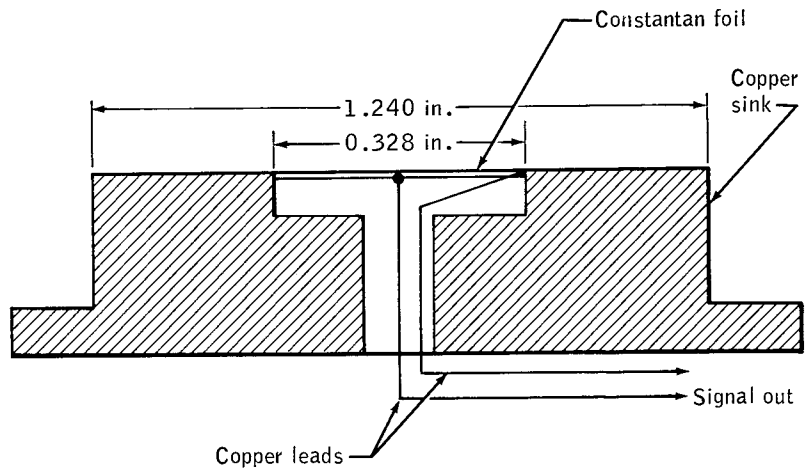
(a) Pressure transducer.



(b) Radiometer.



(c) Wafer calorimeter. (See ref. 4.)



(d) Asymptotic calorimeter. (See ref. 3.)

Figure 3. - Schematic of the aerothermodynamic instruments. Dimensions are in inches.

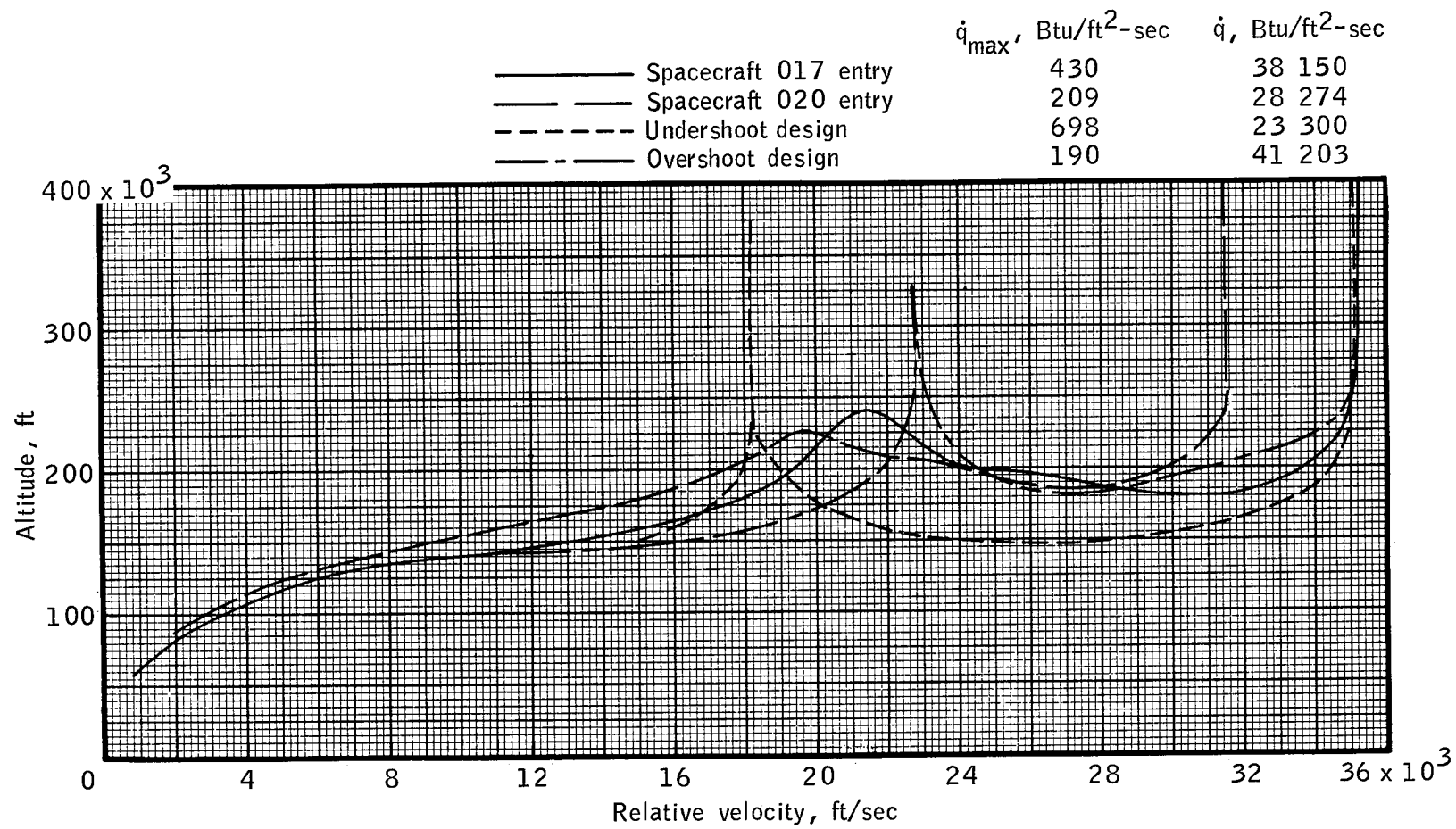
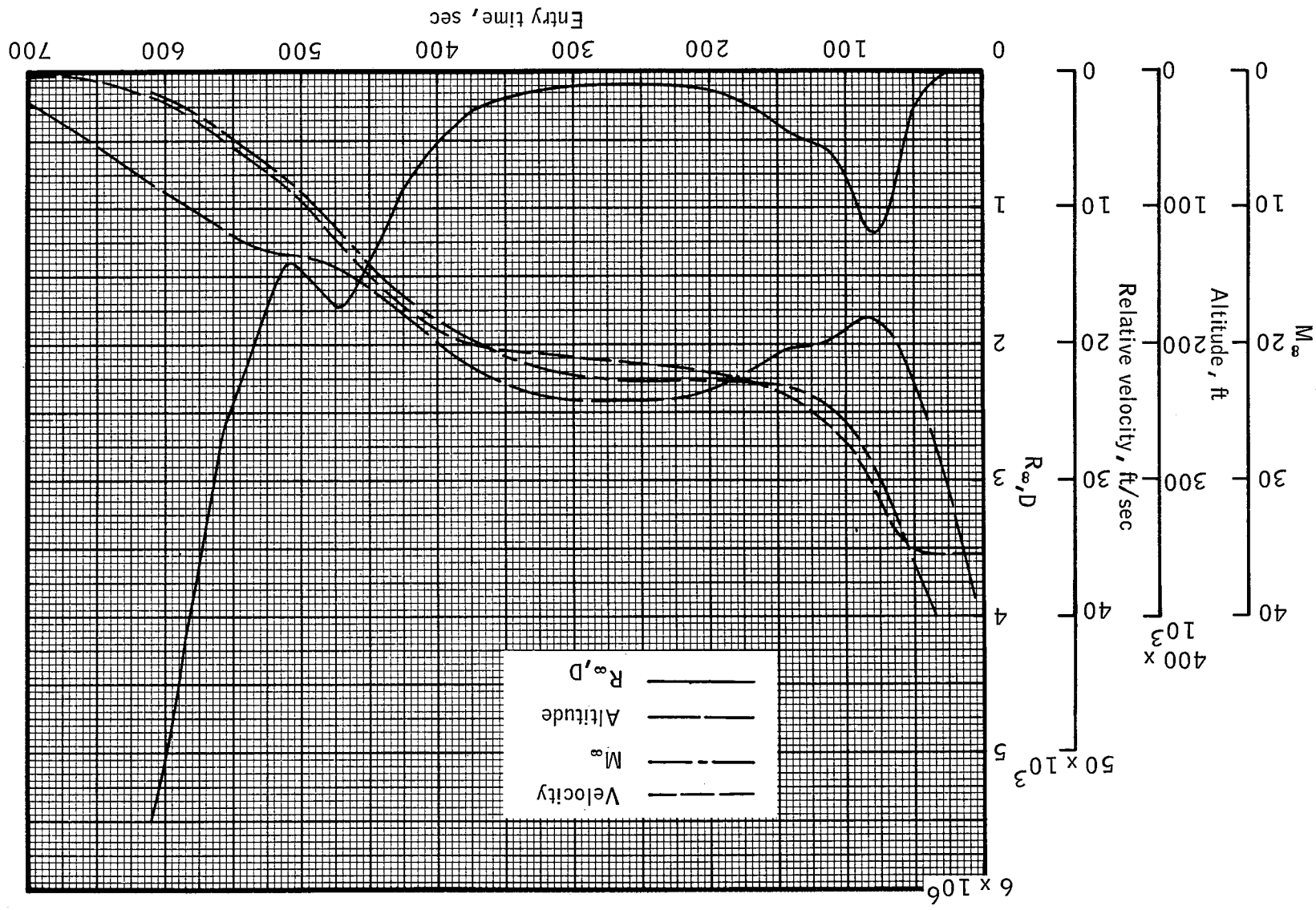


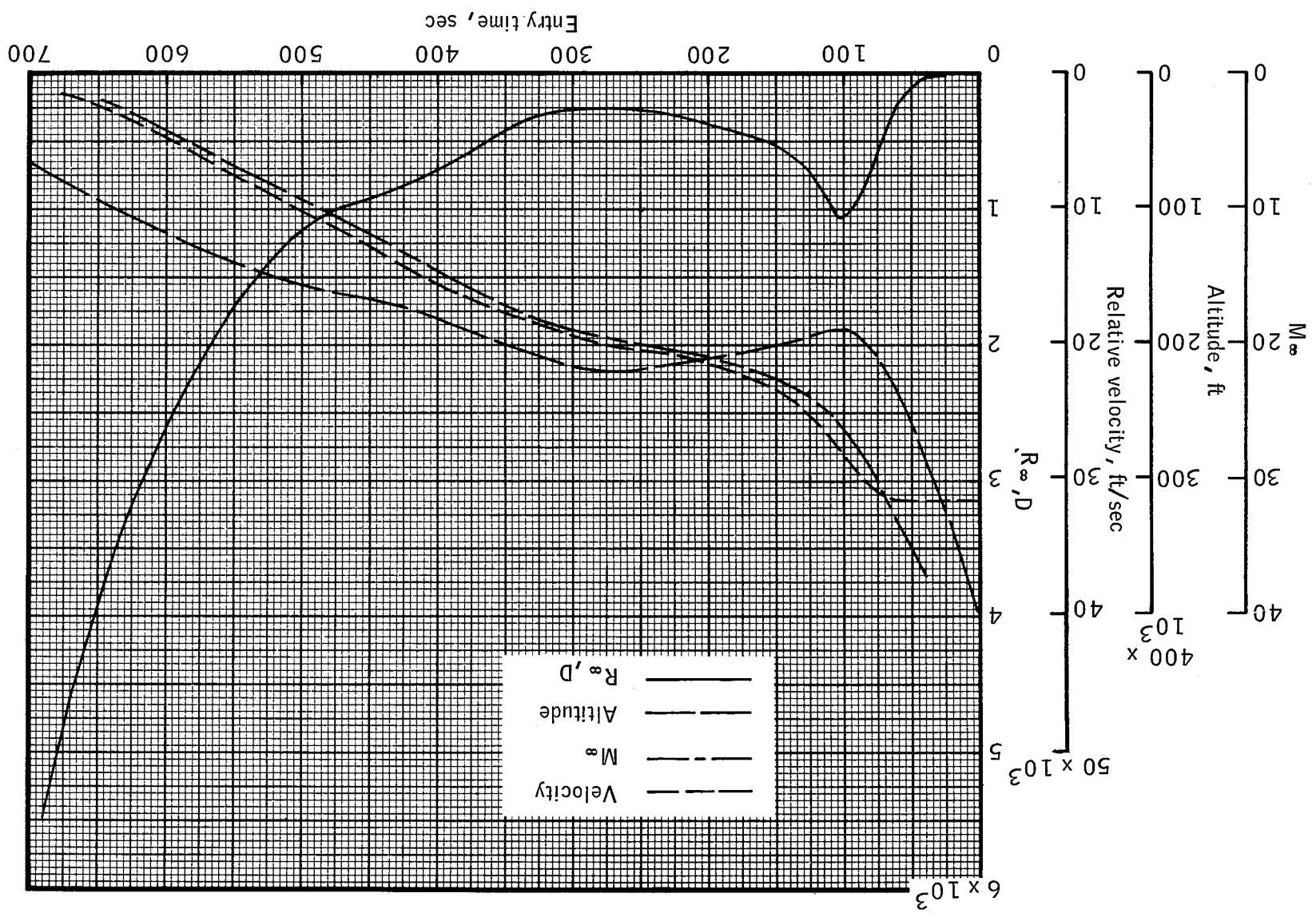
Figure 4. - Comparison of flight entry trajectories with heat shield design trajectories.



(a) Spacecraft 017.

Figure 5. - Entry conditions of spacecraft 017 and 020.

Figure 5. - Concluded.
 (b) Spacecraft 020.



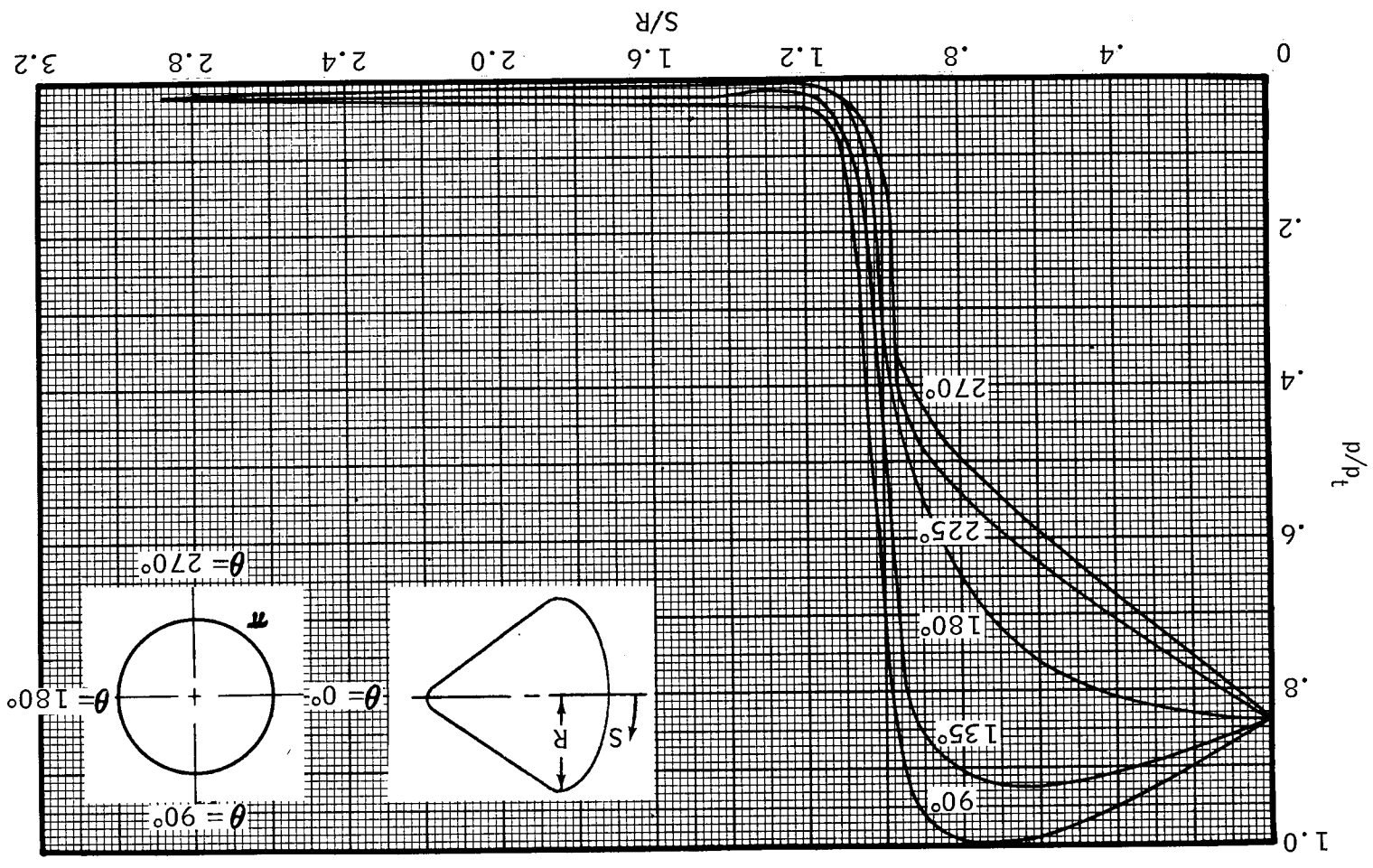
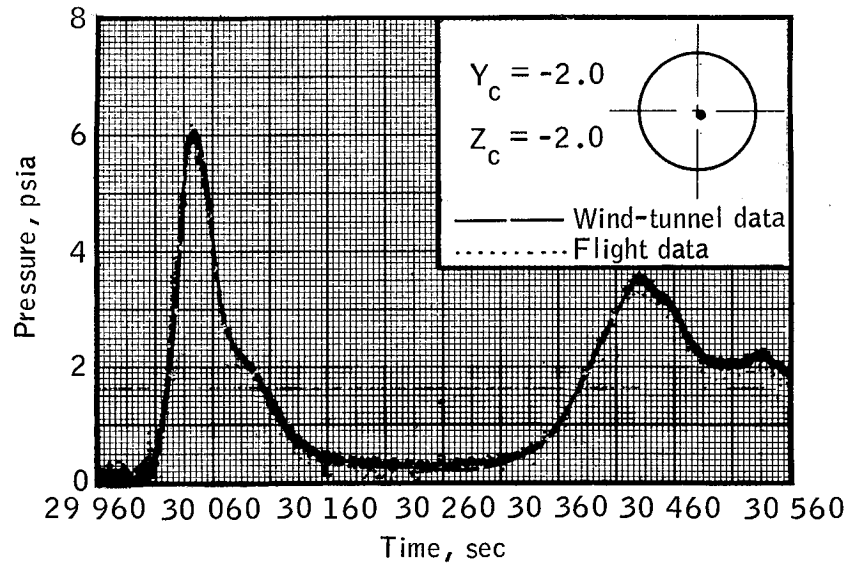
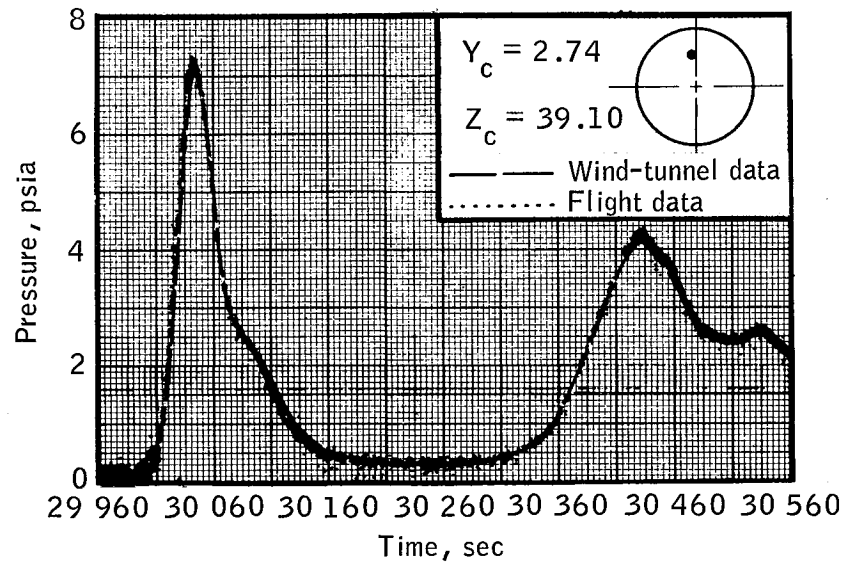


Figure 6. - Distribution of local to total pressure ratio around Apollo command module for $\alpha = 25^\circ$.

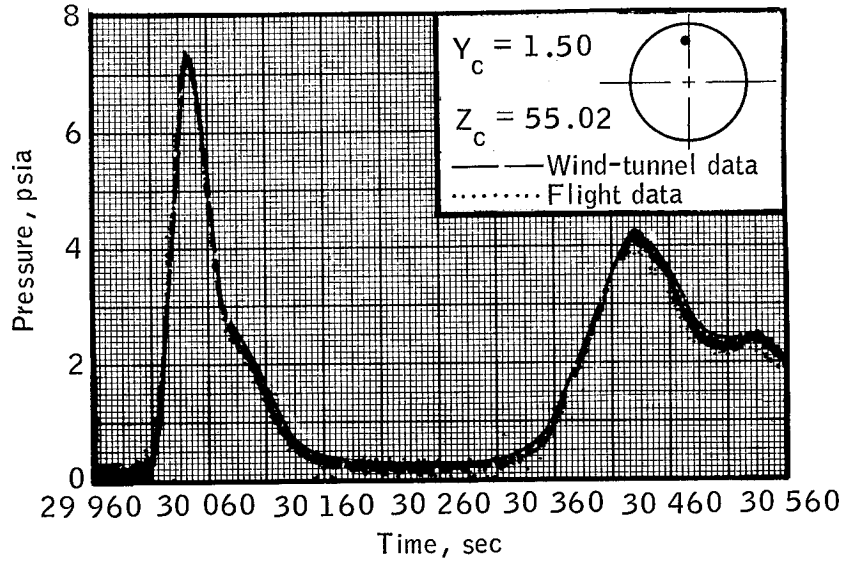


(a) $Y_c = -2.0$ in., $Z_c = -2.0$ in., $S/R = 0.004$.

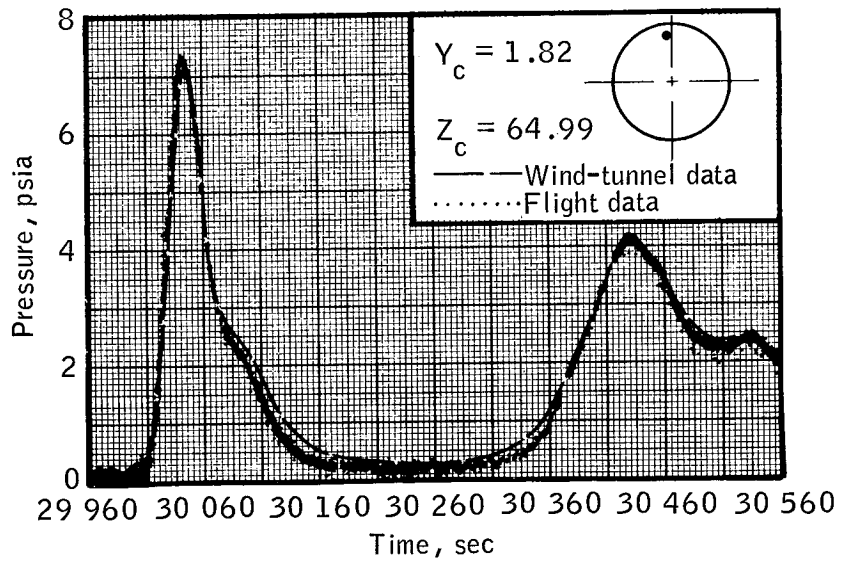


(b) $Y_c = 2.74$ in., $Z_c = 39.10$ in., $S/R = 0.513$.

Figure 7. - Histories of pressures measured on spacecraft 017.

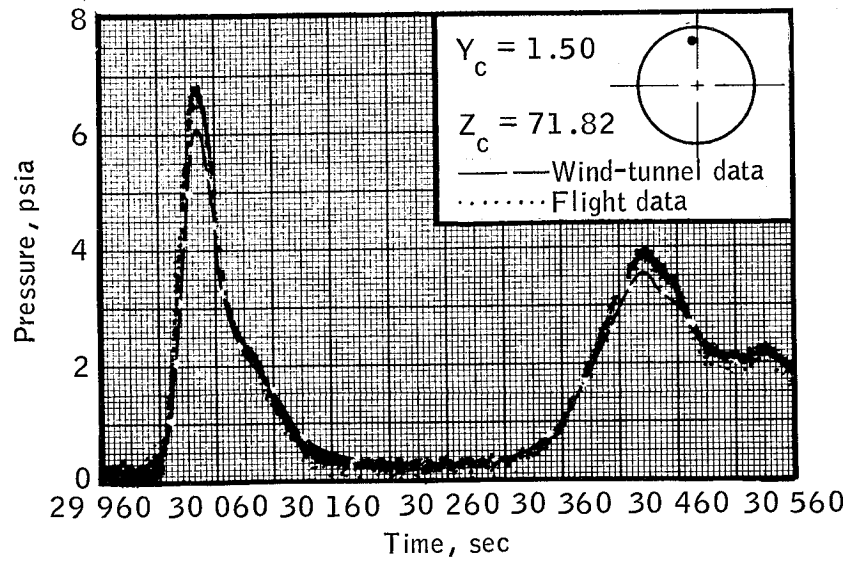


(c) $Y_c = 1.50$ in., $Z_c = 55.02$ in., $S/R = 0.732$.

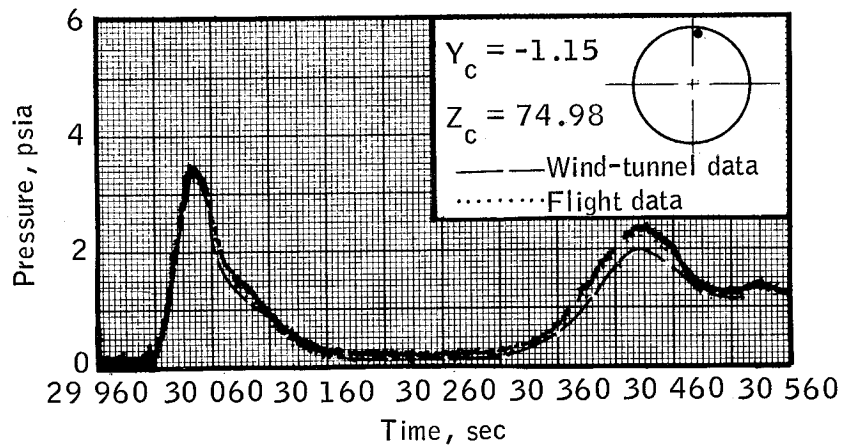


(d) $Y_c = 1.82$ in., $Z_c = 64.99$ in., $S/R = 0.872$.

Figure 7. - Continued.

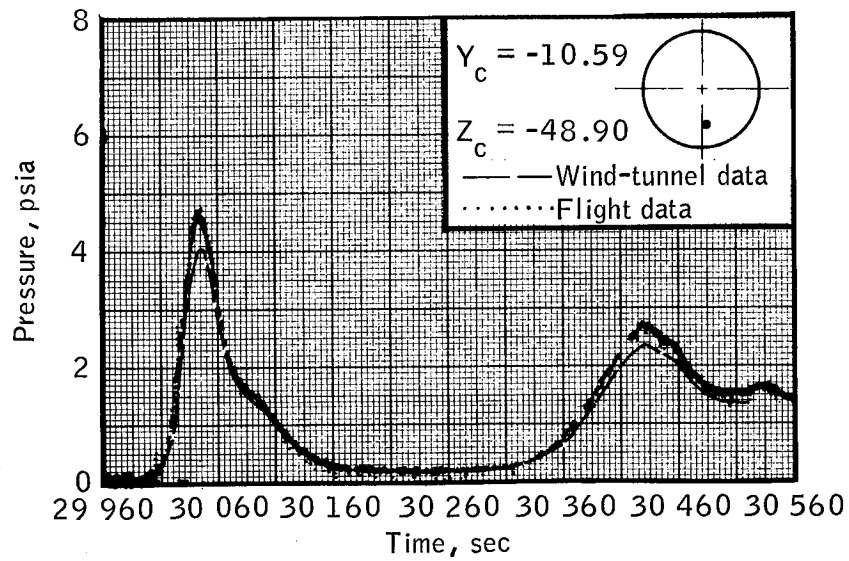


(e) $Y_c = 1.50$ in., $Z_c = 71.82$ in., $S/R = 0.969$.

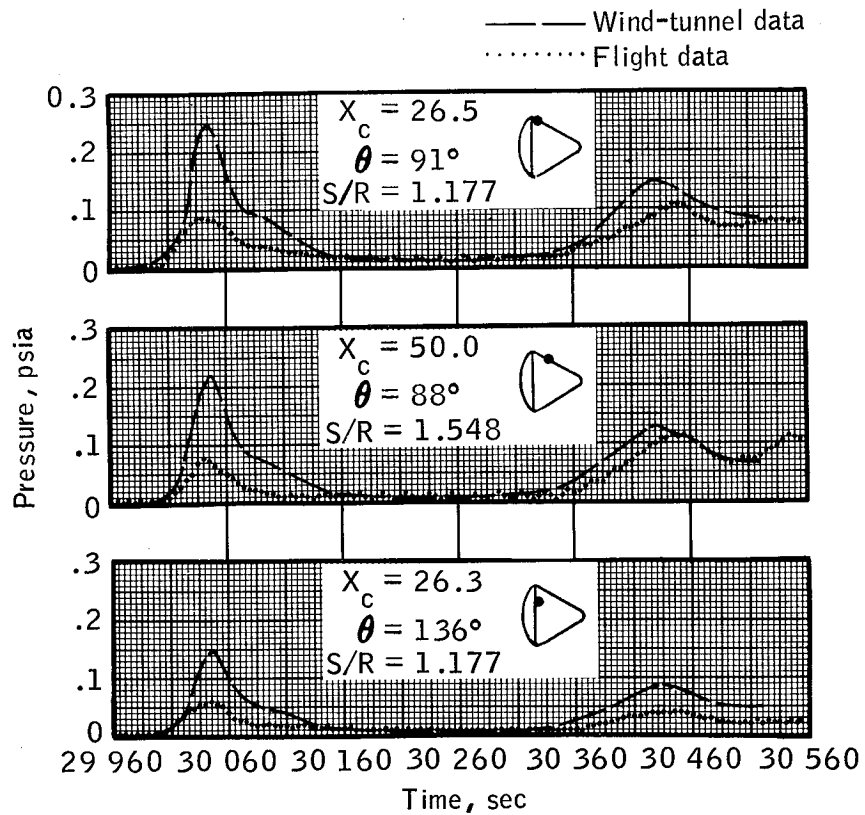


(f) $Y_c = -1.15$ in., $Z_c = 74.98$ in., $S/R = 1.038$.

Figure 7. - Continued.

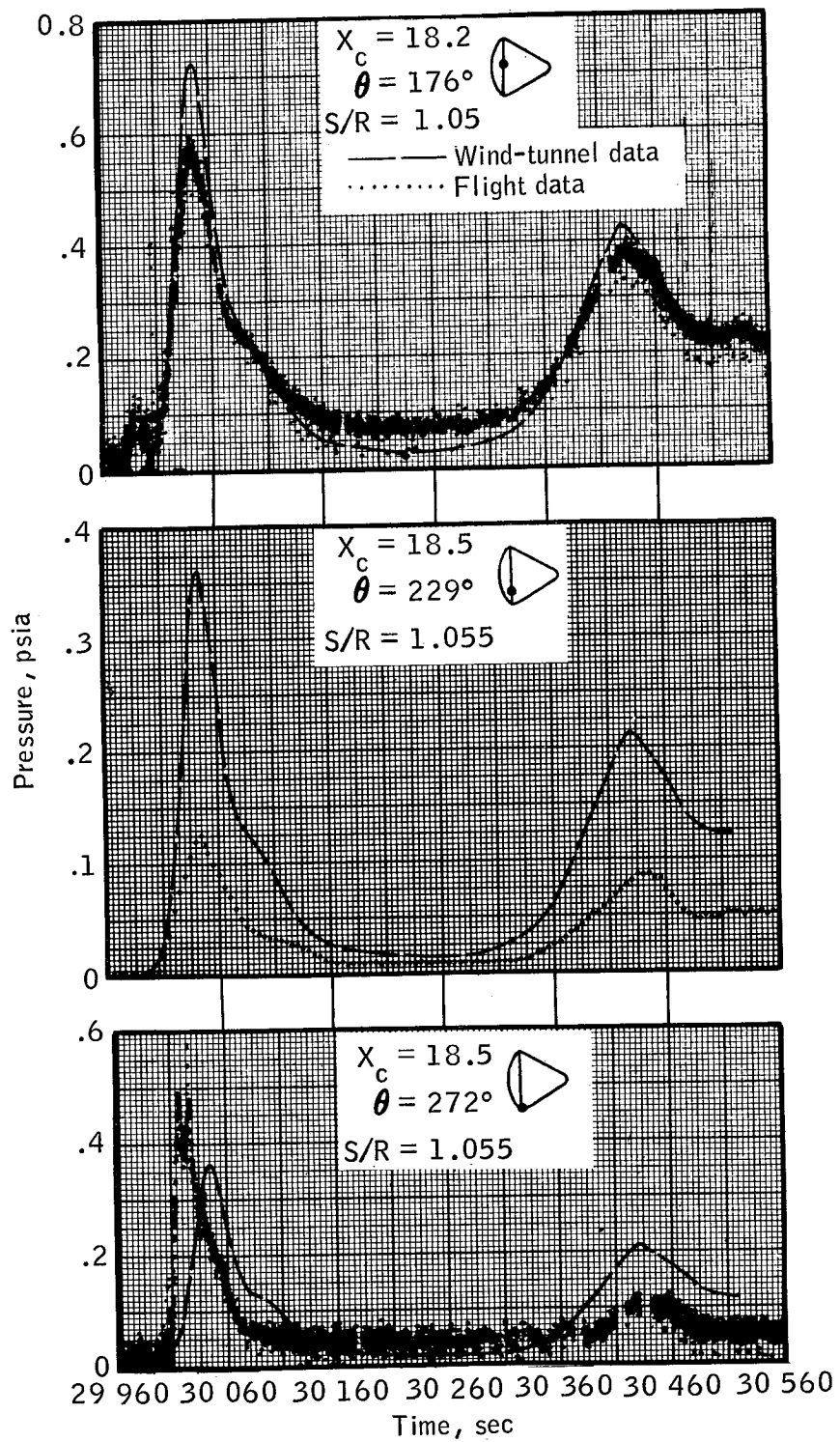


(g) $Y_c = -10.59$ in., $Z_c = -48.90$ in., $S/R = -0.663$.



(h) Conical section.

Figure 7. - Continued.



(i) Toroid.

Figure 7. - Concluded.

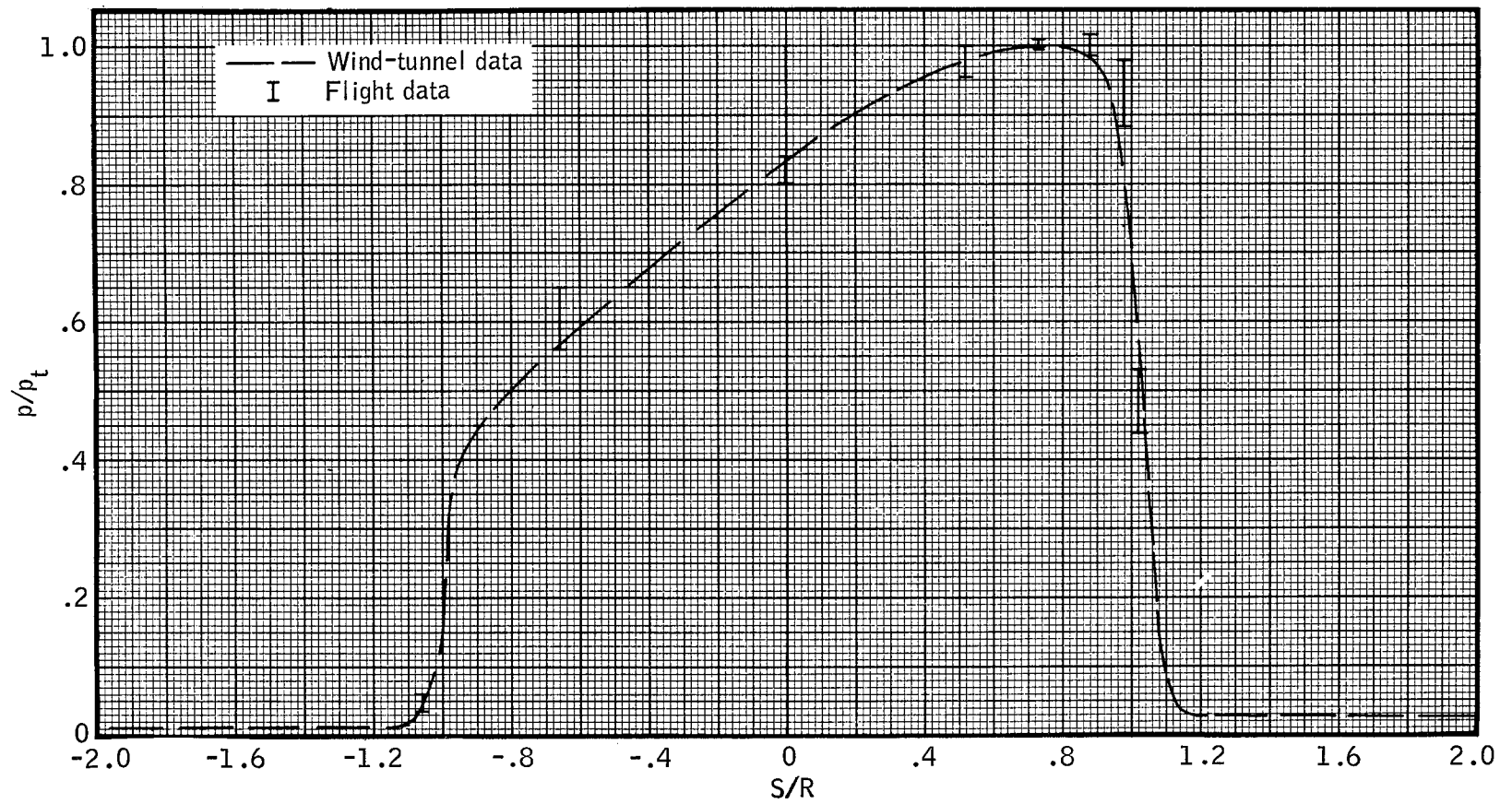
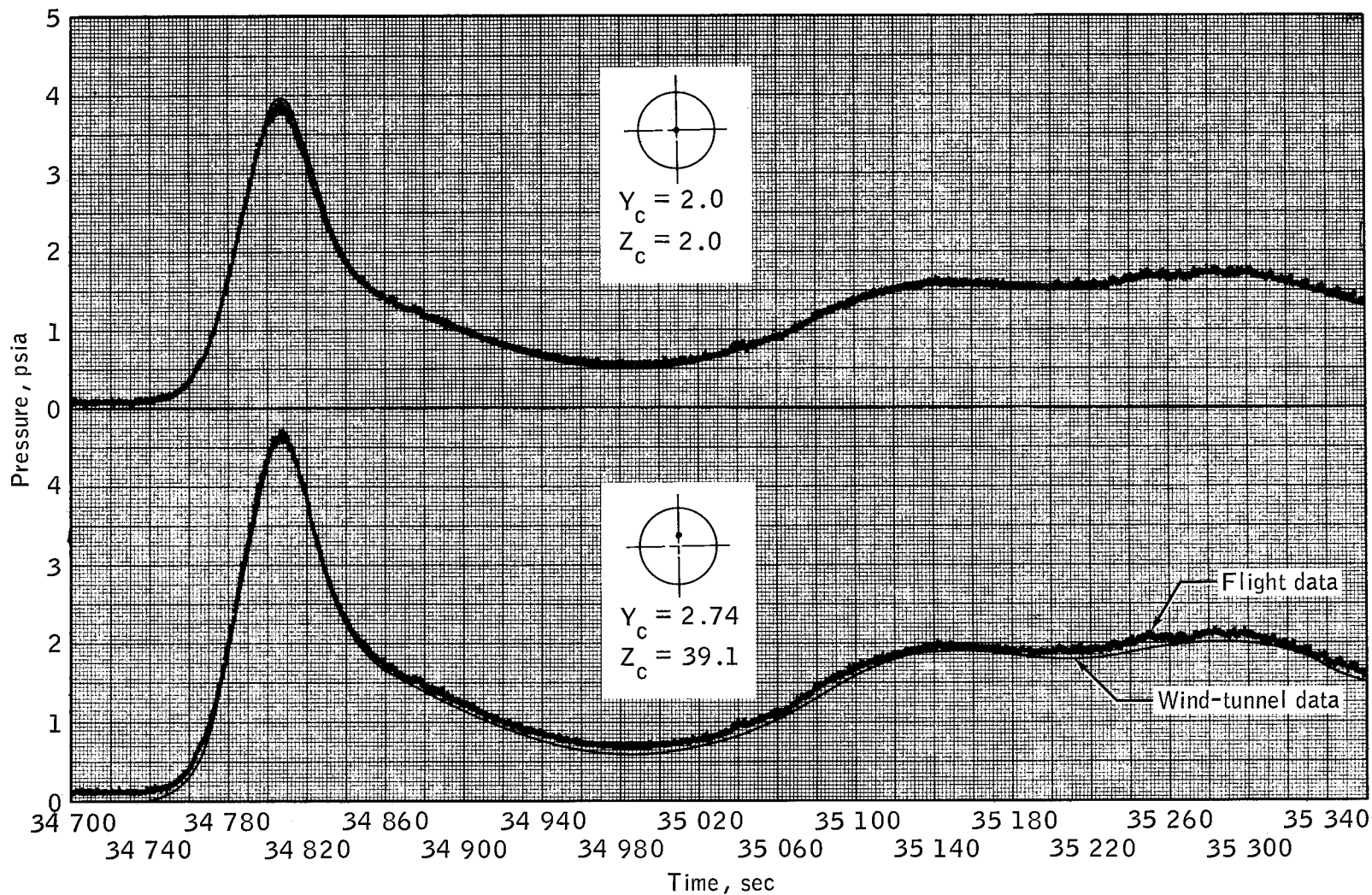
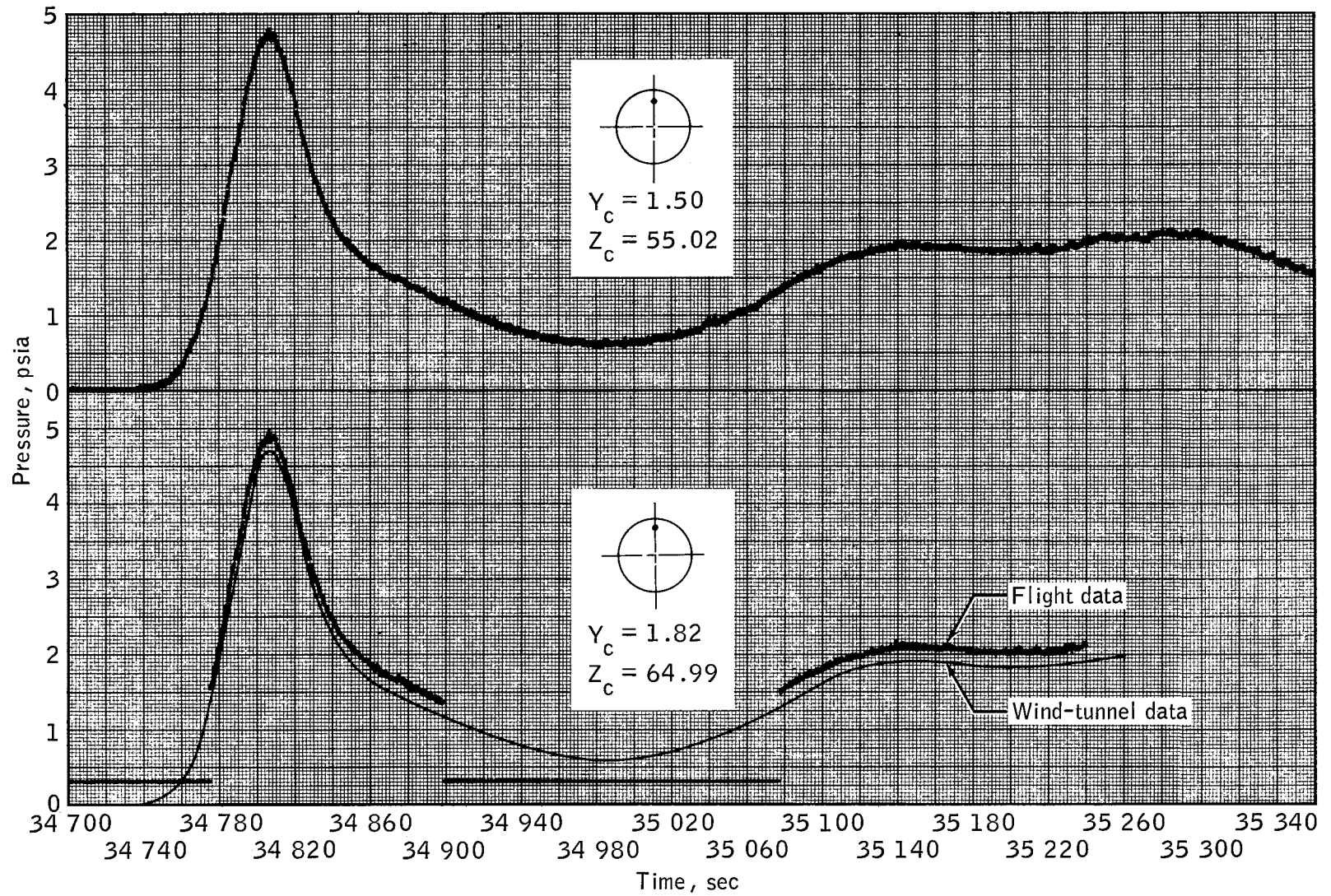


Figure 8. - Comparison of spacecraft 017 flight measurement with wind-tunnel data for $\alpha = 25^\circ$.



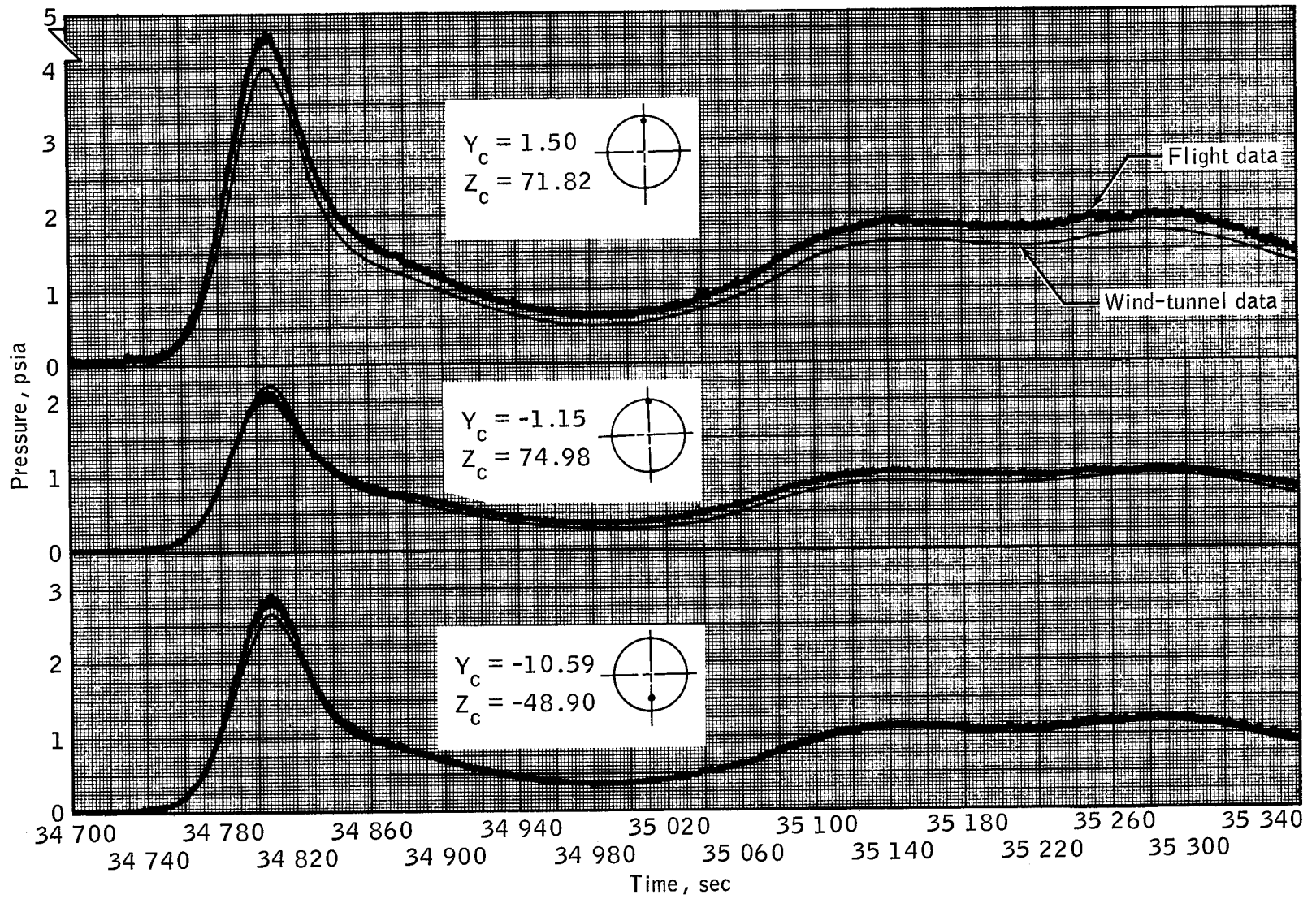
(a) Aft compartment.

Figure 9. - Histories of pressure measured on spacecraft 020.



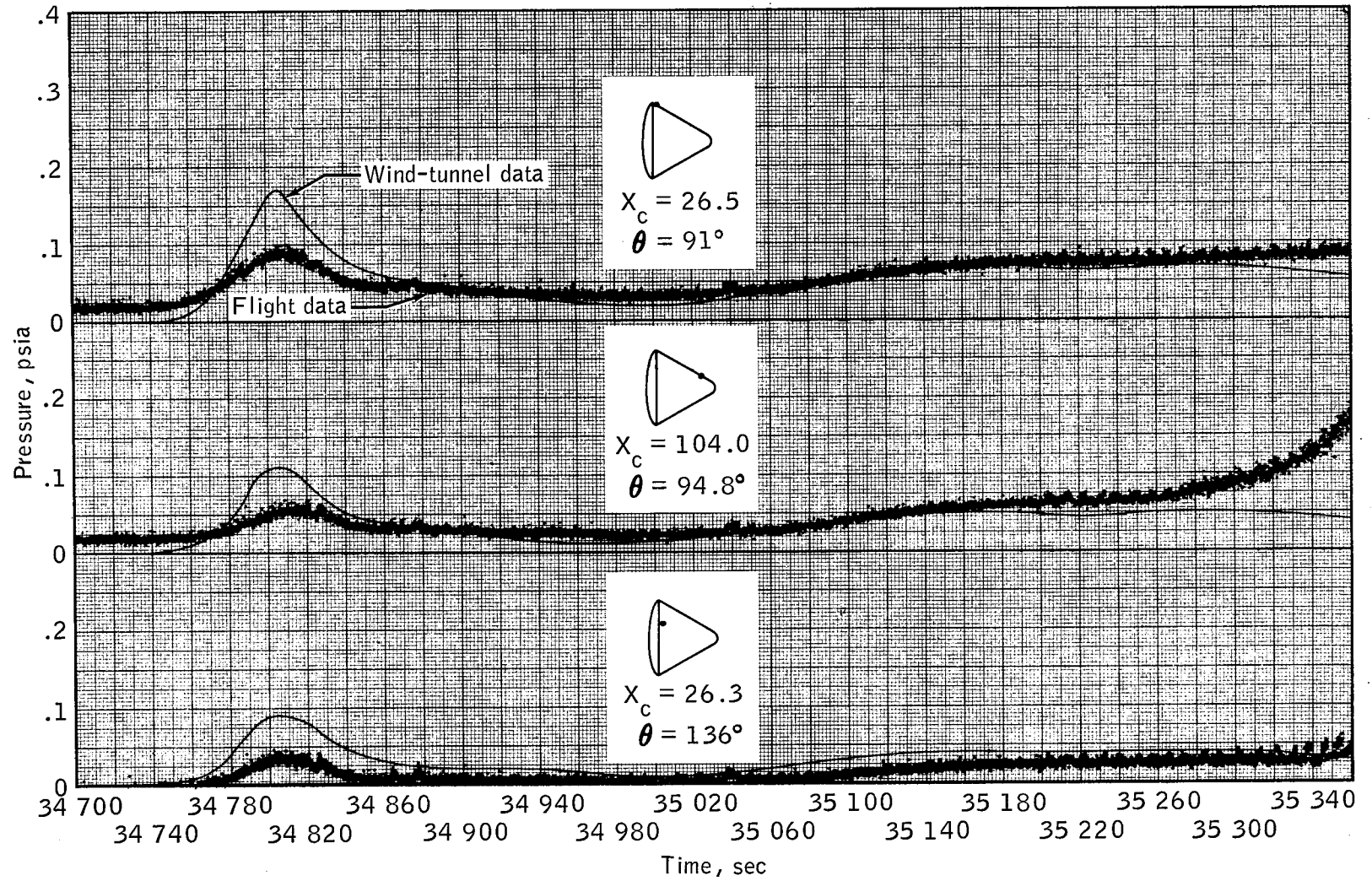
(a) Continued.

Figure 9. - Continued.



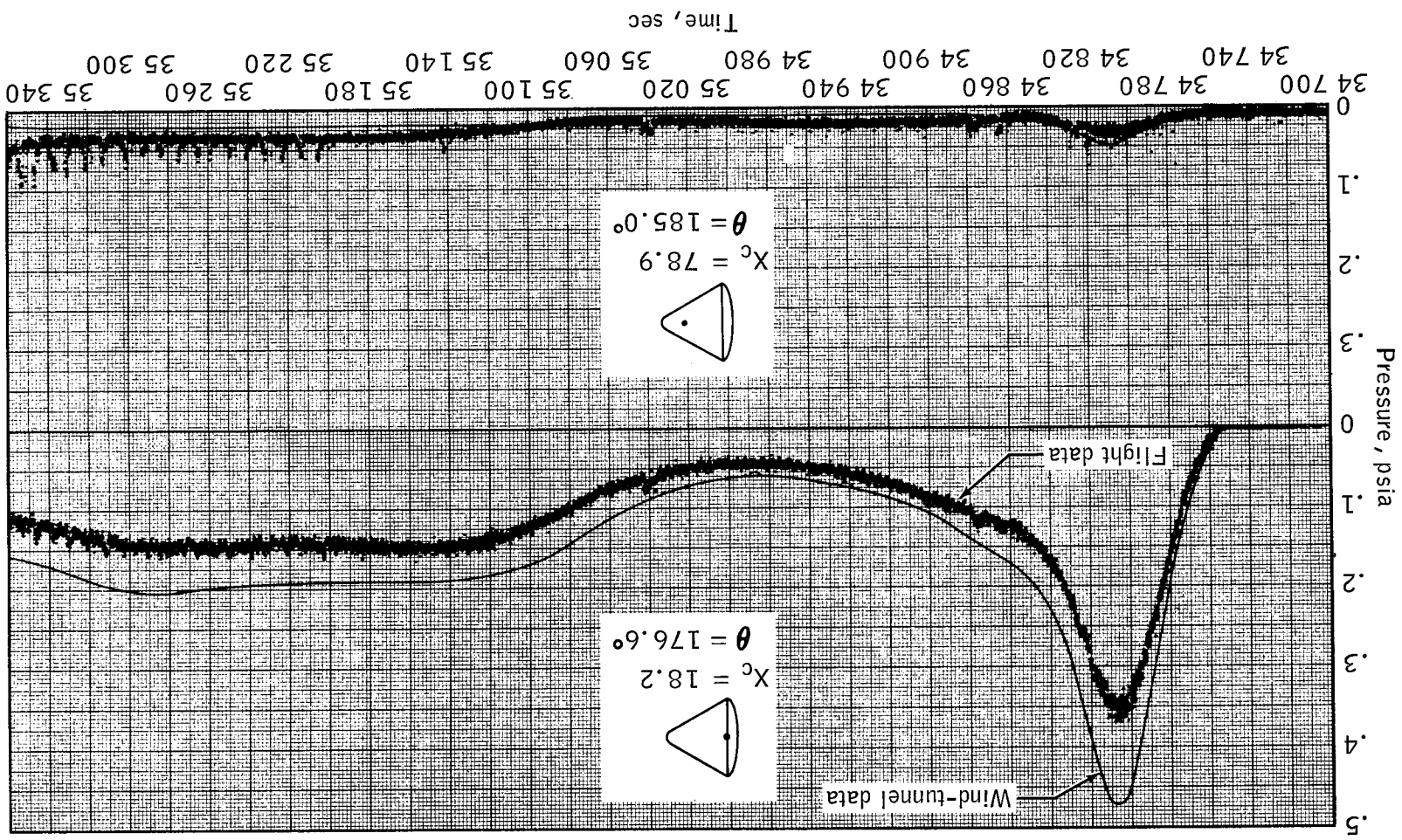
(a) Concluded.

Figure 9. - Continued.

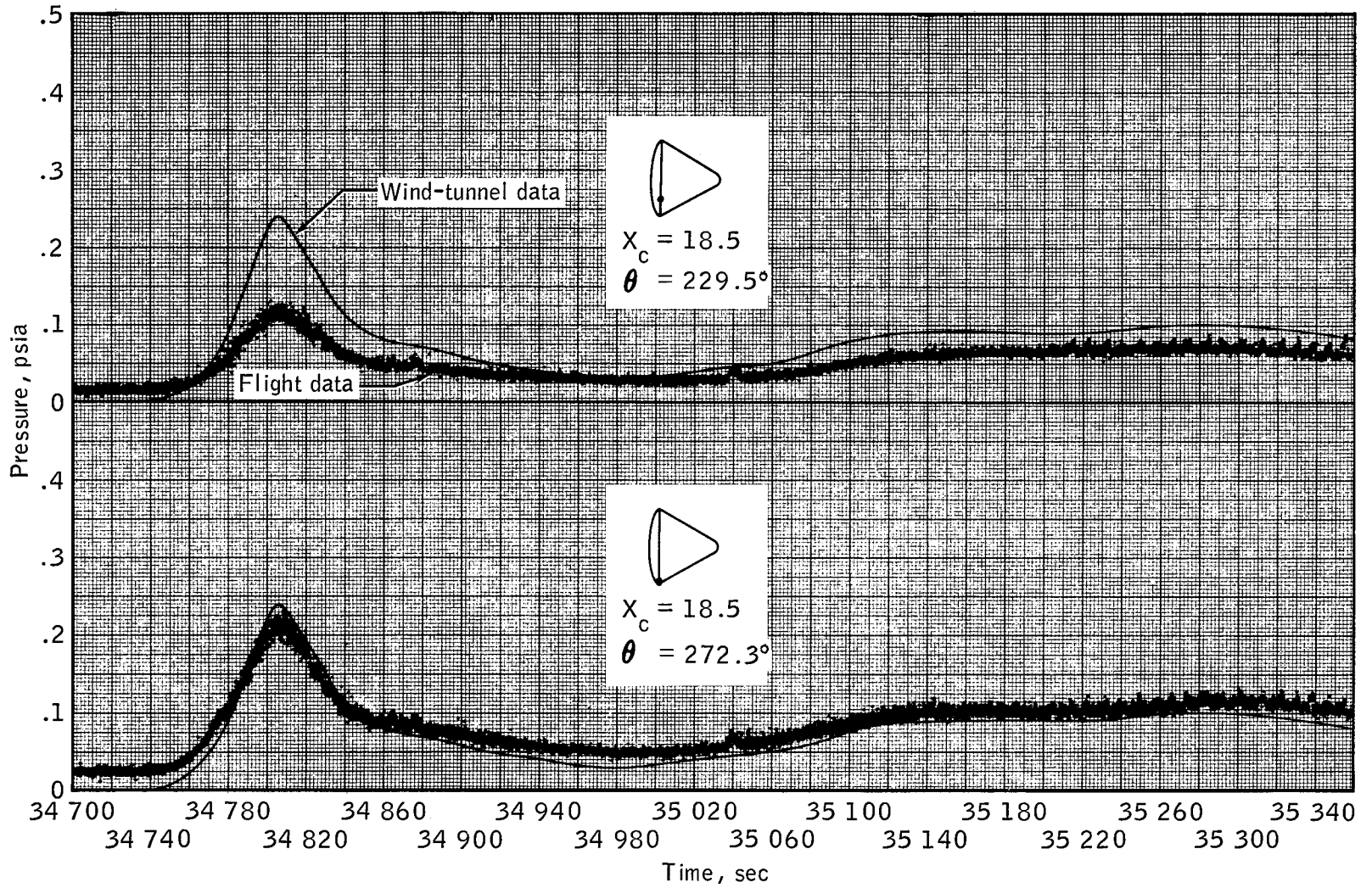


(b) Windward conical section.

Figure 9. - Continued.



(c) Yaw toroid and conical section.
 Figure 9. - Continued.



(d) Toroid.

Figure 9. - Concluded.

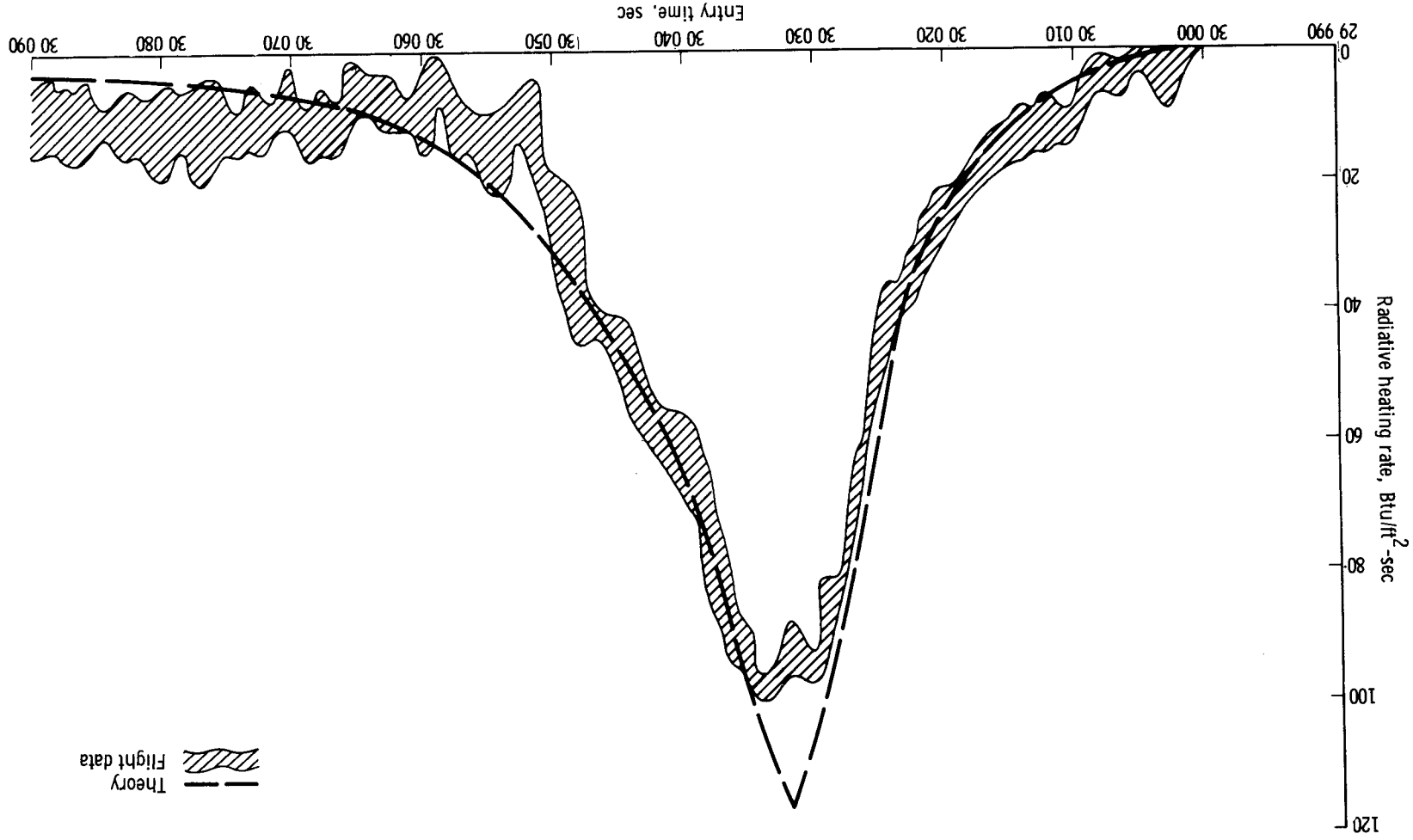
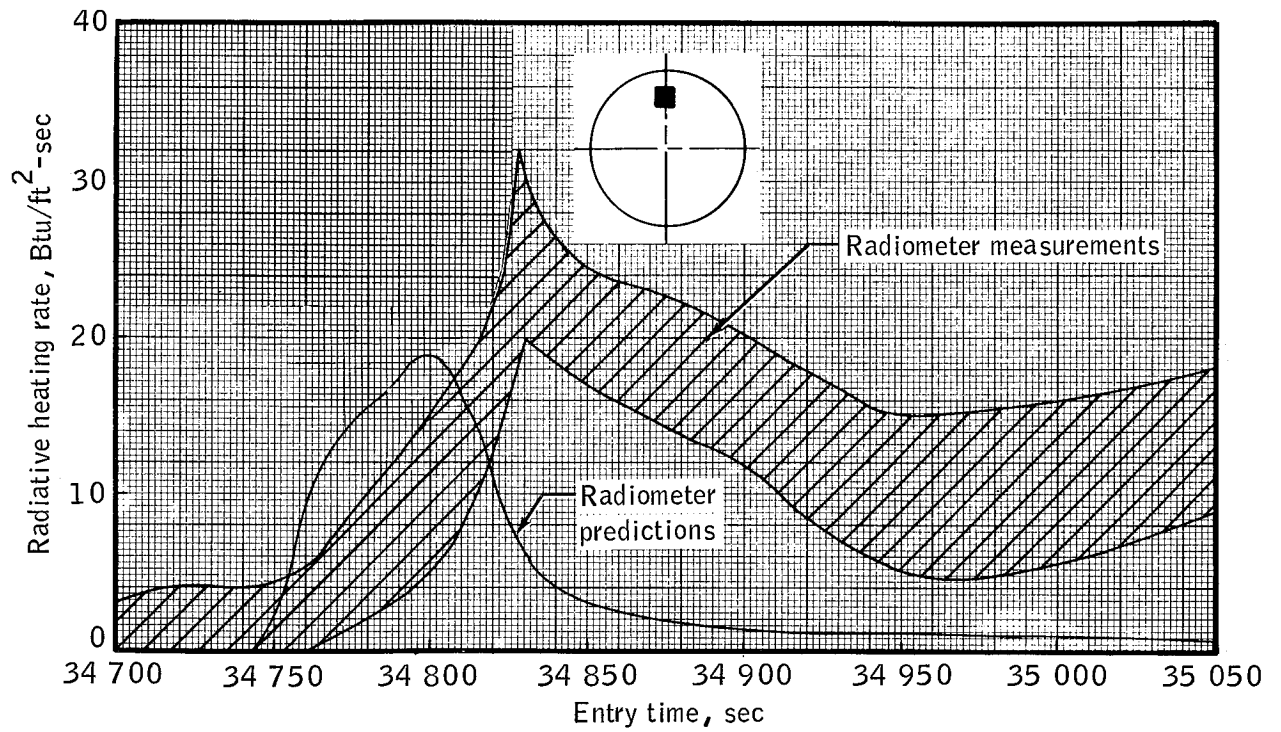
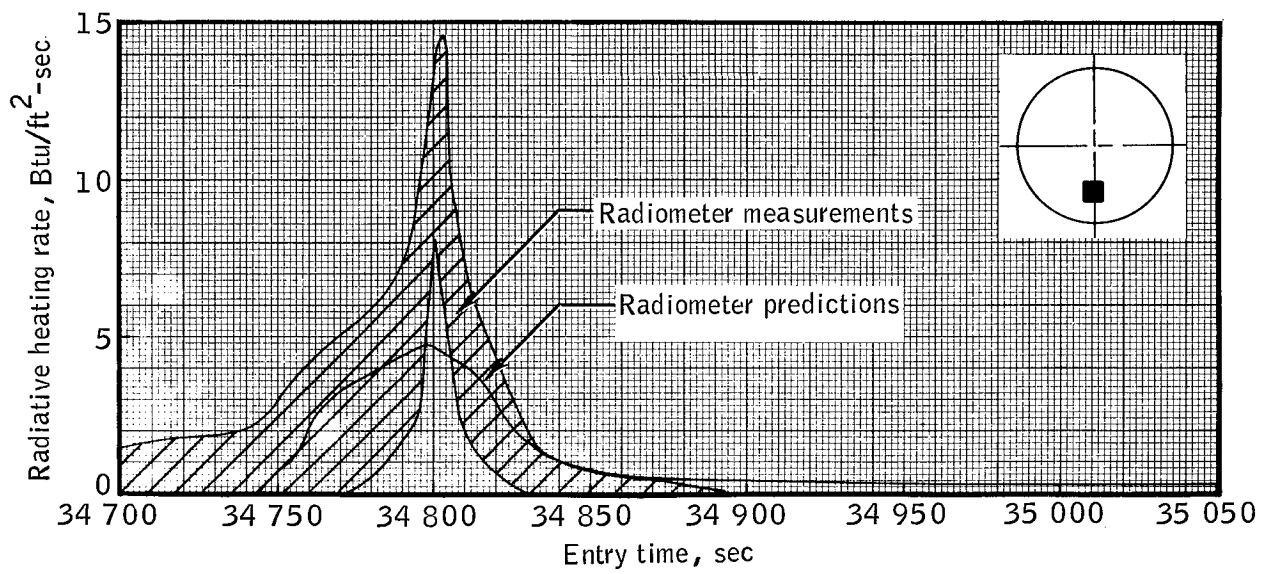


Figure 10. - Radiative heating rates measured at the stagnation point of spacecraft 017 compared with theoretical predictions.



(a) $Y_c = -0.48$ in., $Z_c = 55.0$ in., $S/R = 0.727$.



(b) $Y_c = 1.02$ in., $Z_c = -48.75$ in., $S/R = -0.643$.

Figure 11. - Comparison of measured radiative heating rates on spacecraft 020 with theoretical predictions.

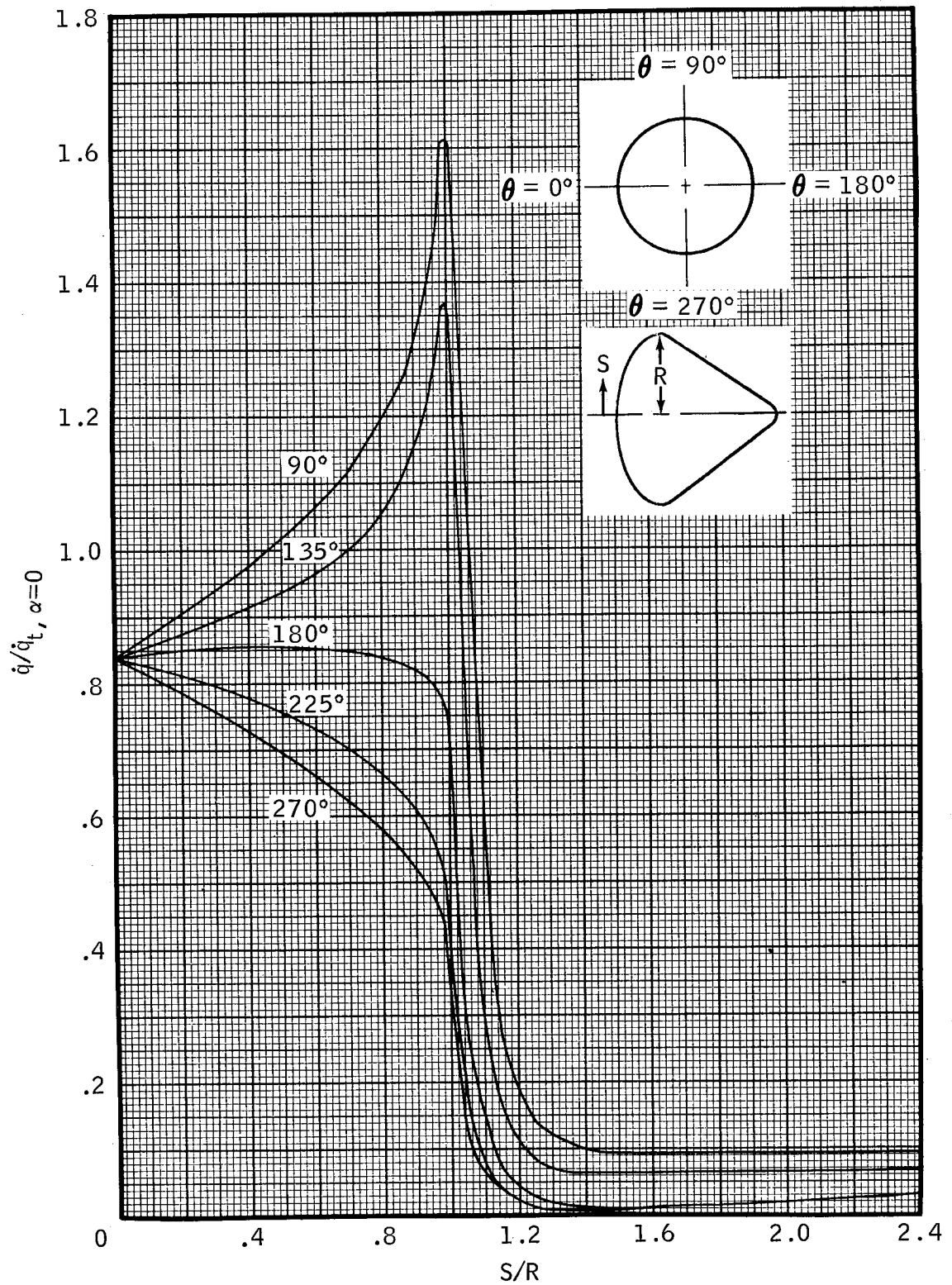
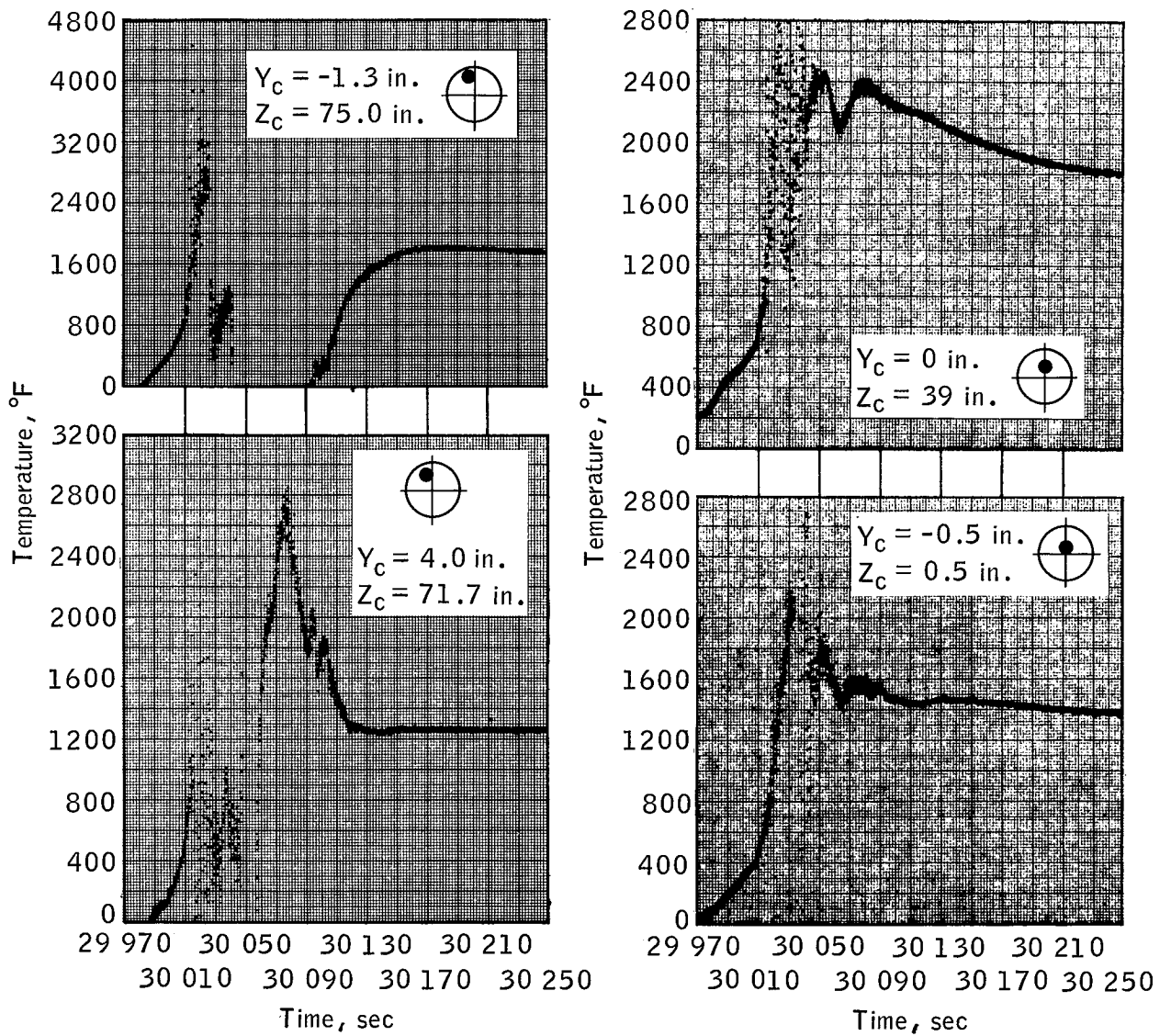
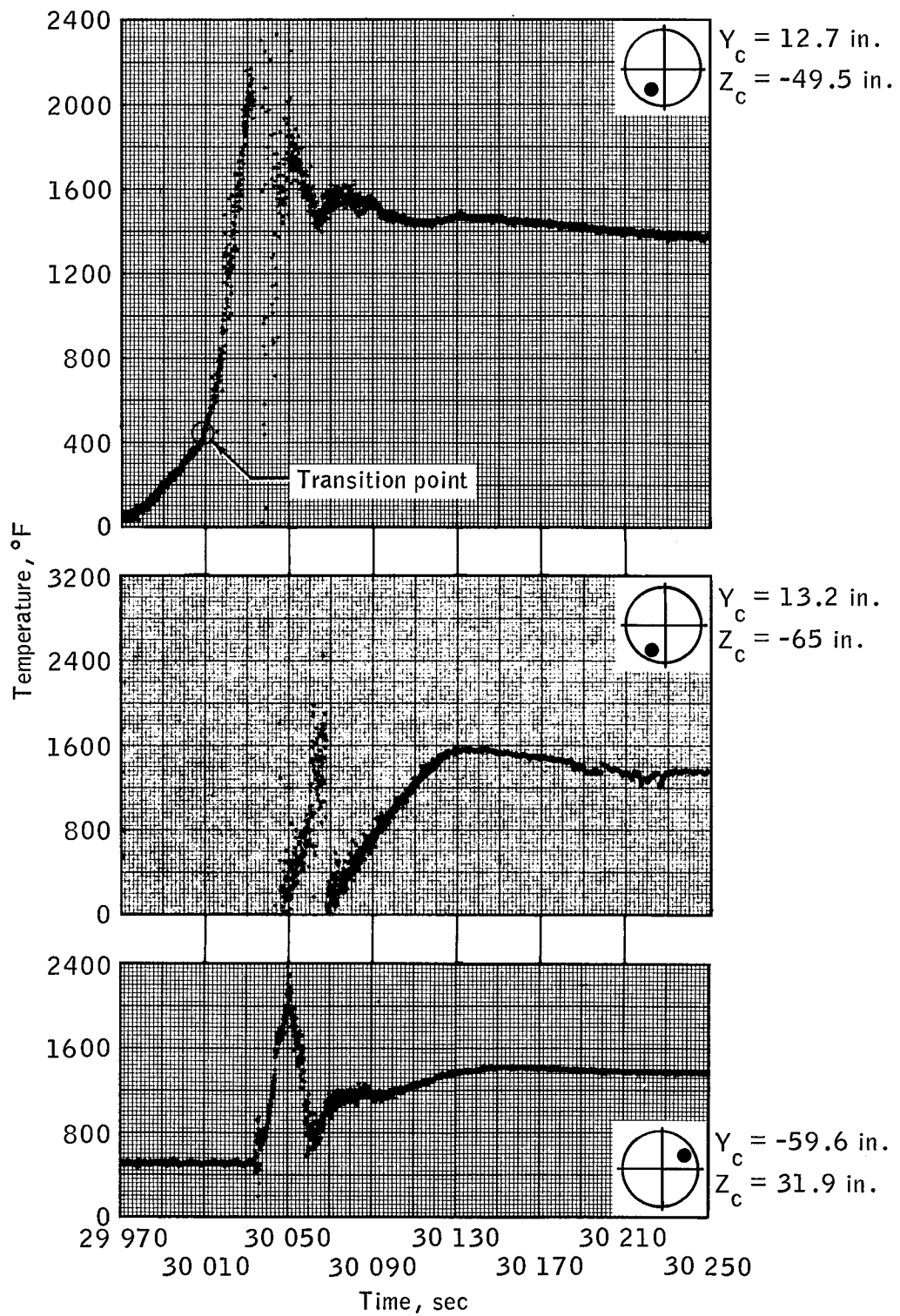


Figure 12. - Wind-tunnel distribution of local heating rate for $\alpha = 25^\circ$ divided by zero angle-of-attack stagnation-point heating rate.



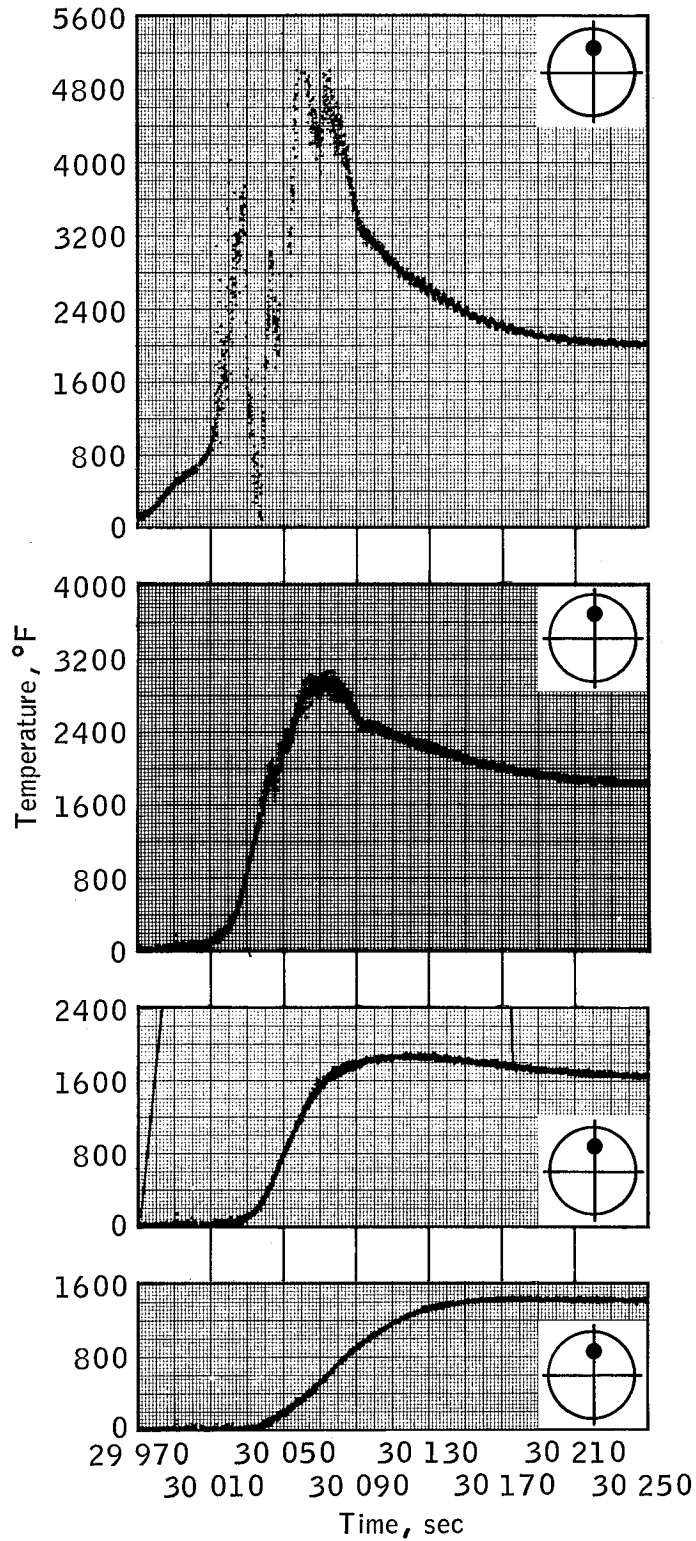
(a) Aft compartment.

Figure 13. - Histories of high-range calorimeter wafer temperatures measured on spacecraft 017.



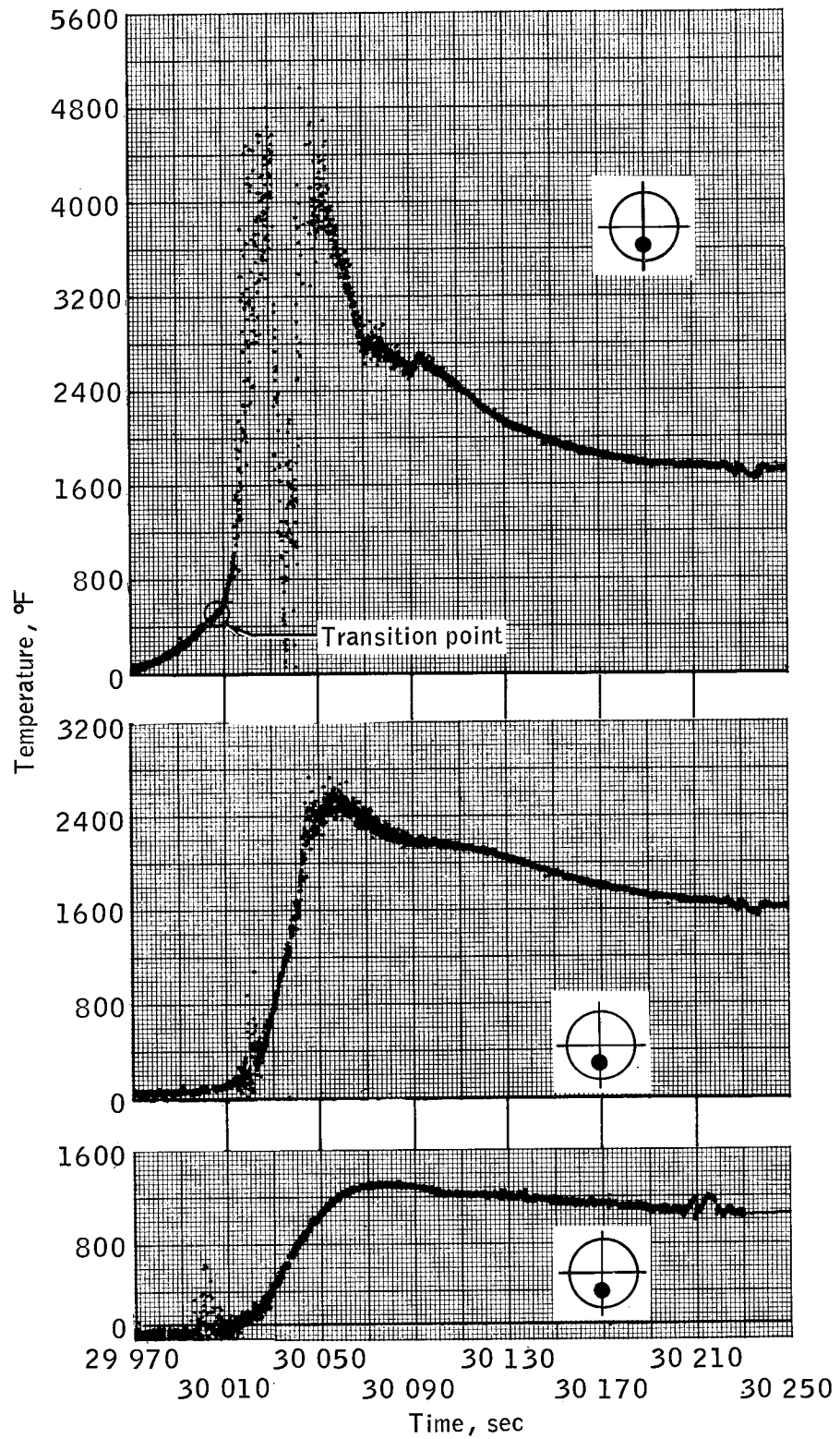
(a) Concluded.

Figure 13. - Continued.



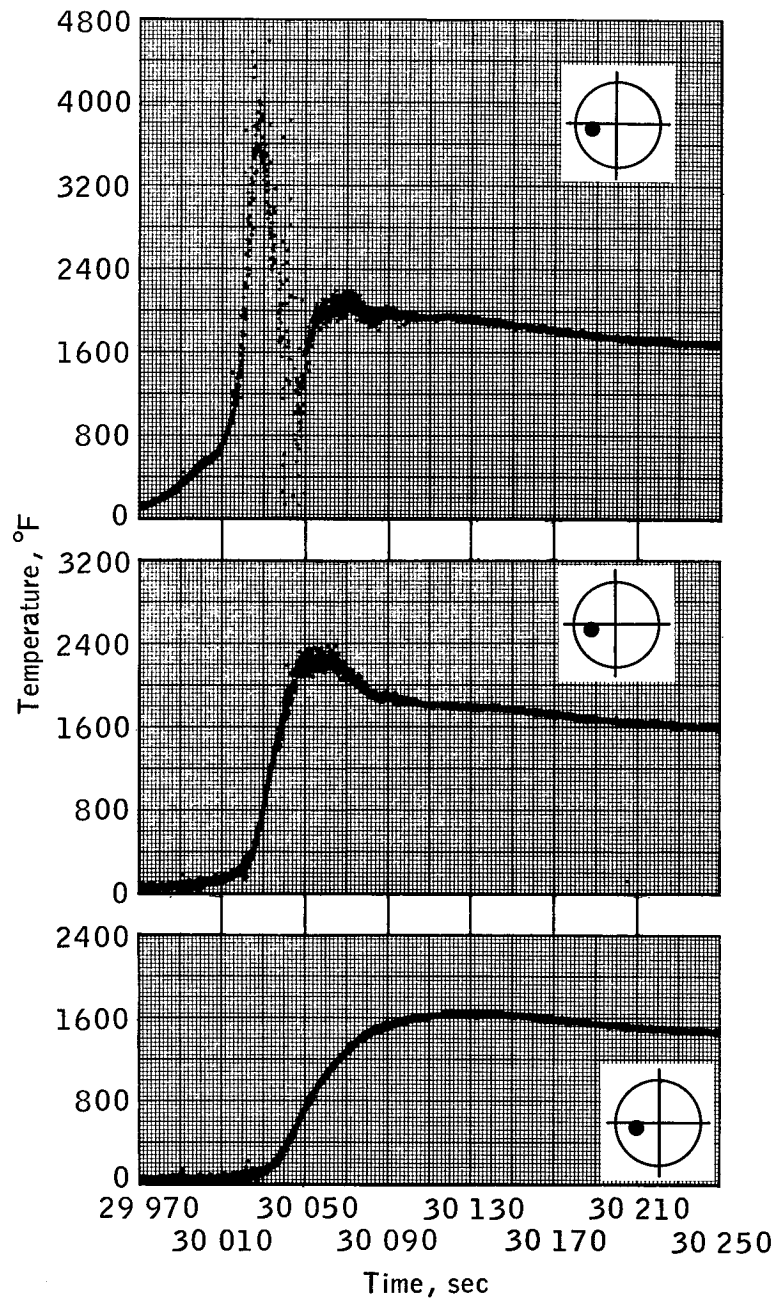
(b) Top four wafers of $Y_c = 4.23$ in., $Z_c = 55.16$ in., $S/R = 0.732$.

Figure 13. - Continued.



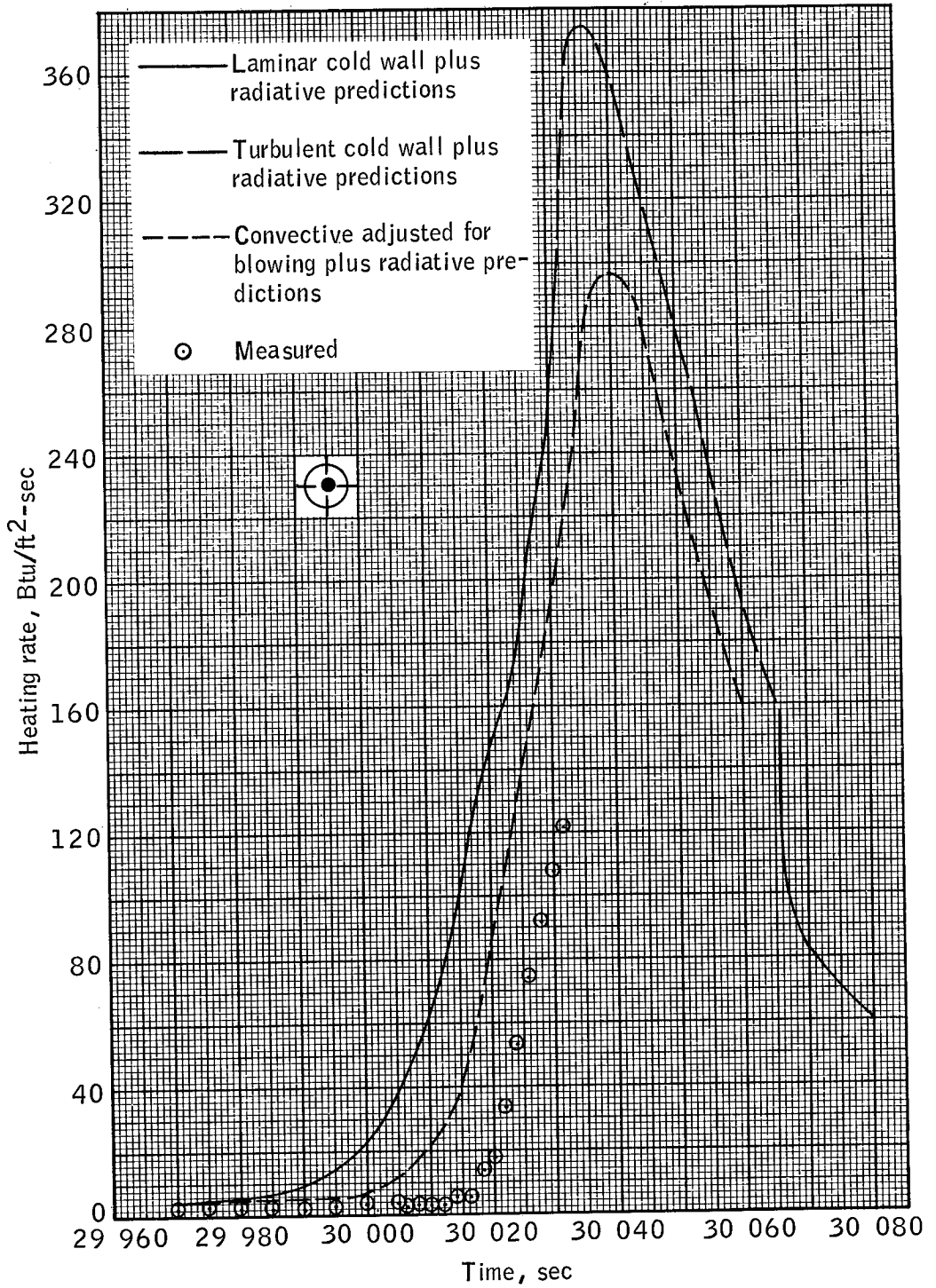
(c) Top three wafers of $Y_c = -4.74$ in., $Z_c = -50.0$ in., $S/R = -0.663$.

Figure 13. - Continued.



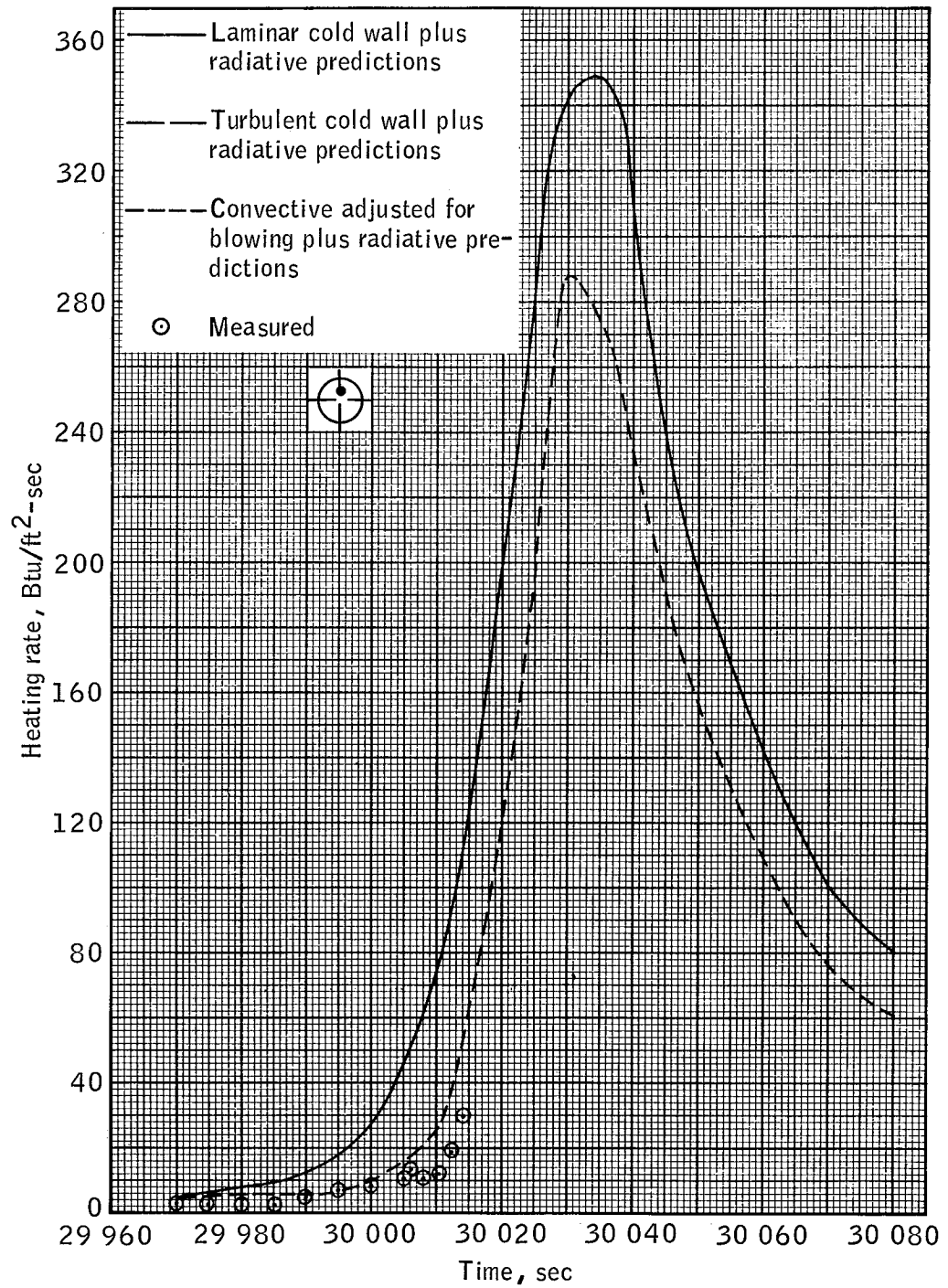
(d) Top three wafers of $Y_c = 50.0$ in., $Z_c = -1.5$ in., $S/R = 0.666$.

Figure 13. - Concluded.



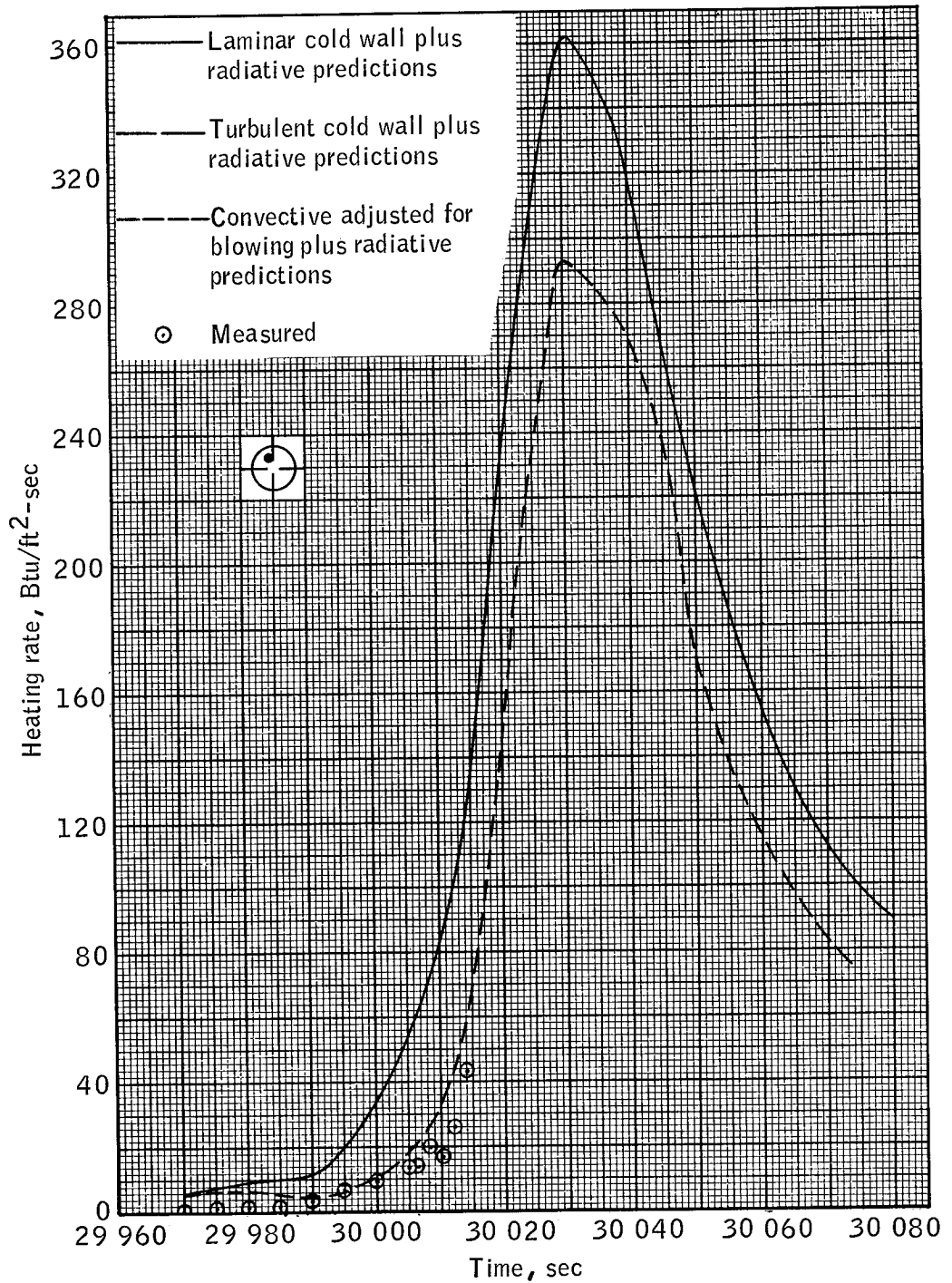
(a) $Y_c = -0.48$ in., $Z_c = 0.48$ in., $S/R = 0.004$.

Figure 14. - Heating rates calculated from wafer calorimeter temperature measurements on spacecraft 017.



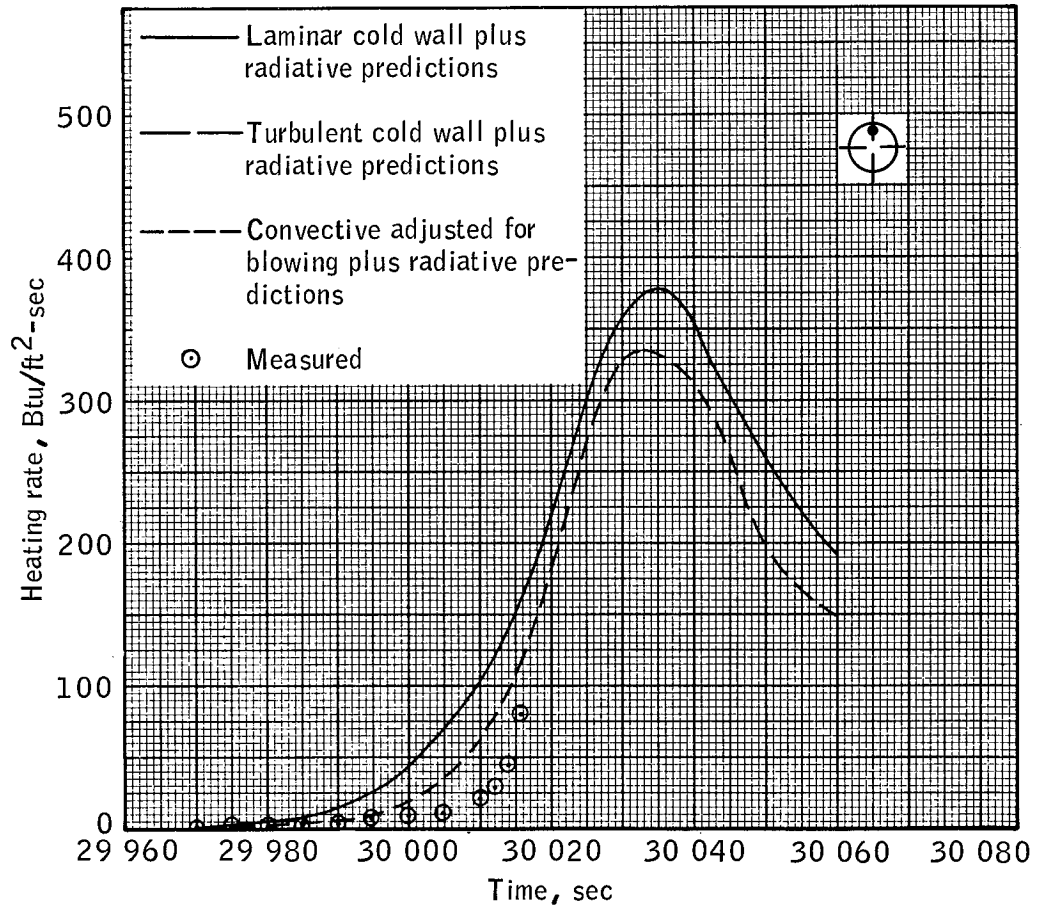
(b) $Y_c = 0$ in., $Z_c = 39.0$ in., $S/R = 0.512$.

Figure 14. - Continued.



(c) $Y_c = 4.23$ in., $Z_c = 55.16$ in., $S/R = 0.732$.

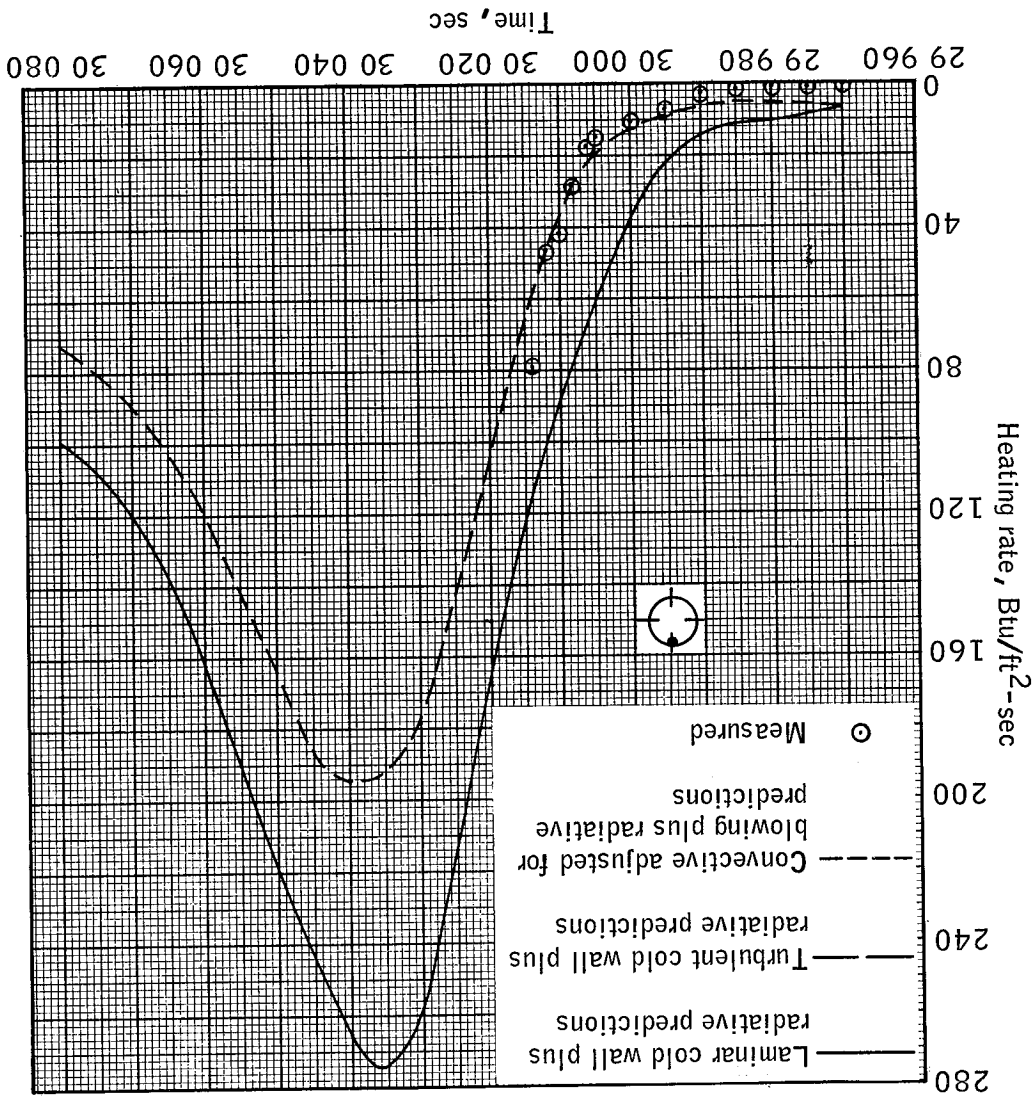
Figure 14. - Continued.

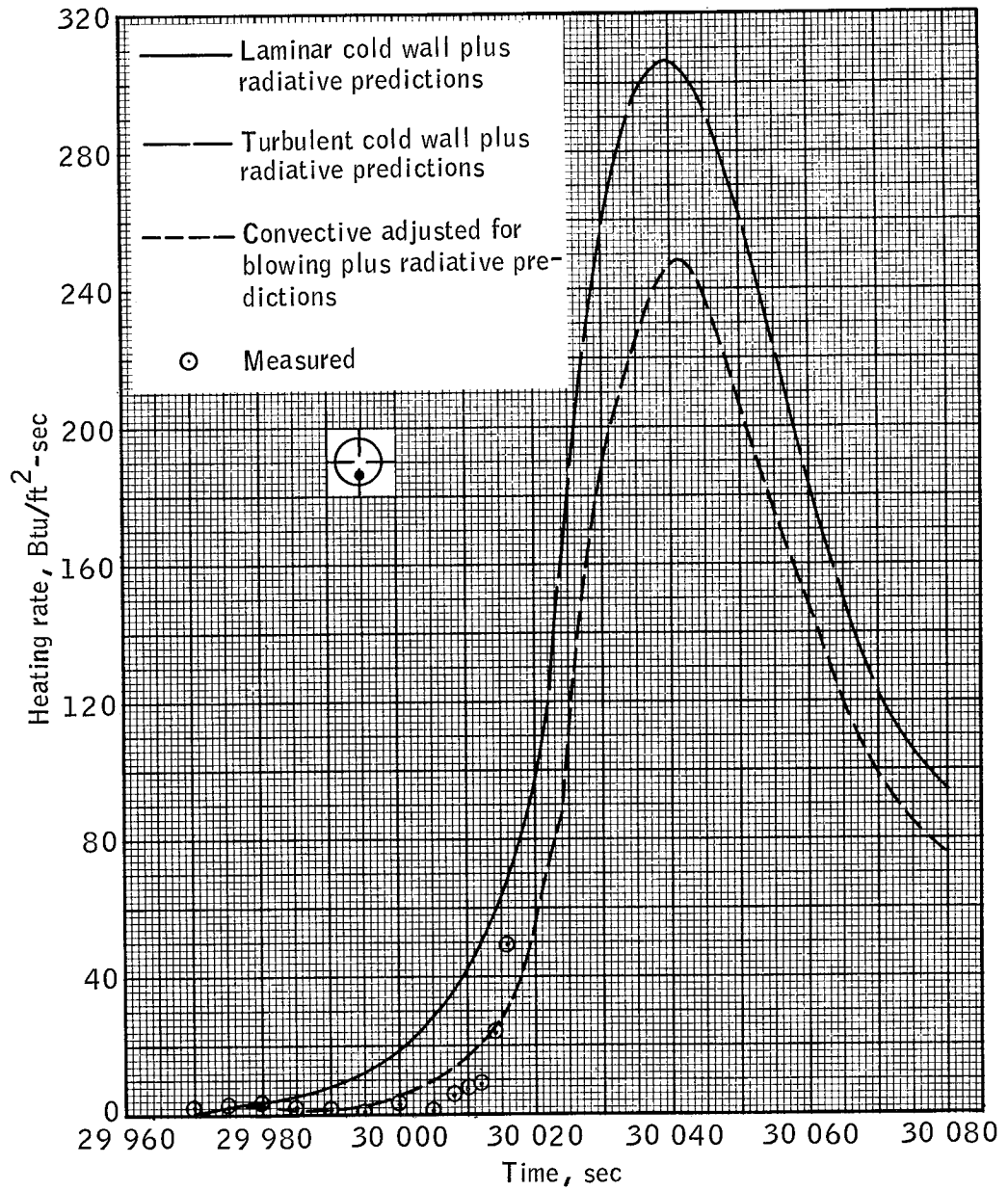


(d) $Y_c = 4.01$ in., $Z_c = 71.72$ in., $S/R = 0.969$.

Figure 14. - Continued.

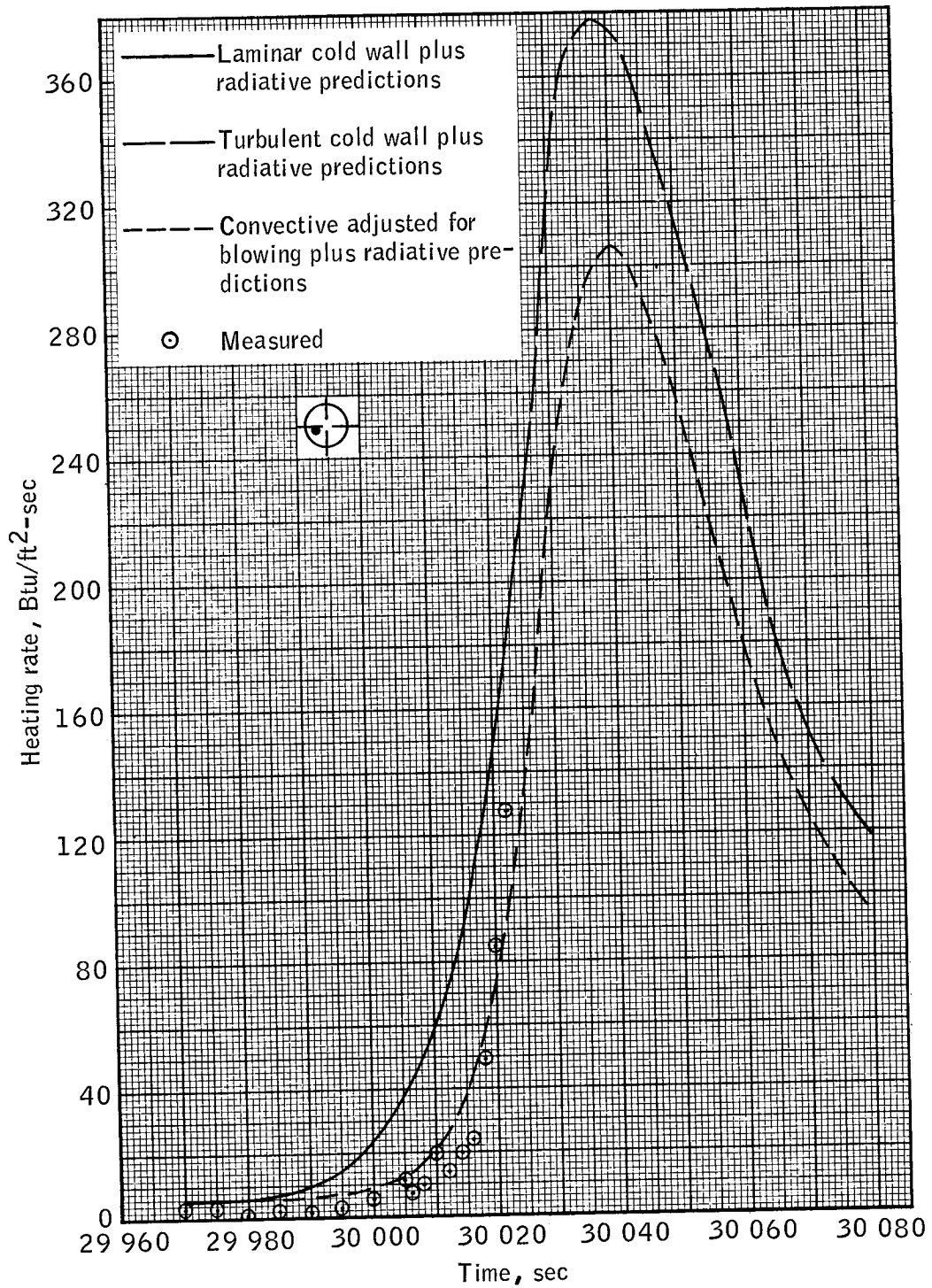
(e) $Y_c = 1.31$ in., $Z_c = 74.98$ in., $S/R = 1.038$.
Figure 14. - Continued.





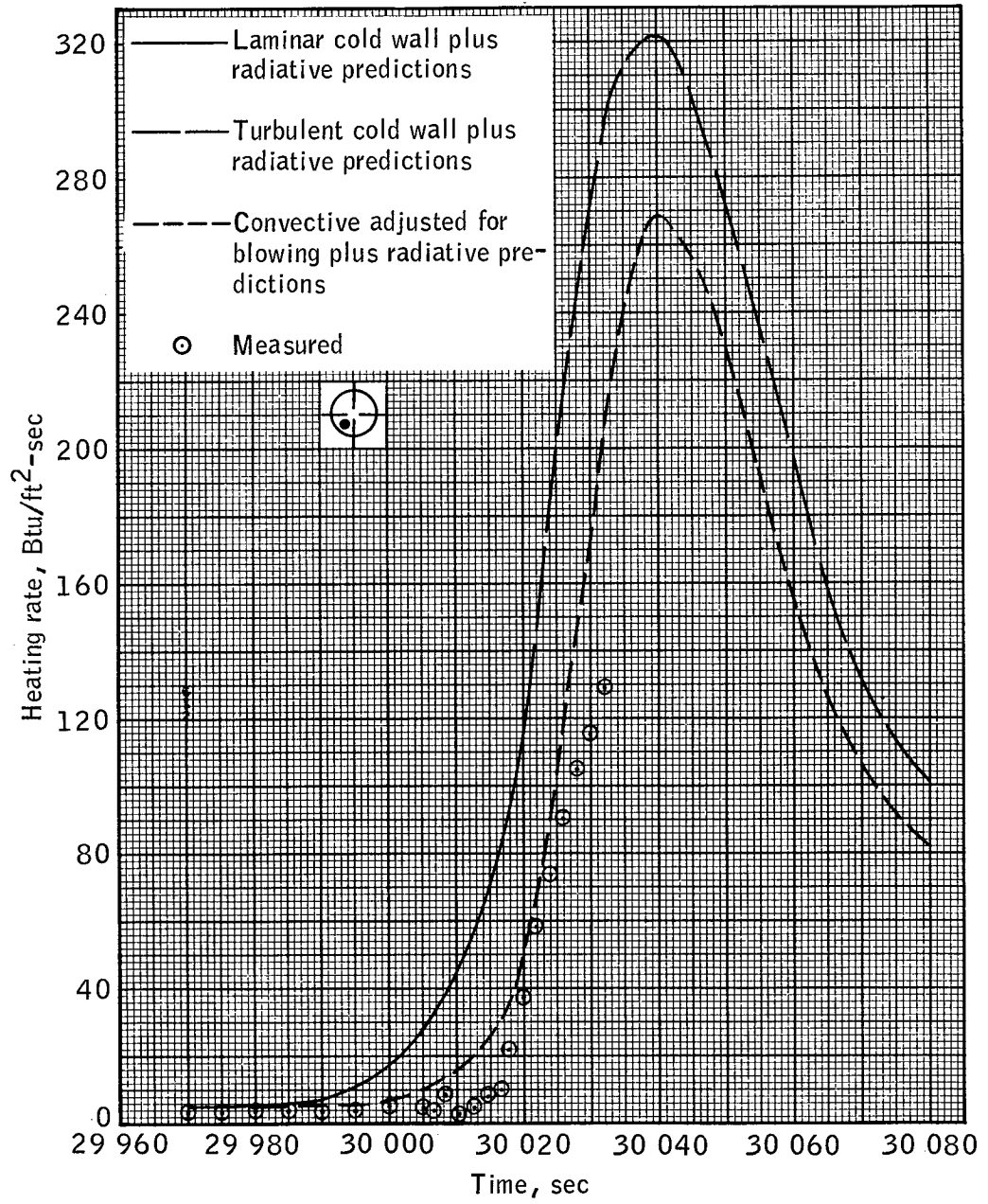
(f) $Y_c = -4.74$ in., $Z_c = -50.0$ in., $S/R = -0.663$.

Figure 14. - Continued.



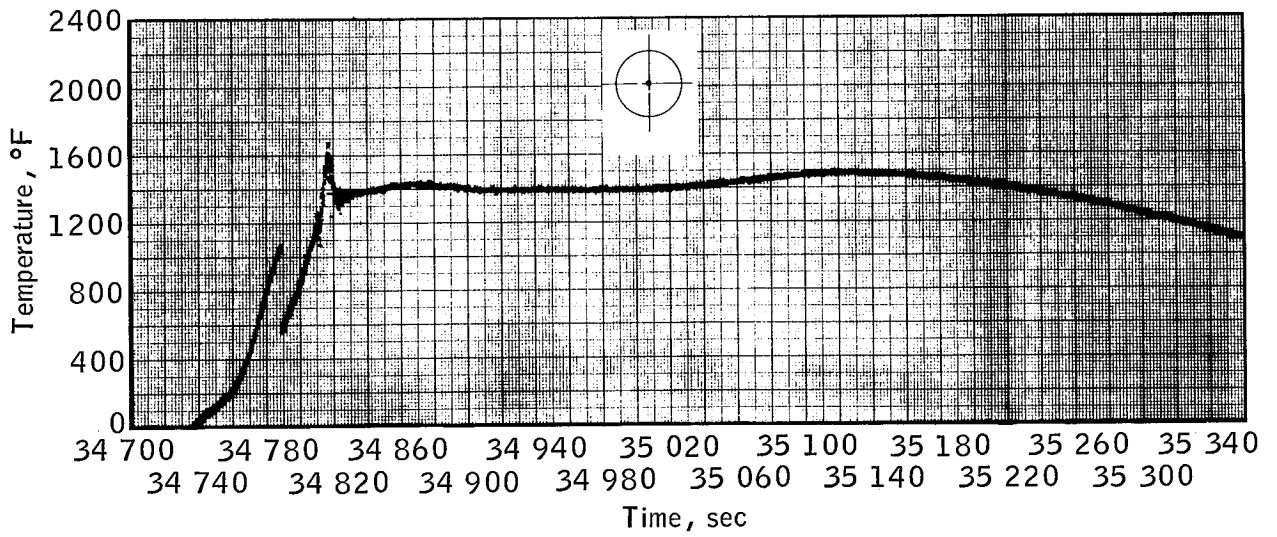
(g) $Y_c = 50.0$ in., $Z_c = -1.5$ in., $S/R = 0.666$, $\theta = 0^\circ$.

Figure 14. - Continued.

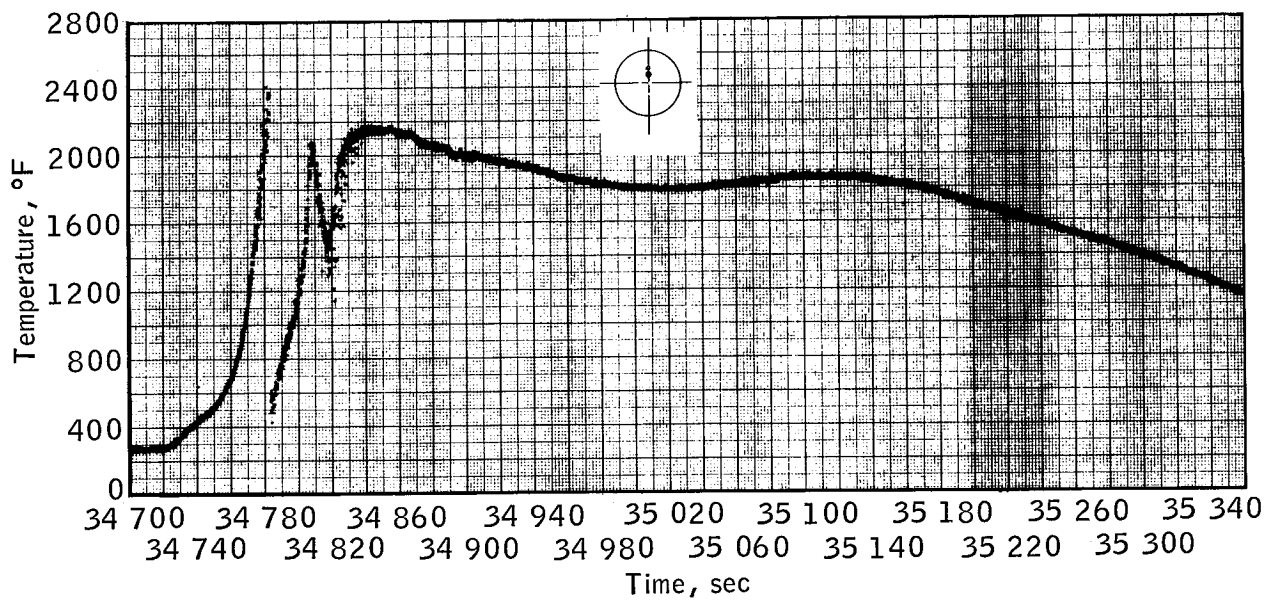


(h) $Y_c = 12.73$ in., $Z_c = -49.47$ in., $S/R = 0.671$, $\theta = 284^\circ$.

Figure 14. - Concluded.

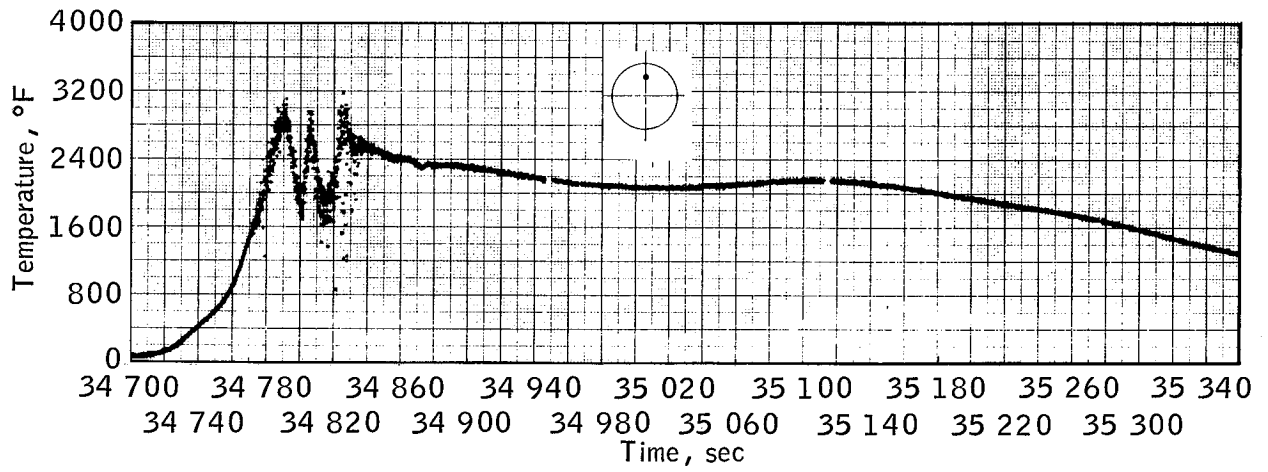


(a) $Y_c = -0.48$ in., $Z_c = 0.48$ in., $S/R = 0.004$.

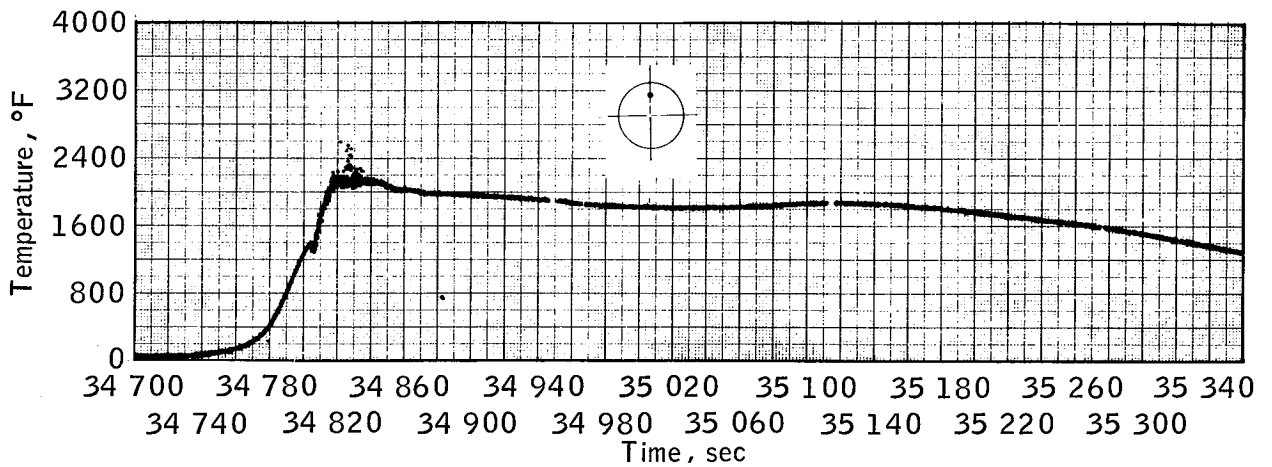


(b) $Y_c = 0$ in., $Z_c = 39.0$ in., $S/R = 0.512$.

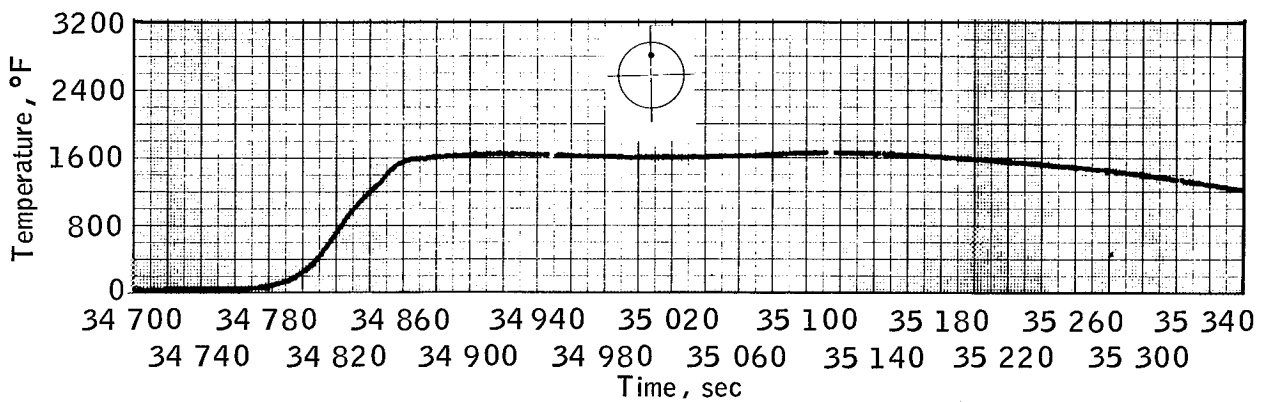
Figure 15. - High-range calorimeter wafer temperature measured on spacecraft 020.



(c) Top wafer of $Y_c = 4.23$ in., $Z_c = 55.16$ in., $S/R = 0.732$.

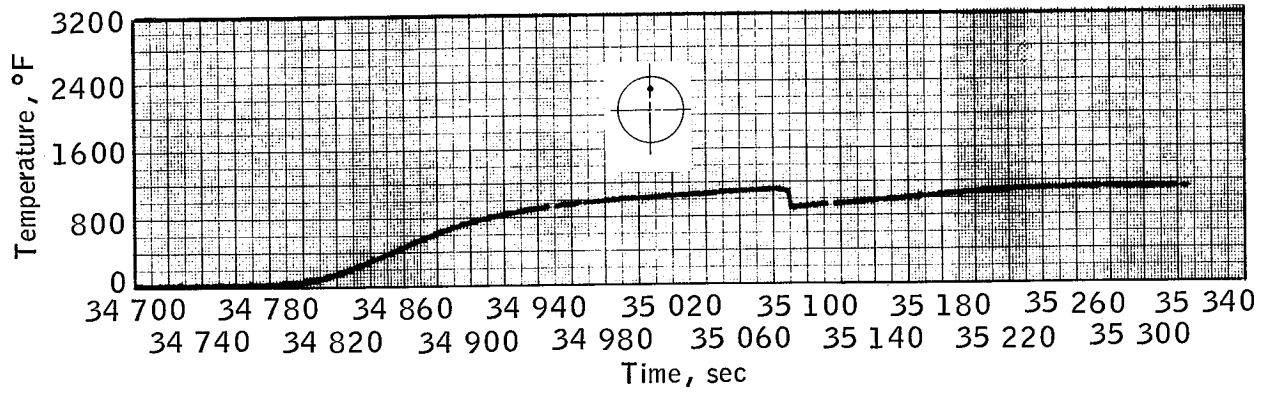


(d) Second wafer of $Y_c = 4.23$ in., $Z_c = 55.16$ in., $S/R = 0.732$.

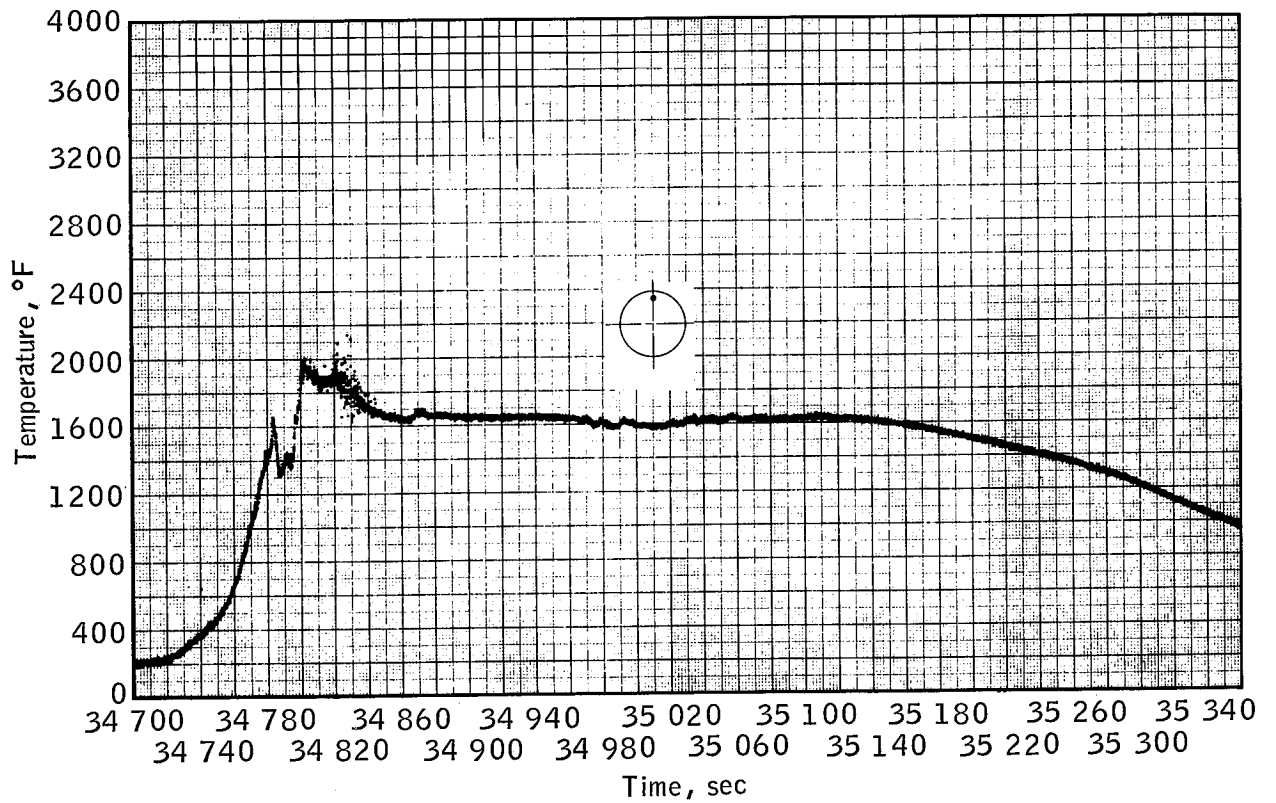


(e) Third wafer of $Y_c = 4.23$ in., $Z_c = 55.16$ in., $S/R = 0.732$.

Figure 15. - Continued.

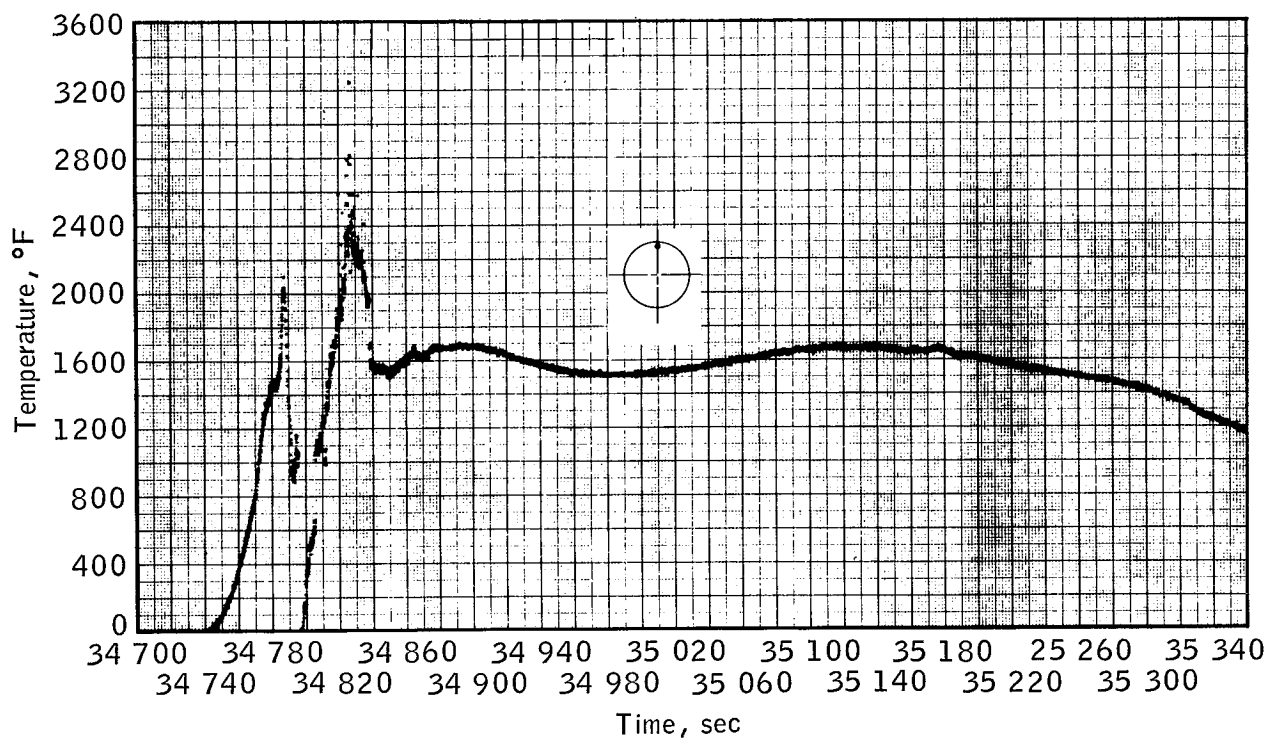


(f) Fourth wafer of $Y_c = 4.23$ in., $Z_c = 55.16$ in., $S/R = 0.732$.

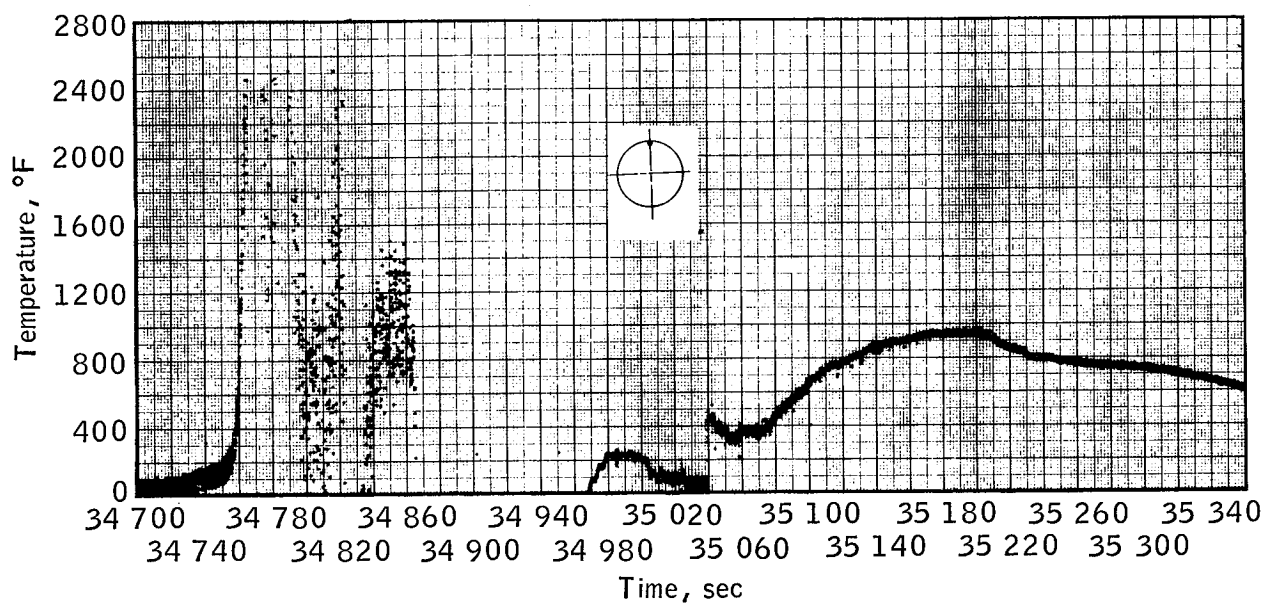


(g) $Y_c = 0$ in., $Z_c = 65.0$ in., $S/R = 0.865$.

Figure 15. - Continued.

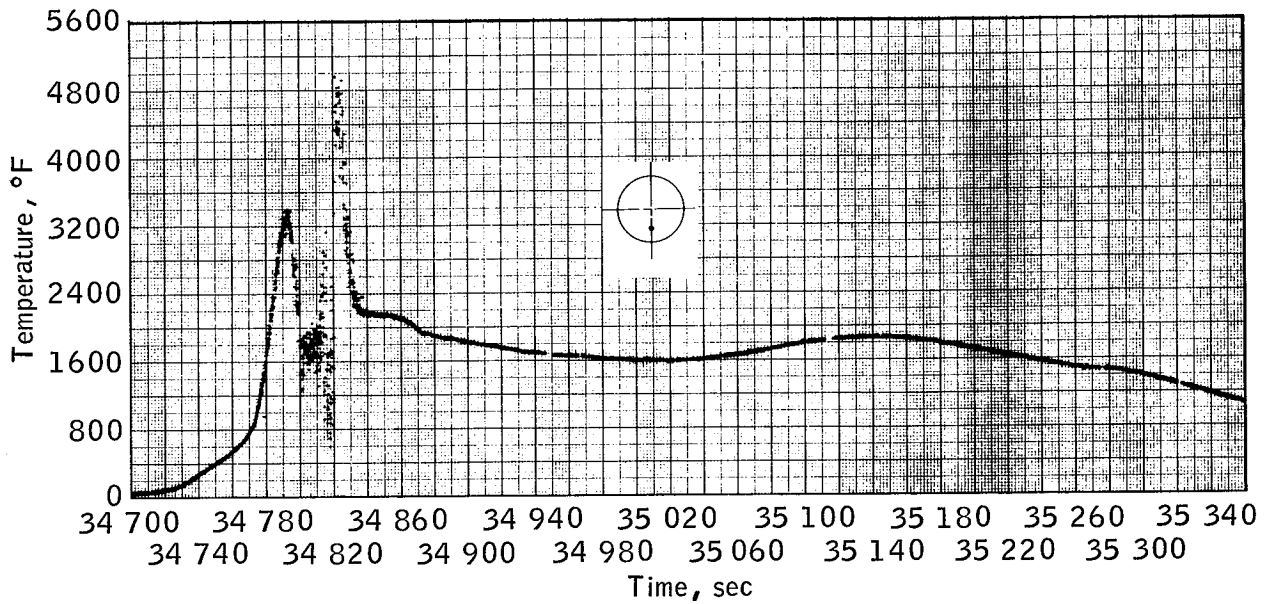


(h) $Y_c = 4.01$ in., $Z_c = 71.72$ in., $S/R = 0.969$.

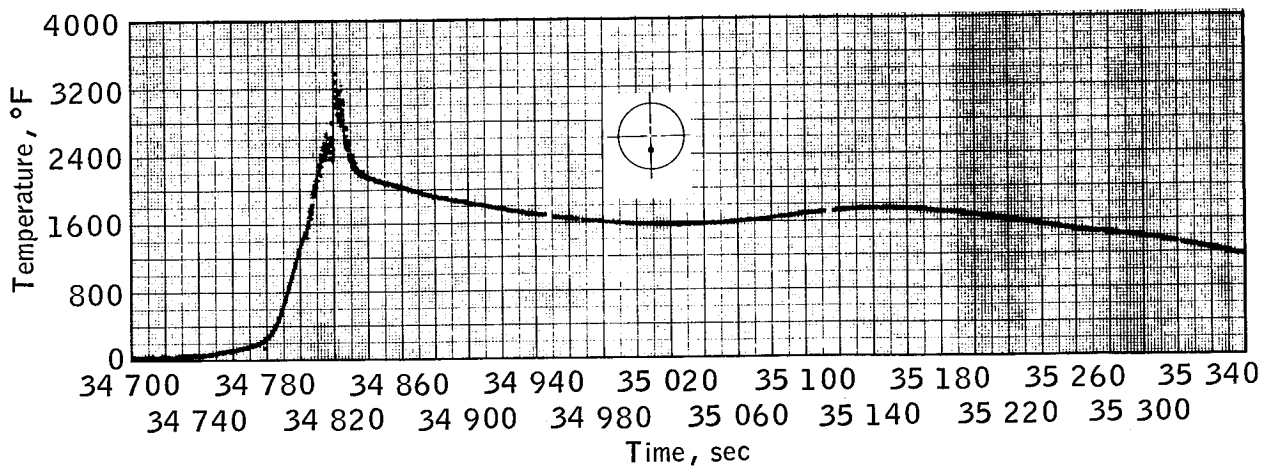


(i) $Y_c = 1.31$ in., $Z_c = 74.98$ in., $S/R = 1.038$.

Figure 15. - Continued.

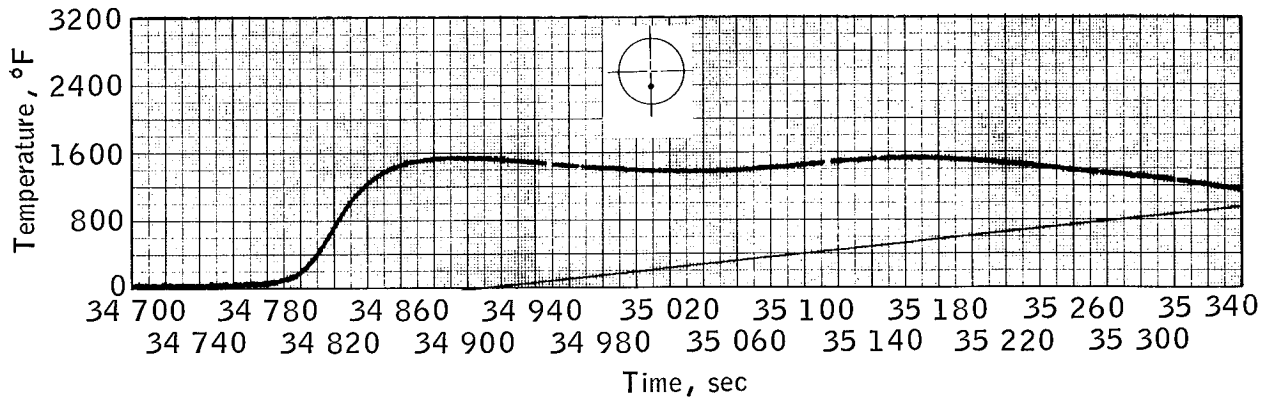


(j) Top wafer of $Y_c = -4.74$ in., $Z_c = -50.0$ in., $S/R = -0.663$.

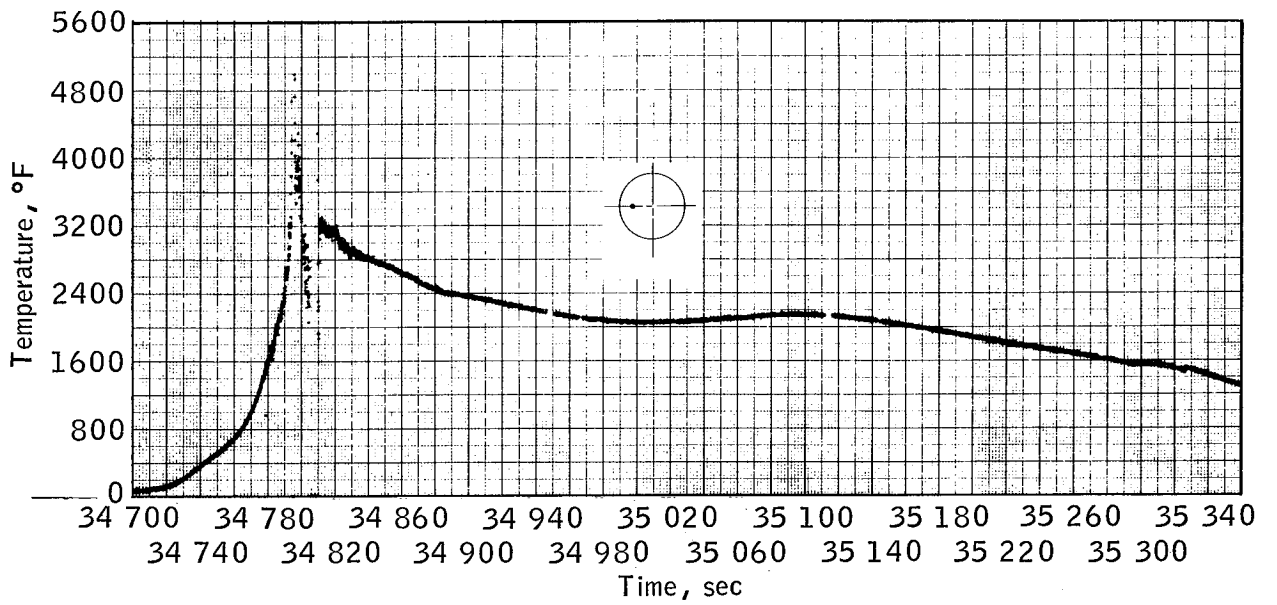


(k) Second wafer of $Y_c = -4.74$ in., $Z_c = -50.0$ in., $S/R = -0.663$.

Figure 15. - Continued.

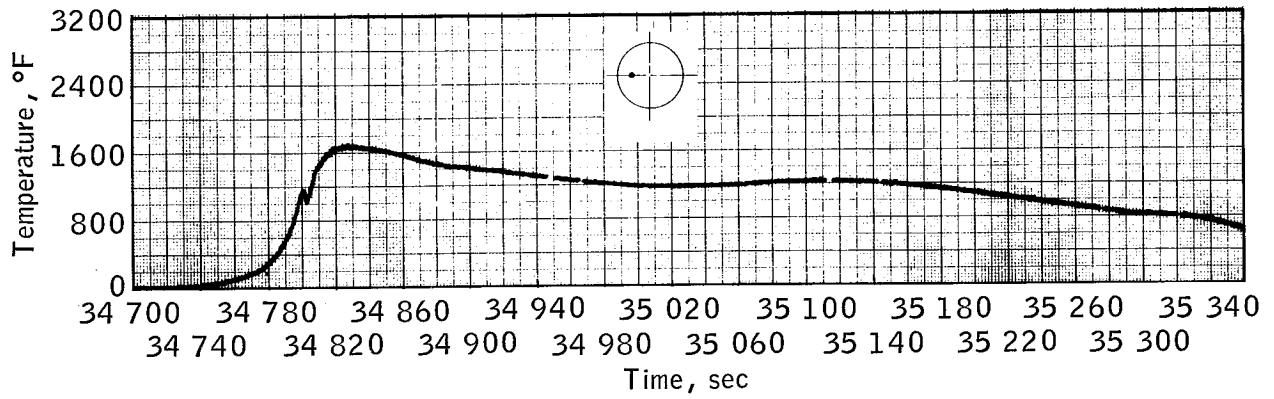


(l) Third wafer of $Y_c = -4.74$ in., $Z_c = -50.0$ in., $S/R = -0.663$.

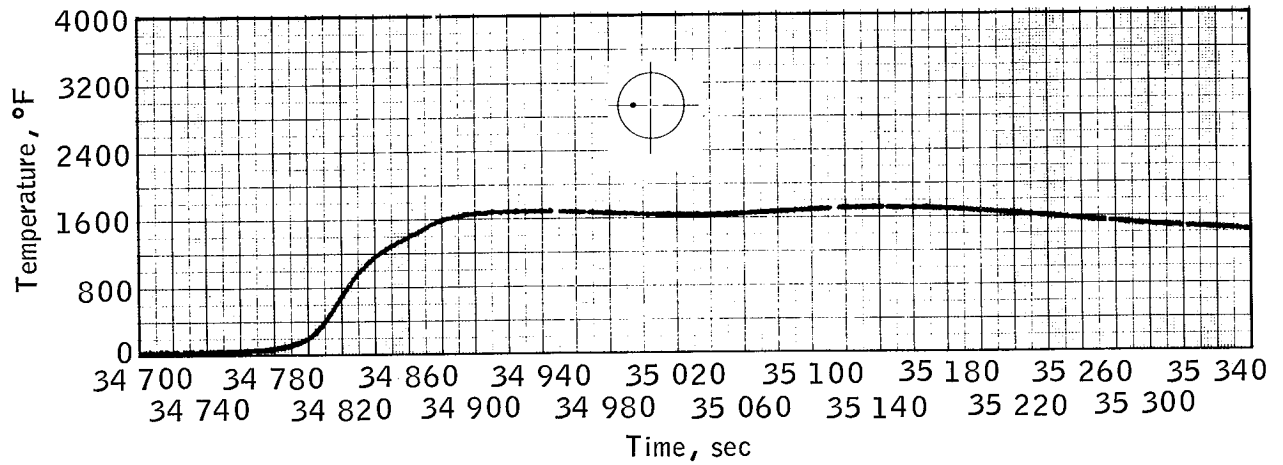


(m) Top wafer of $Y_c = 50.0$ in., $Z_c = -1.5$ in., $S/R = 0.666$, $\theta = 0^\circ$.

Figure 15. - Continued.

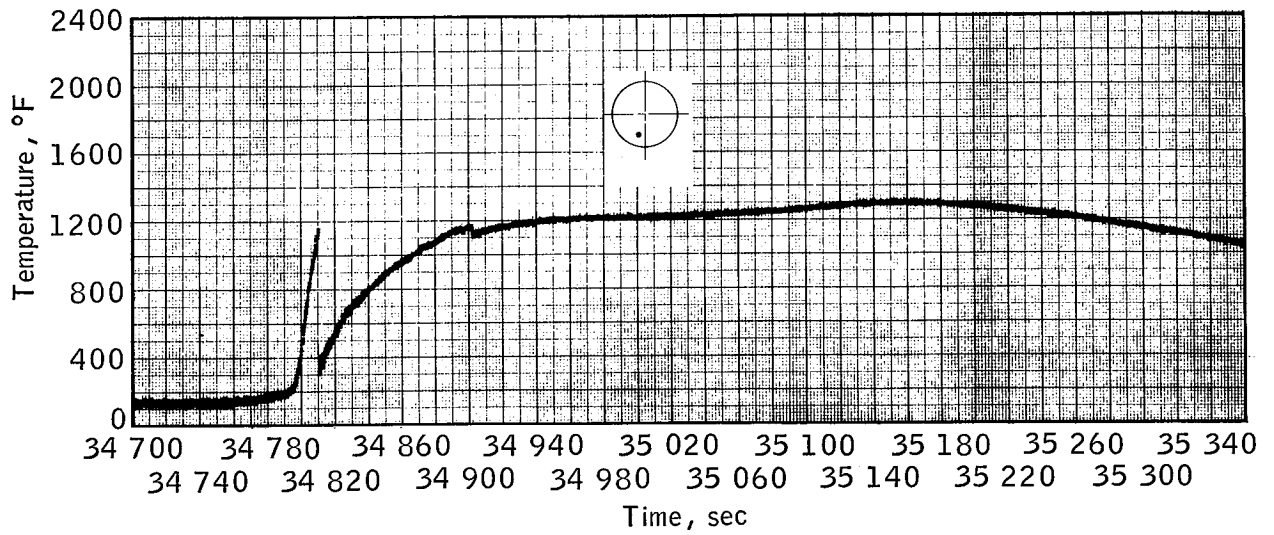


(n) Second wafer of $Y_c = 50.0$ in., $Z_c = -1.5$ in., $S/R = 0.666$, $\theta = 0^\circ$.

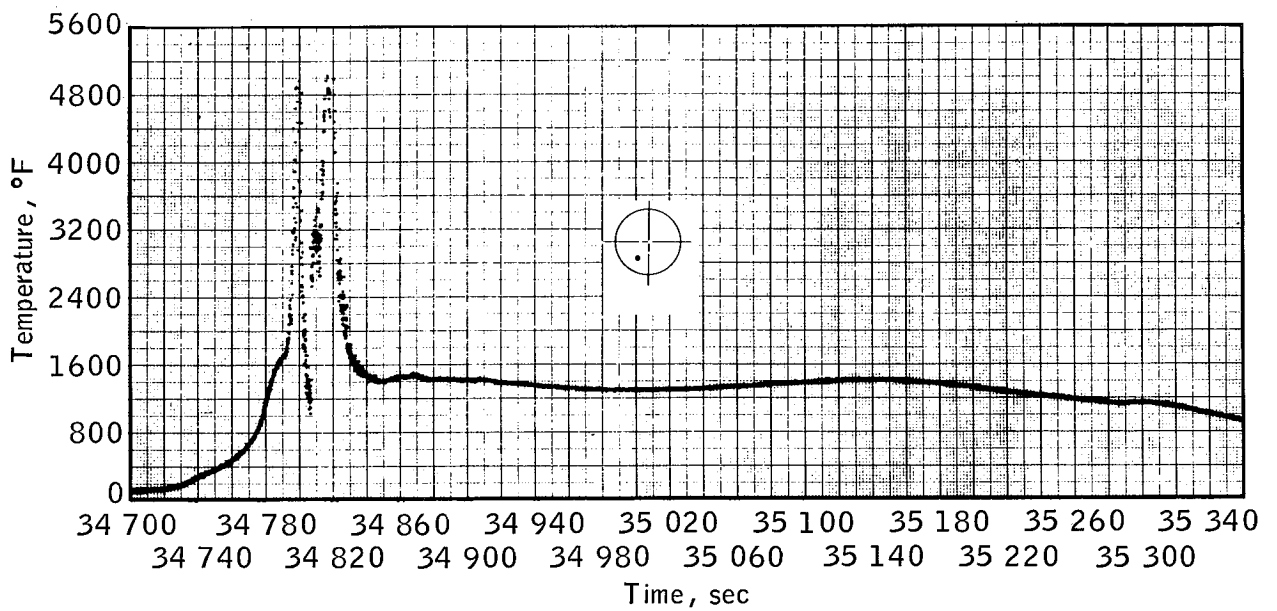


(o) Third wafer of $Y_c = 50.0$ in., $Z_c = -1.5$ in., $S/R = 0.666$, $\theta = 0^\circ$.

Figure 15. - Continued.

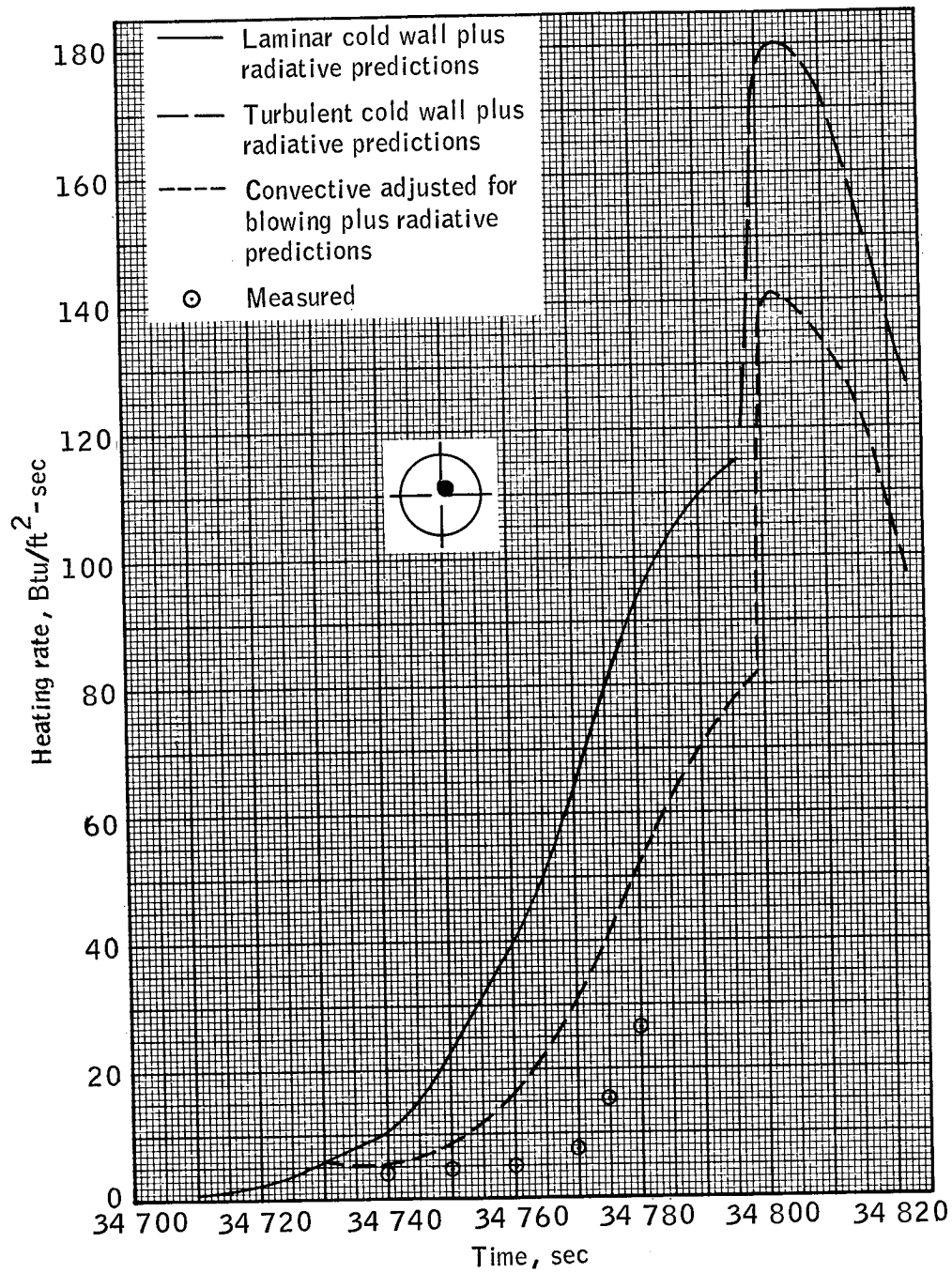


(p) $Y_c = 13.23$ in., $Z_c = -65.18$ in., $S/R = 0.893$.



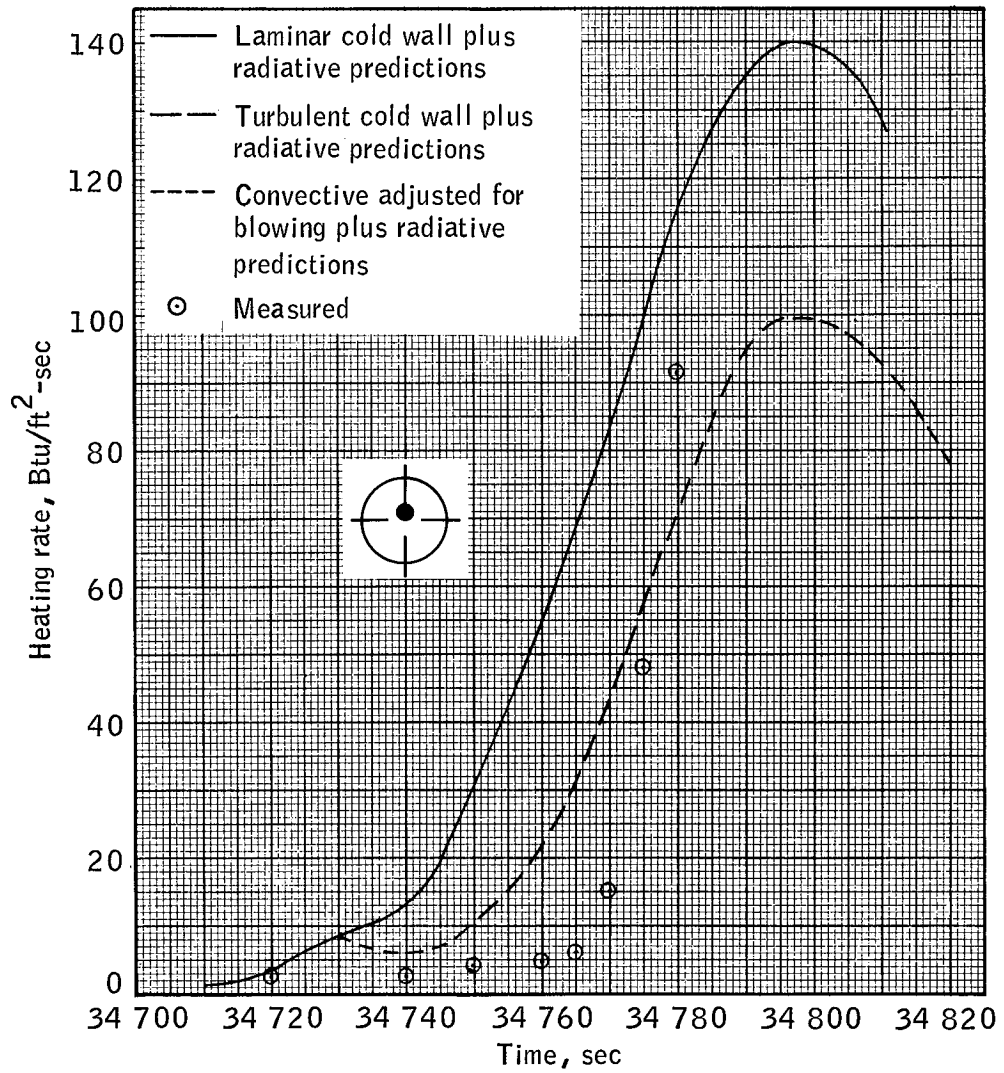
(q) $Y_c = 12.73$ in., $Z_c = -49.47$ in., $S/R = -0.673$.

Figure 15. - Concluded.



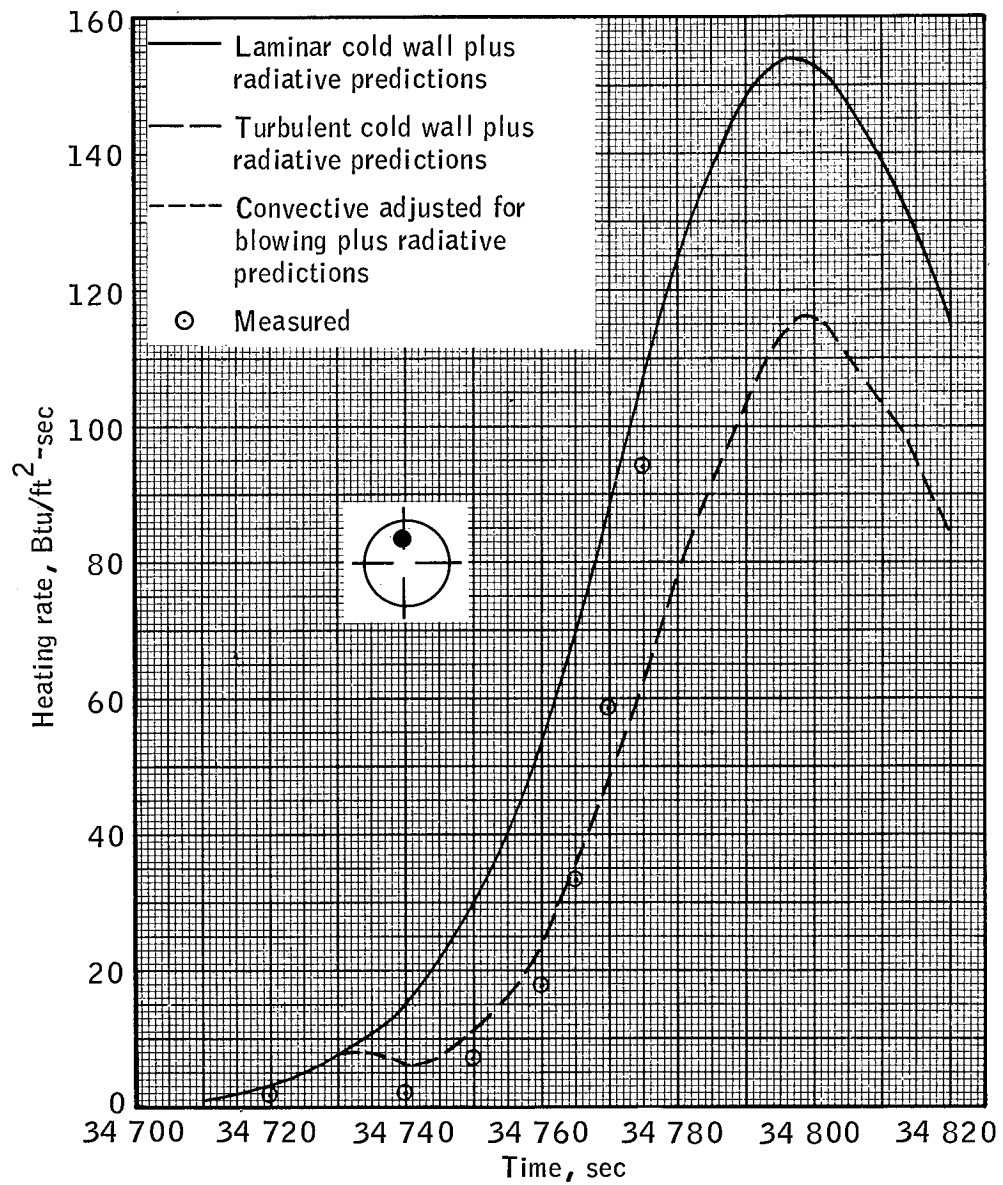
(a) $Y_c = -0.48$ in., $Z_c = 0.48$ in., $S/R = 0.004$.

Figure 16. - Heating rates calculated from wafer calorimeter temperature measurements on spacecraft 020.



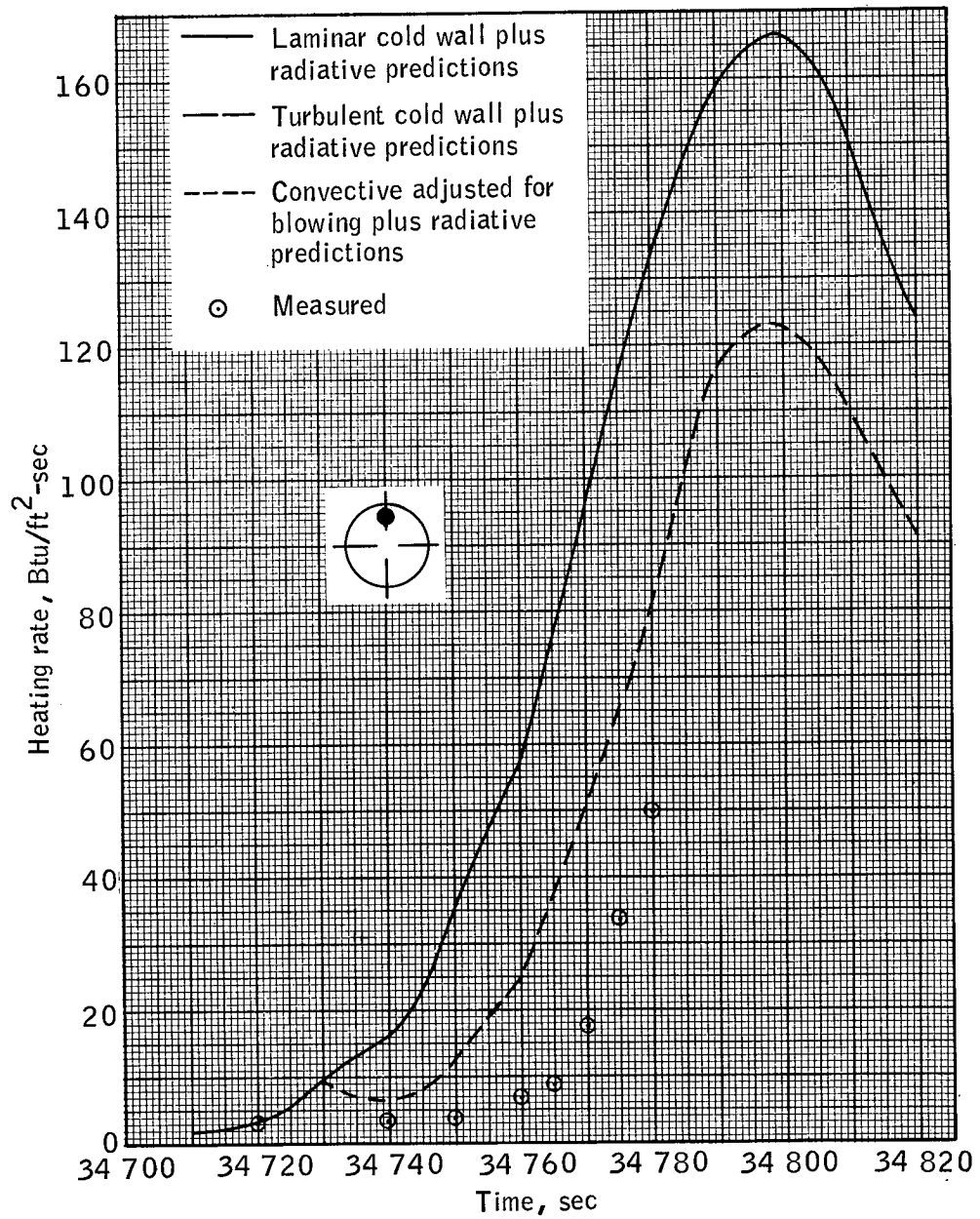
(b) $Y_c = 0$ in., $Z_c = 39.0$ in., $S/R = 0.512$.

Figure 16. - Continued.



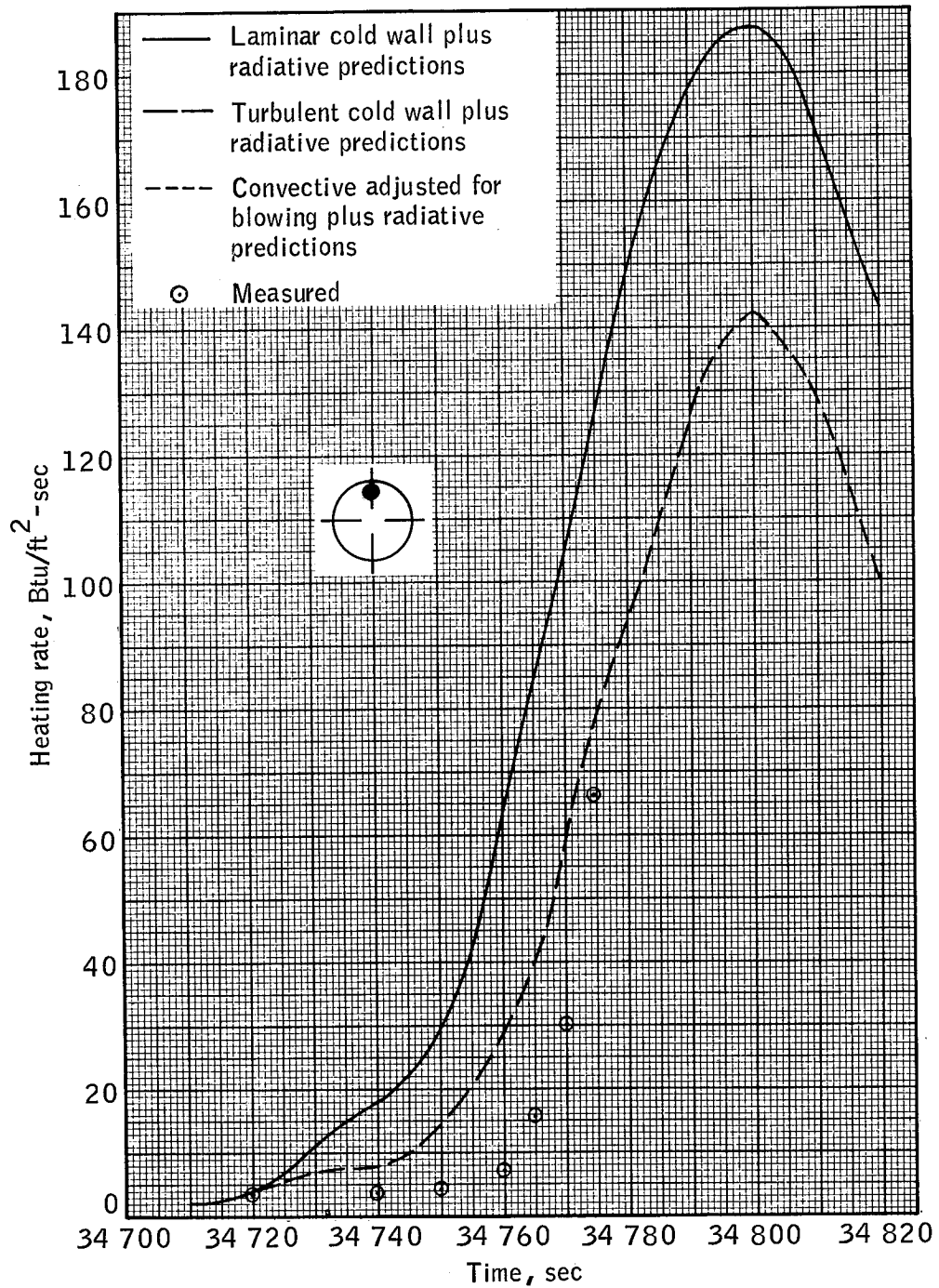
(c) $Y_c = 4.23$ in., $Z_c = 55.16$ in., $S/R = 0.732$.

Figure 16. - Continued.



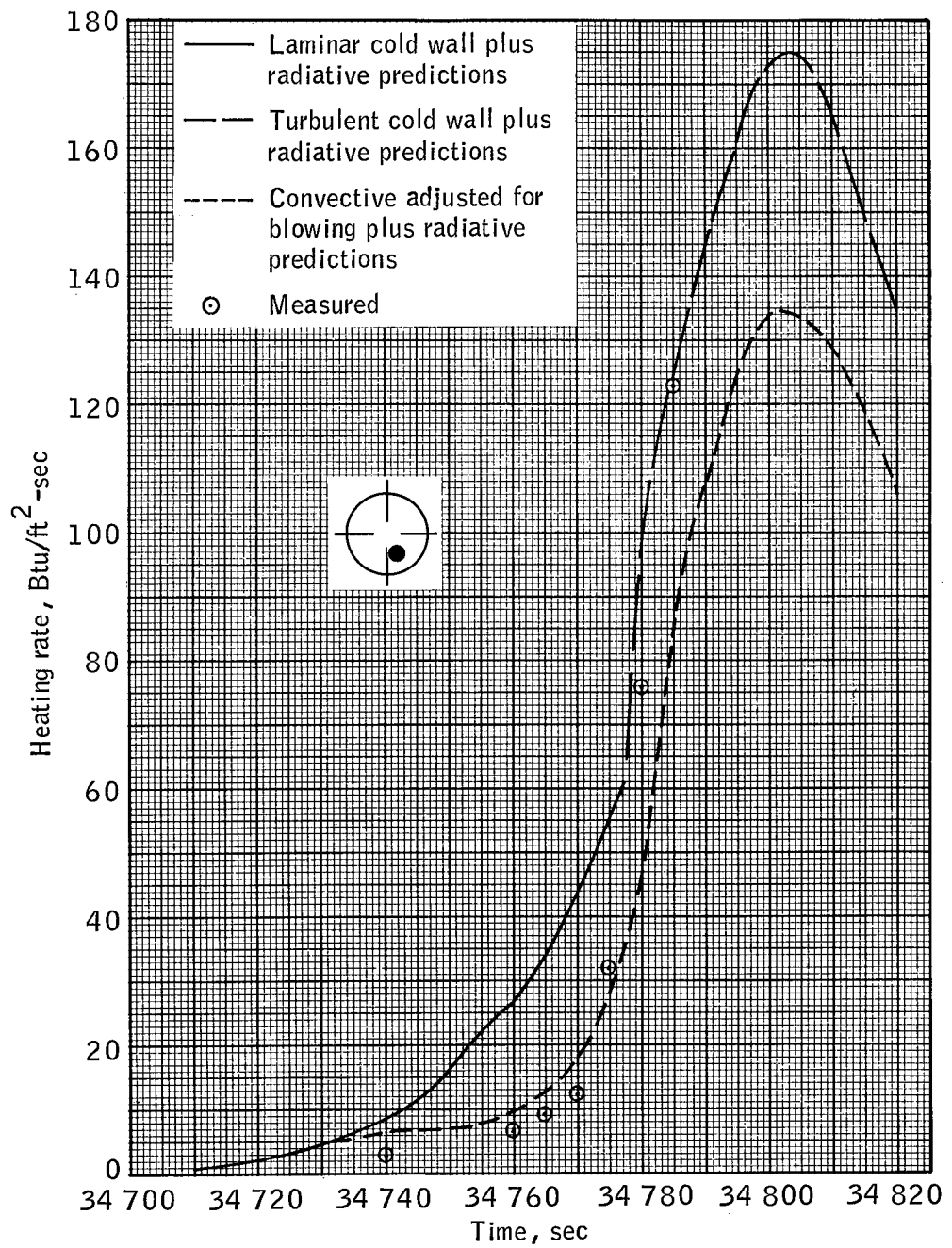
(d) $Y_c = 0$ in., $Z_c = 65.0$ in., $S/R = 0.865$.

Figure 16. - Continued.



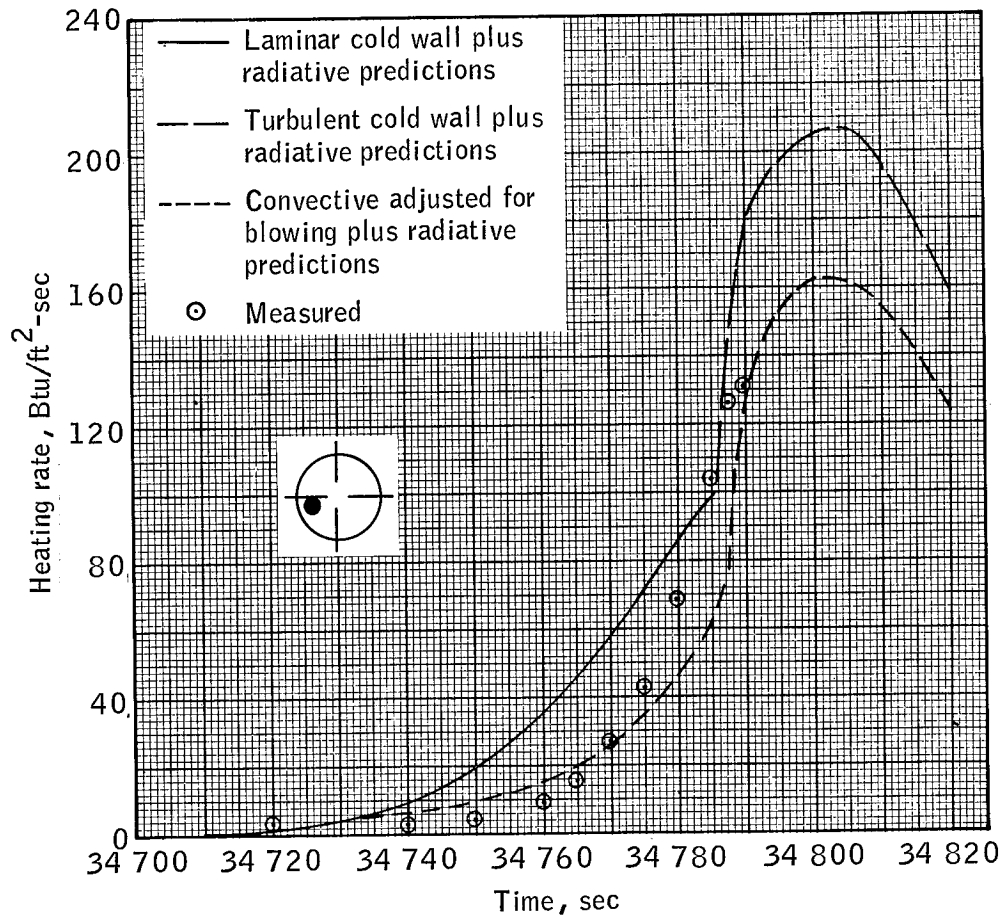
(e) $Y_c = 4.01$ in., $Z_c = 71.72$ in., $S/R = 0.969$.

Figure 16. - Continued.



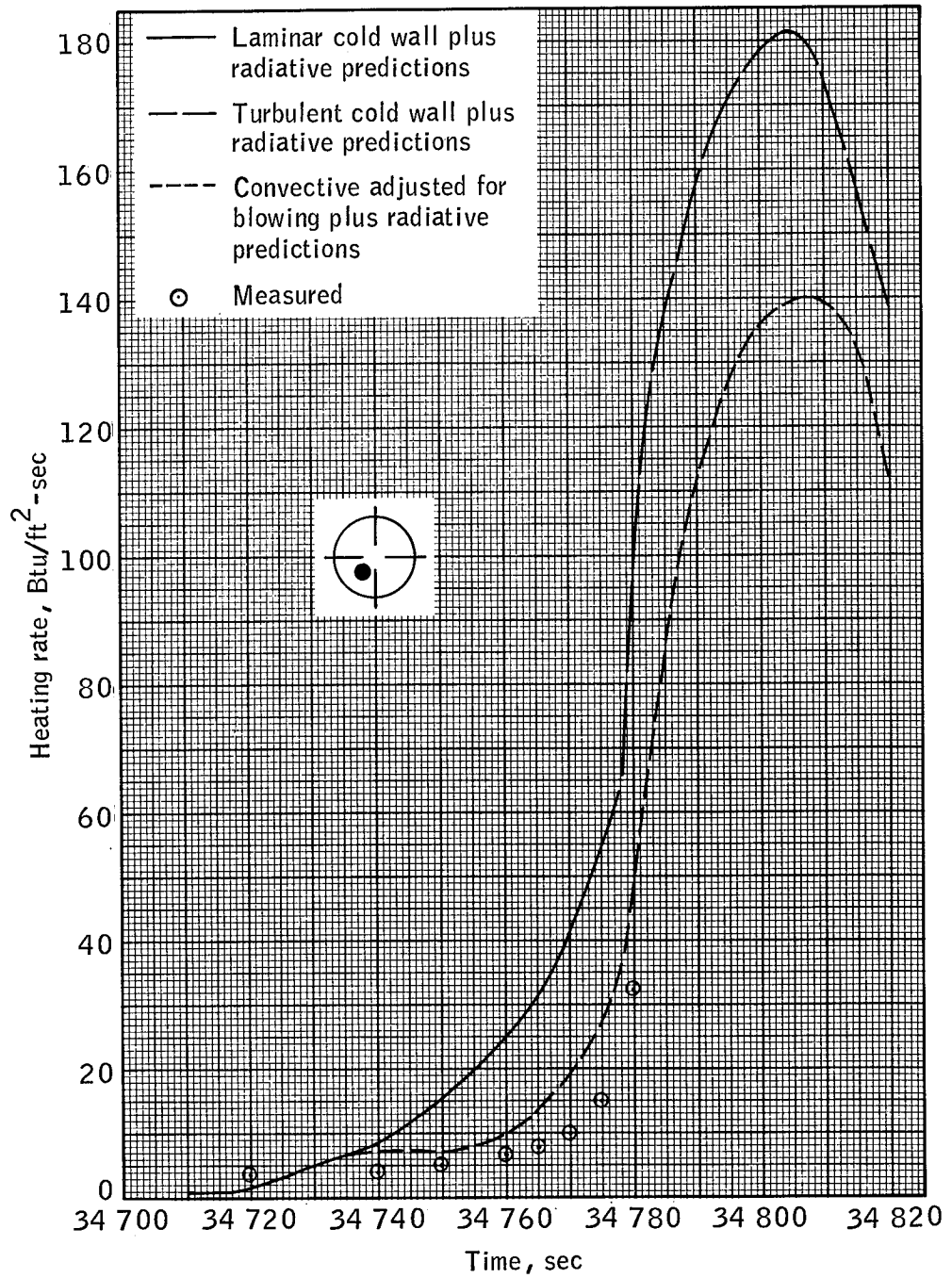
(f) $Y_c = -4.74$ in., $Z_c = -50.0$ in., $S/R = -0.663$.

Figure 16. - Continued.



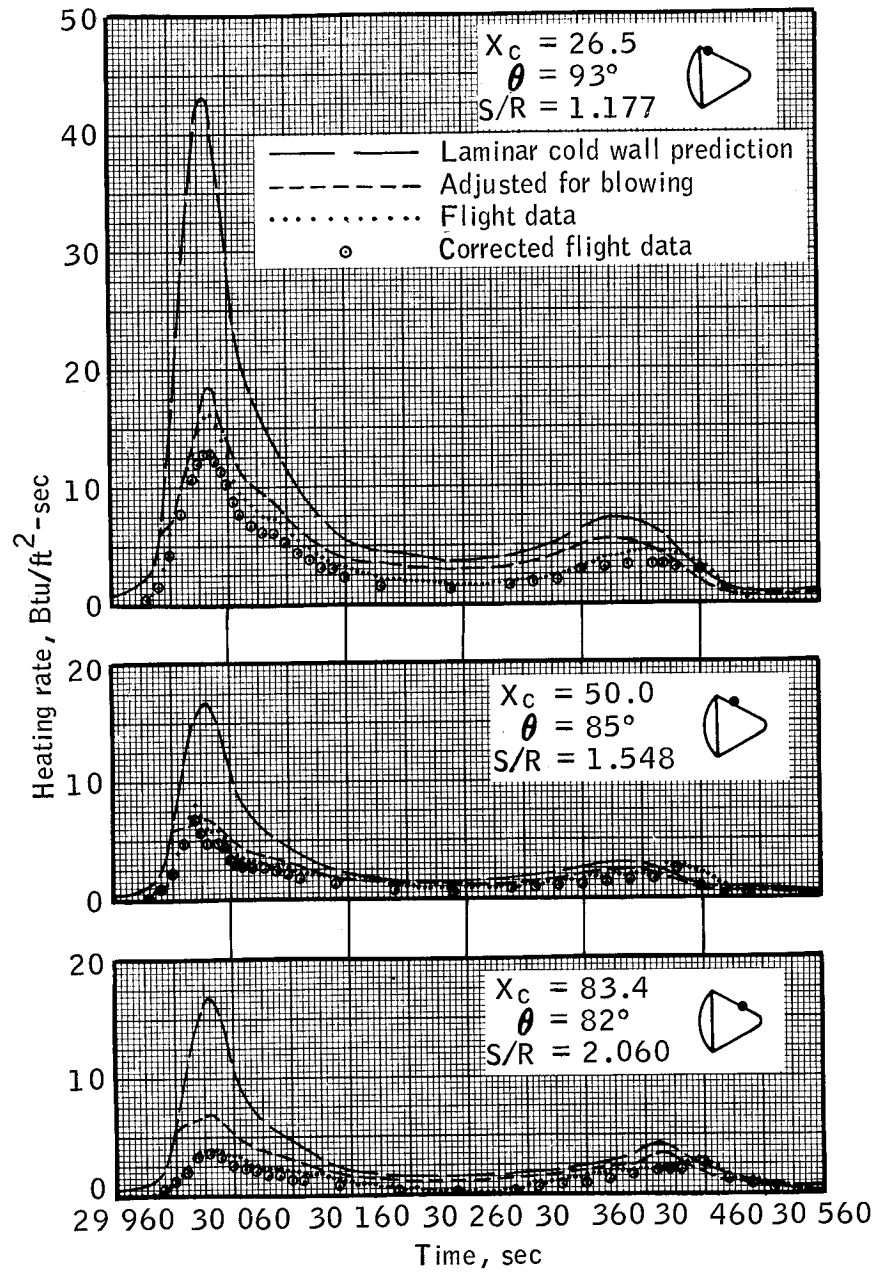
(g) $Y_c = 50.0$ in., $Z_c = -1.5$ in., $S/R = 0.666$, $\theta = 0^\circ$.

Figure 16. - Continued.



(h) $Y_c = 12.73$ in., $Z_c = -49.47$ in., $S/R = -0.673$, $\theta = 284^\circ$.

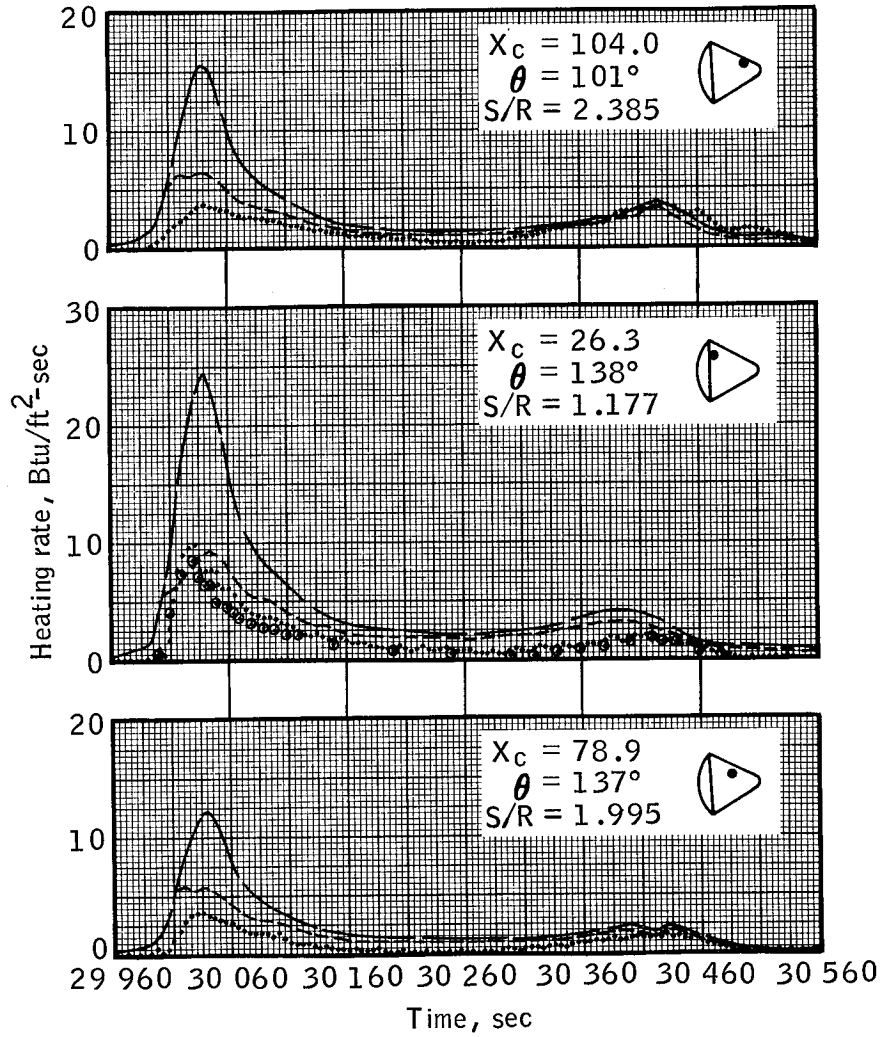
Figure 16. - Concluded.



(a) Windward conical section.

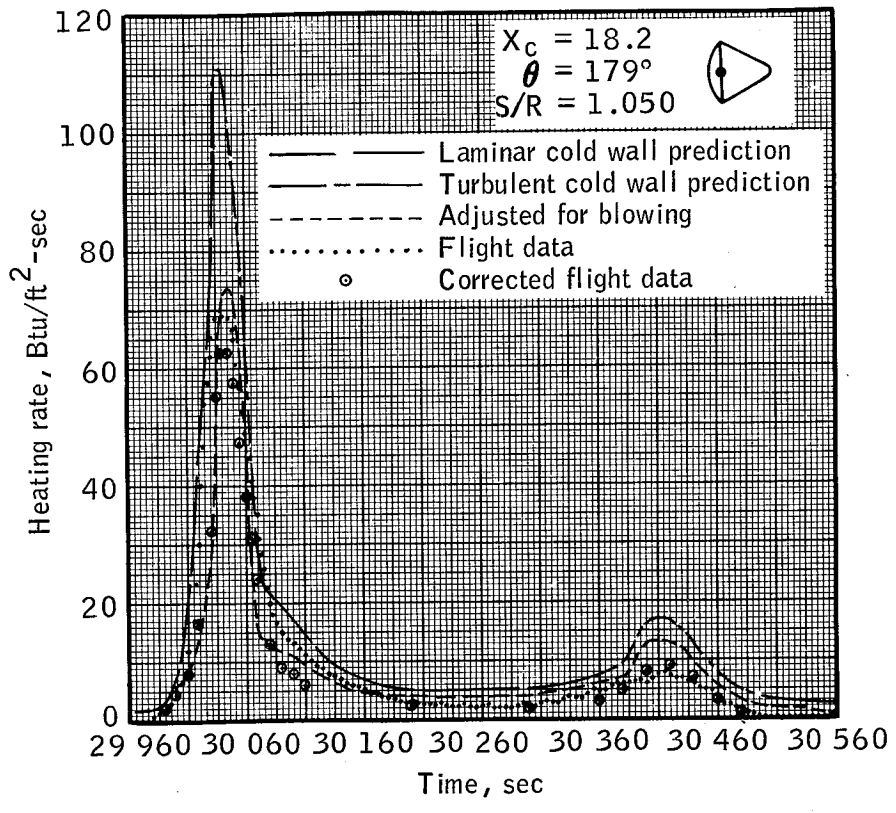
Figure 17. - Asymptotic calorimeter measurements on spacecraft 017 compared with theoretical predictions.

- — — — — Laminar cold wall prediction
- - - - - Adjusted for blowing
- Flight data
- Corrected flight data



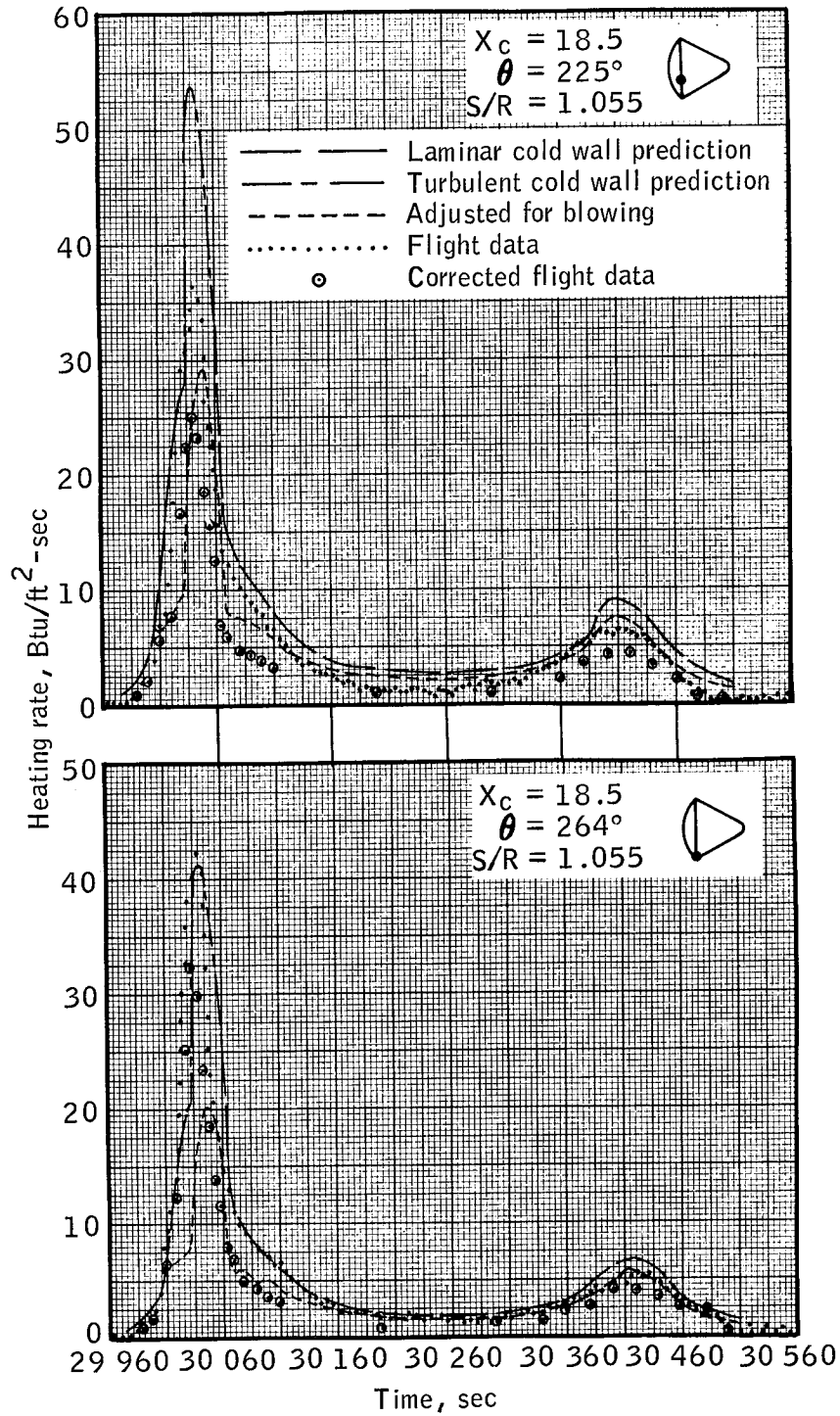
(a) Concluded.

Figure 17. - Continued.



(b) Toroid.

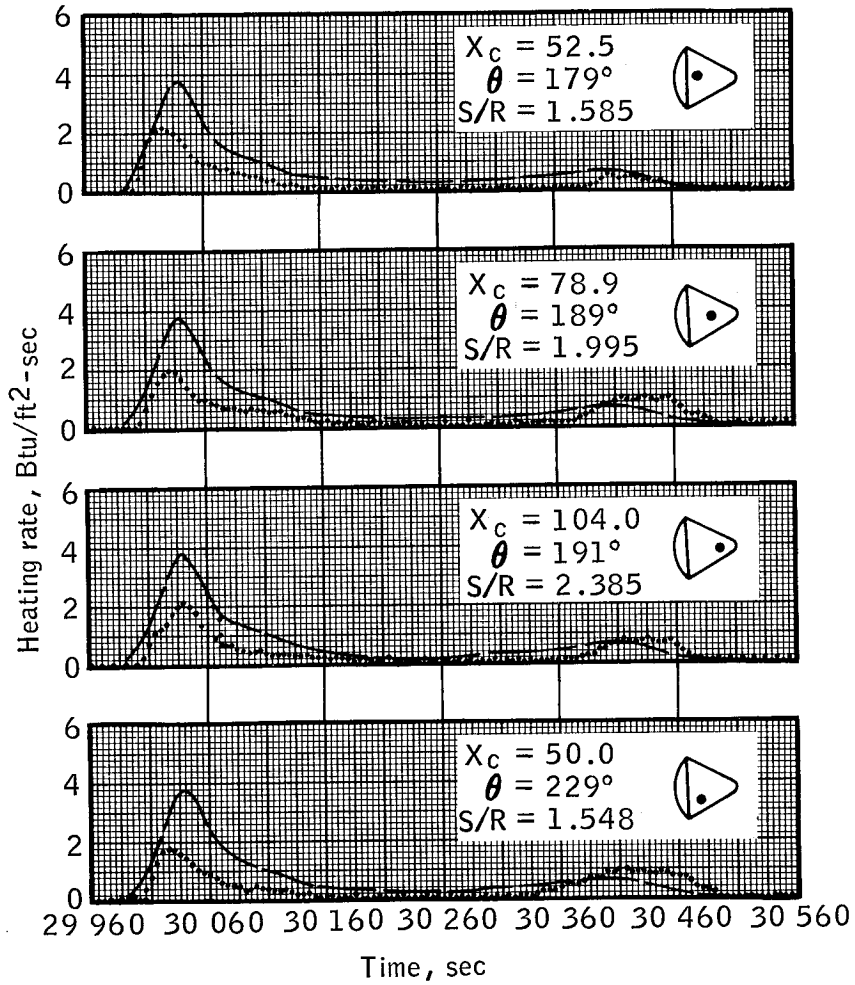
Figure 17. - Continued.



(b) Concluded.

Figure 17. - Continued.

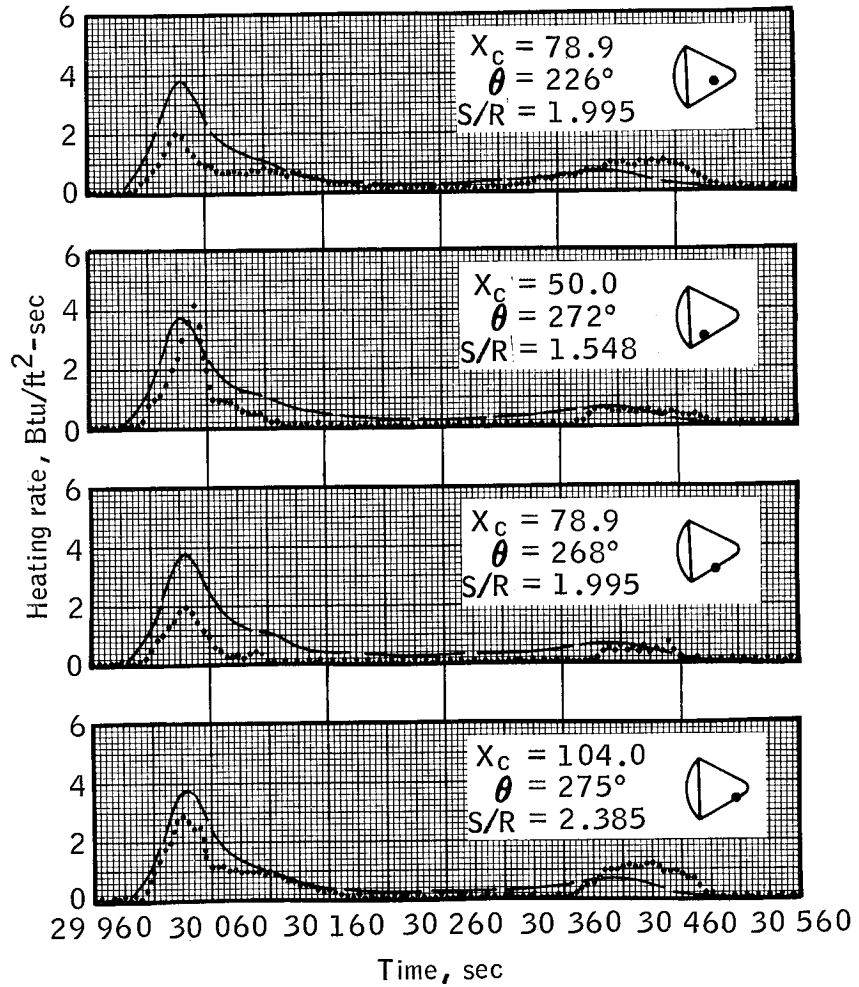
— — — Laminar cold wall prediction
 Flight data



(c) Leeward conical section.

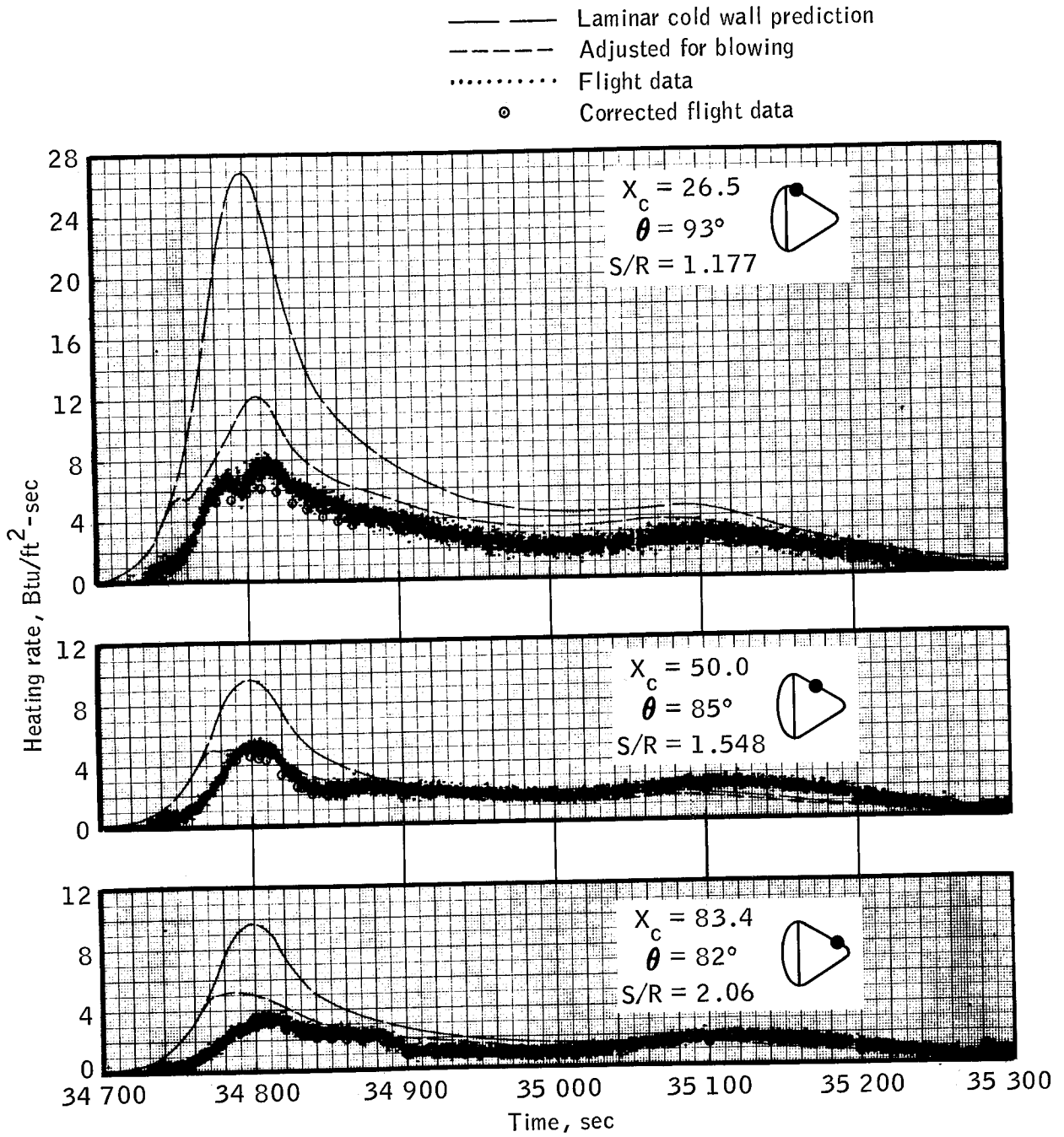
Figure 17. - Continued.

—— Laminar cold wall prediction
 Flight data



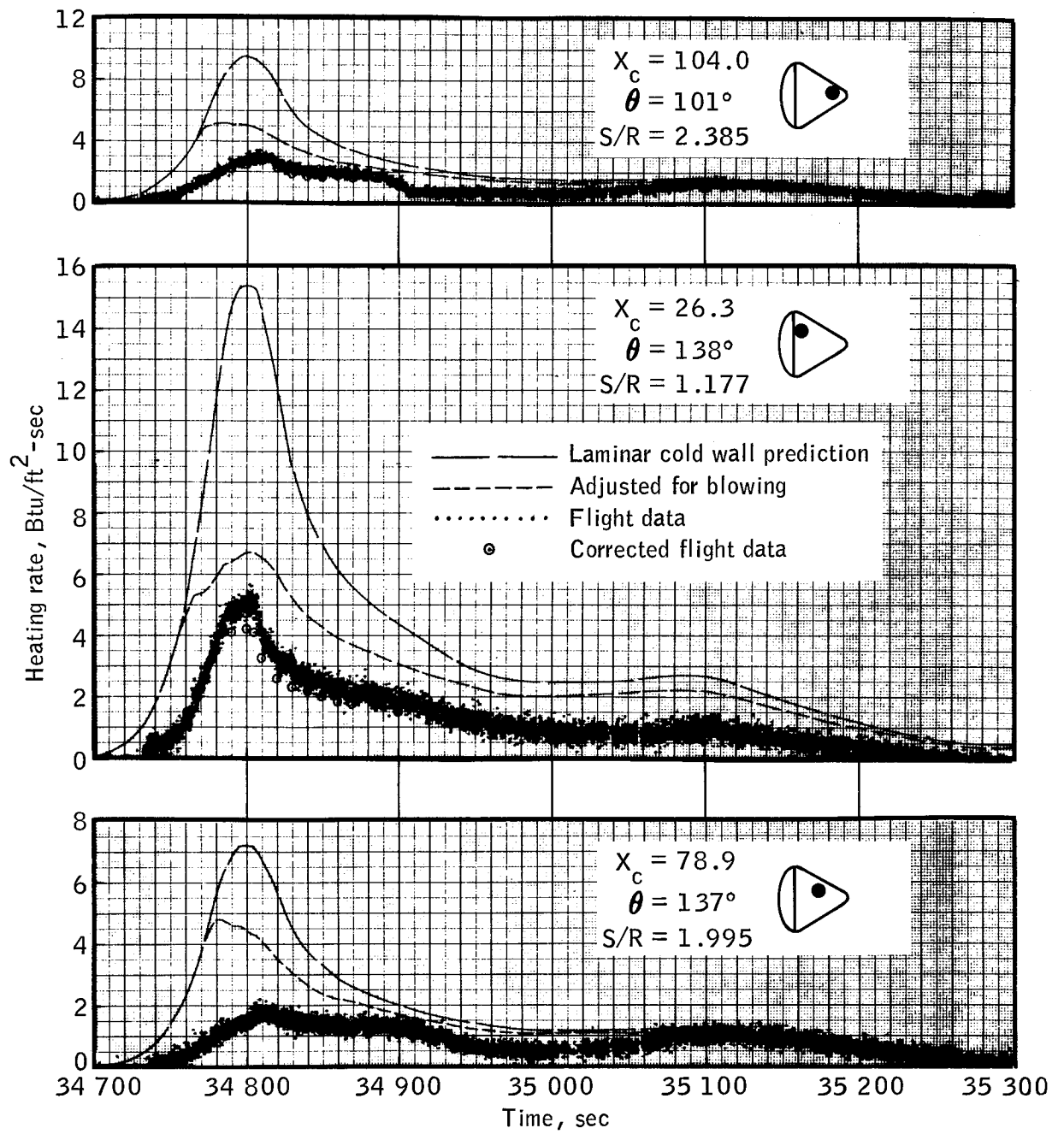
(c) Concluded.

Figure 17. - Concluded.



(a) Windward conical section.

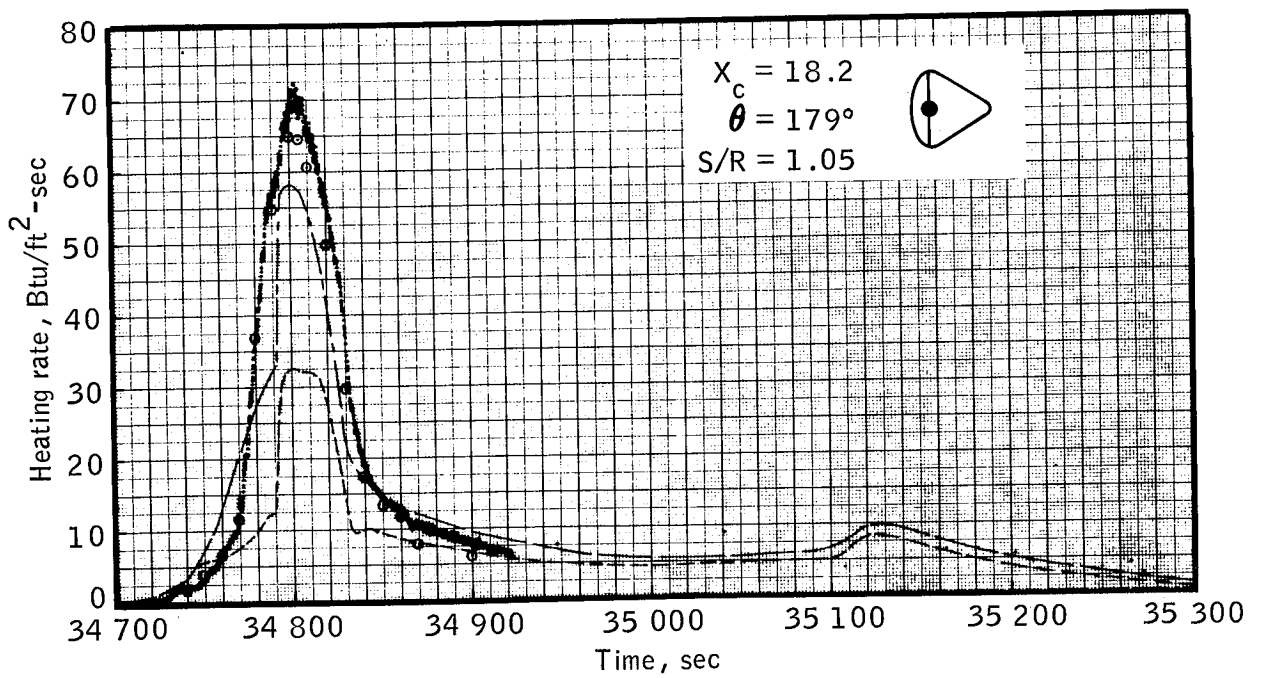
Figure 18. - Asymptotic calorimeter measurements on spacecraft 020 compared with theoretical predictions.



(a) Concluded.

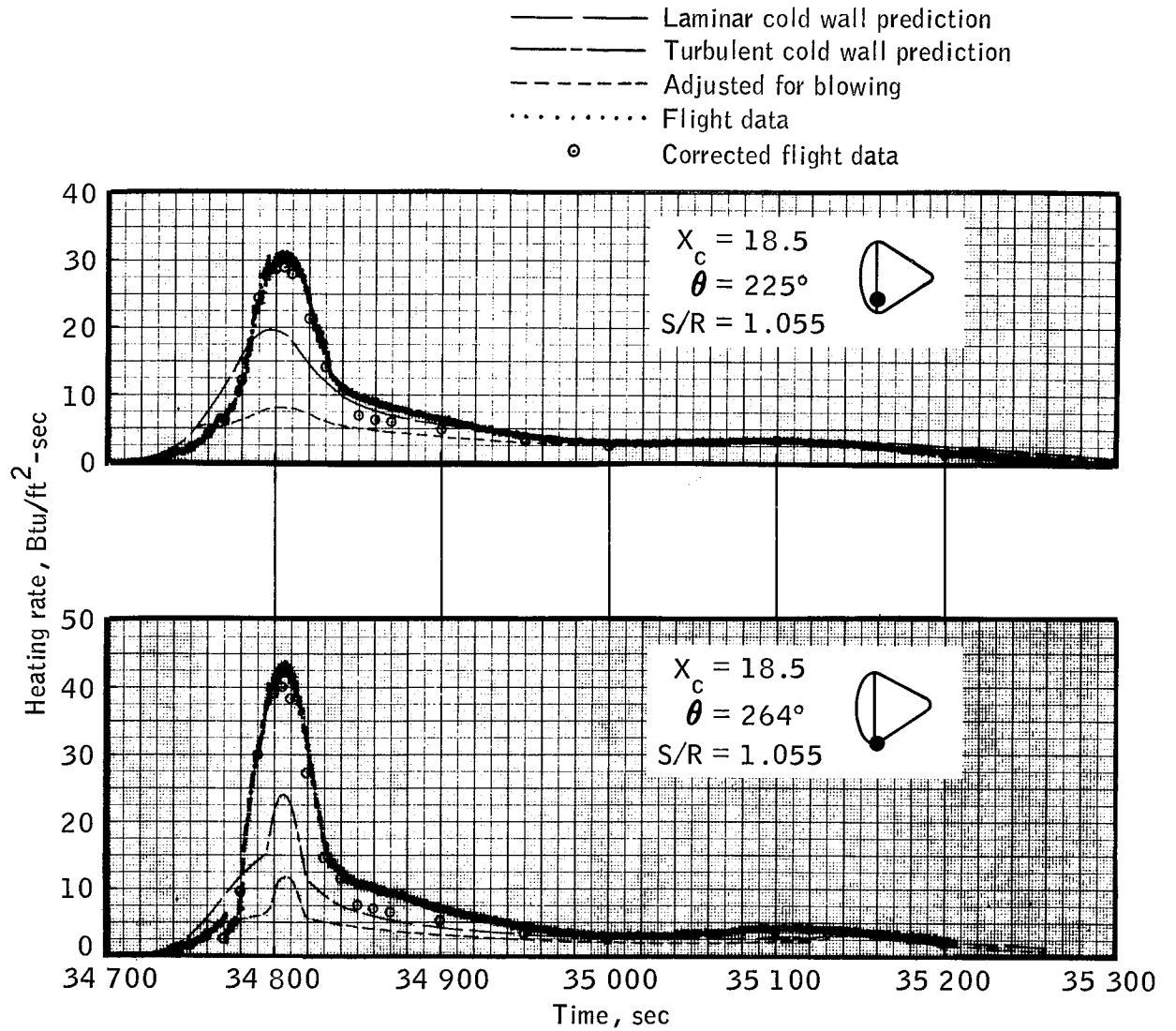
Figure 18. - Continued.

- Laminar cold wall prediction
- Turbulent cold wall prediction
- - - - Adjusted for blowing
- Flight data
- Corrected flight data



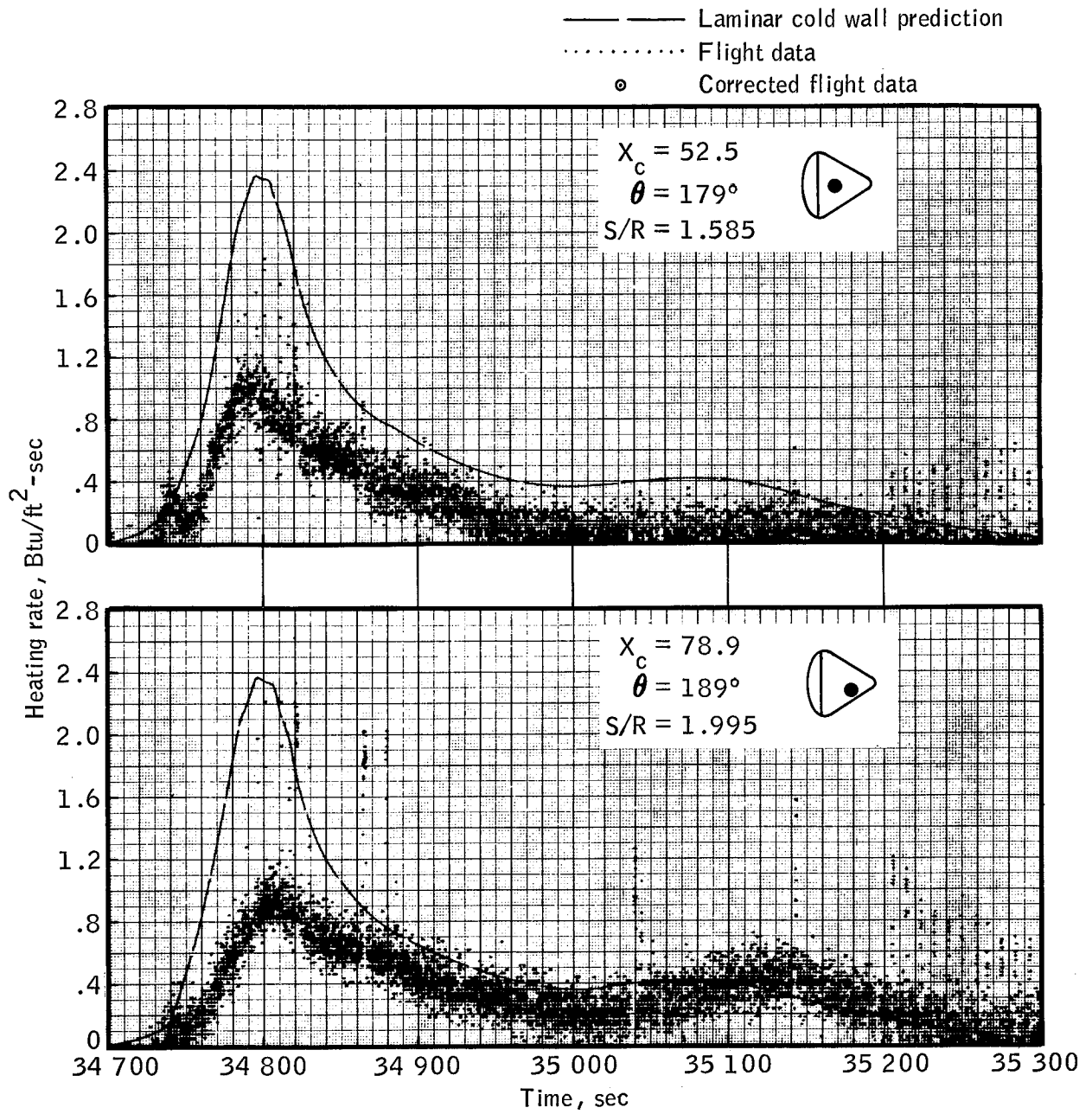
(b) Toroid.

Figure 18. - Continued.



(b) Concluded.

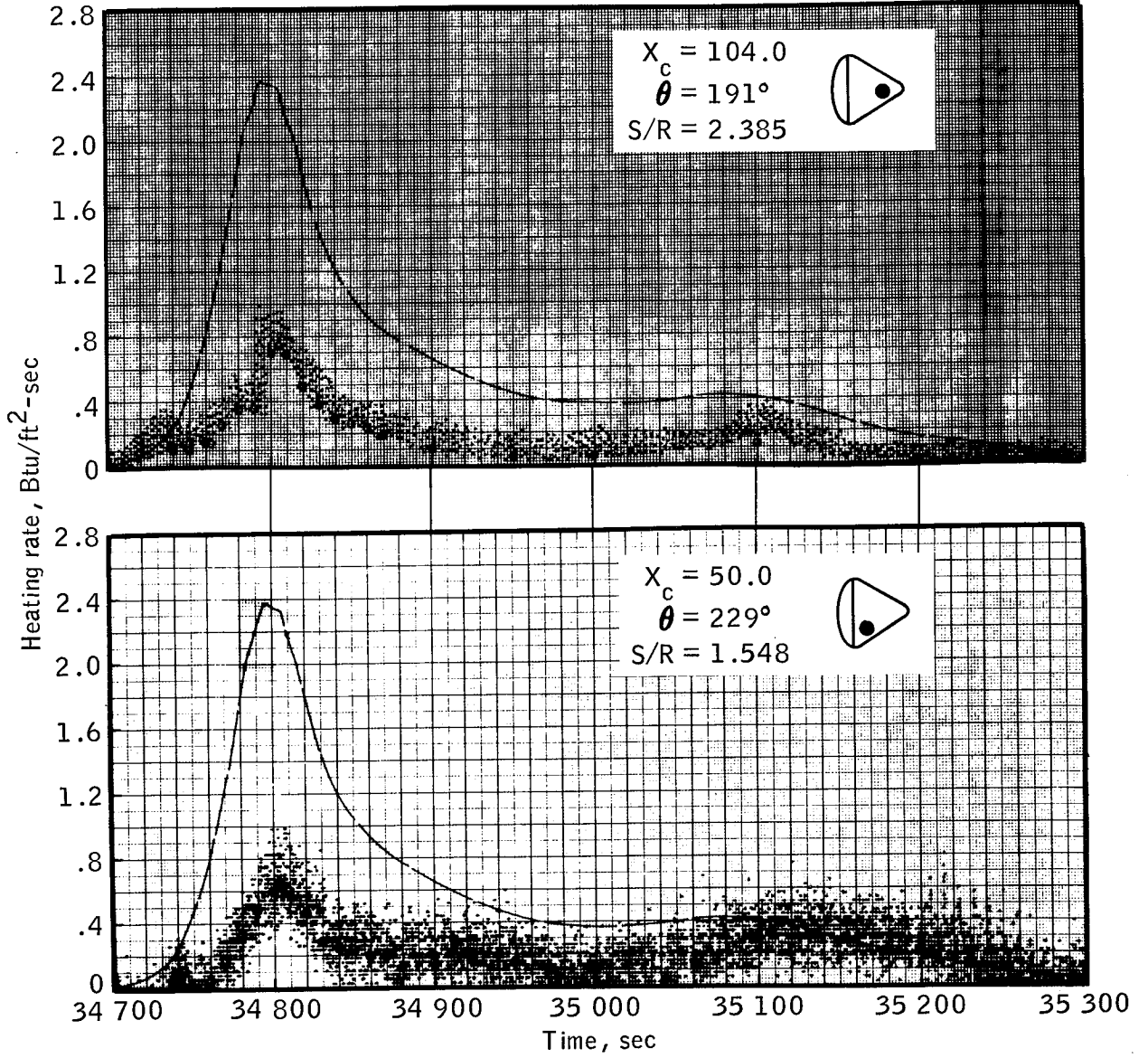
Figure 18. - Continued.



(c) Leeward conical section.

Figure 18. - Continued.

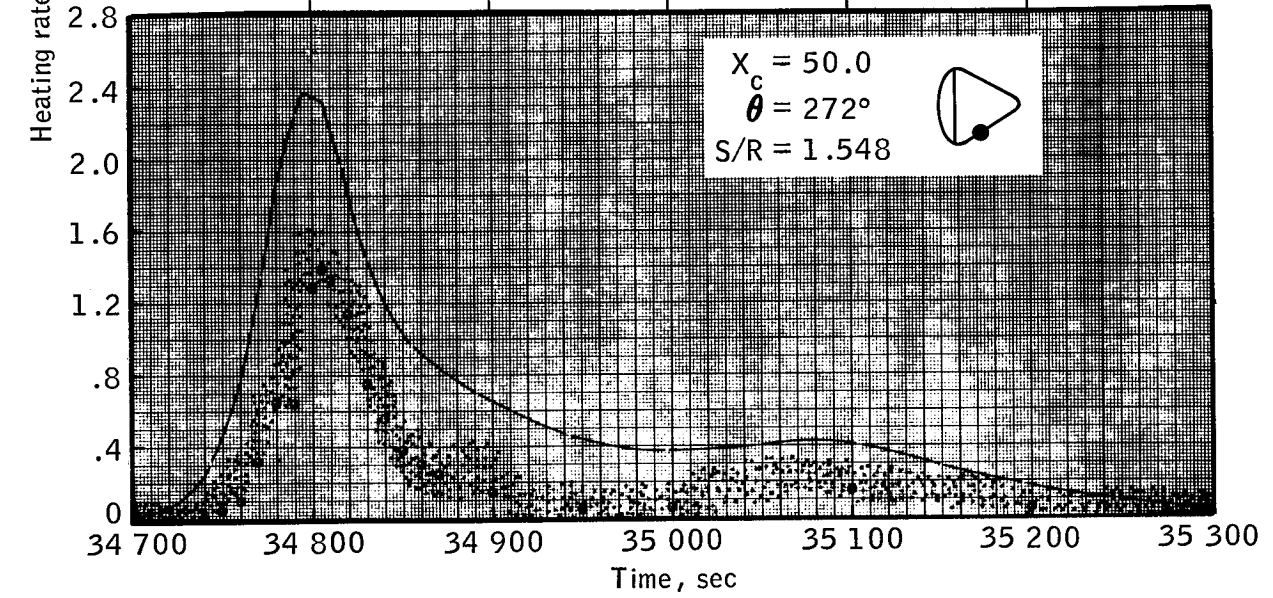
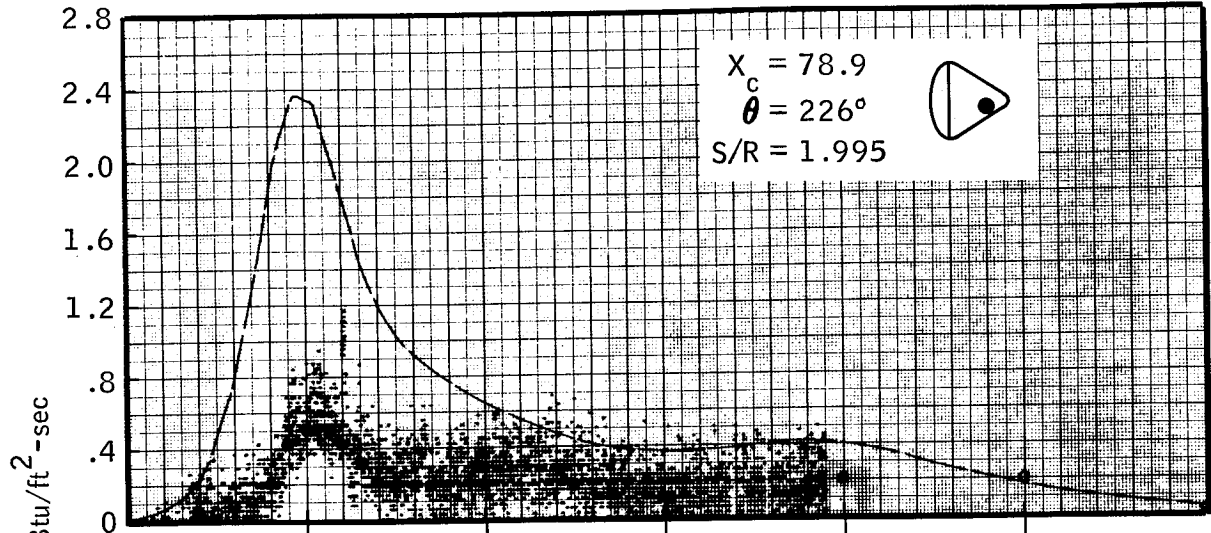
———— Laminar cold wall prediction
 Flight data
 ○ Corrected flight data



(c) Continued.

Figure 18. - Continued.

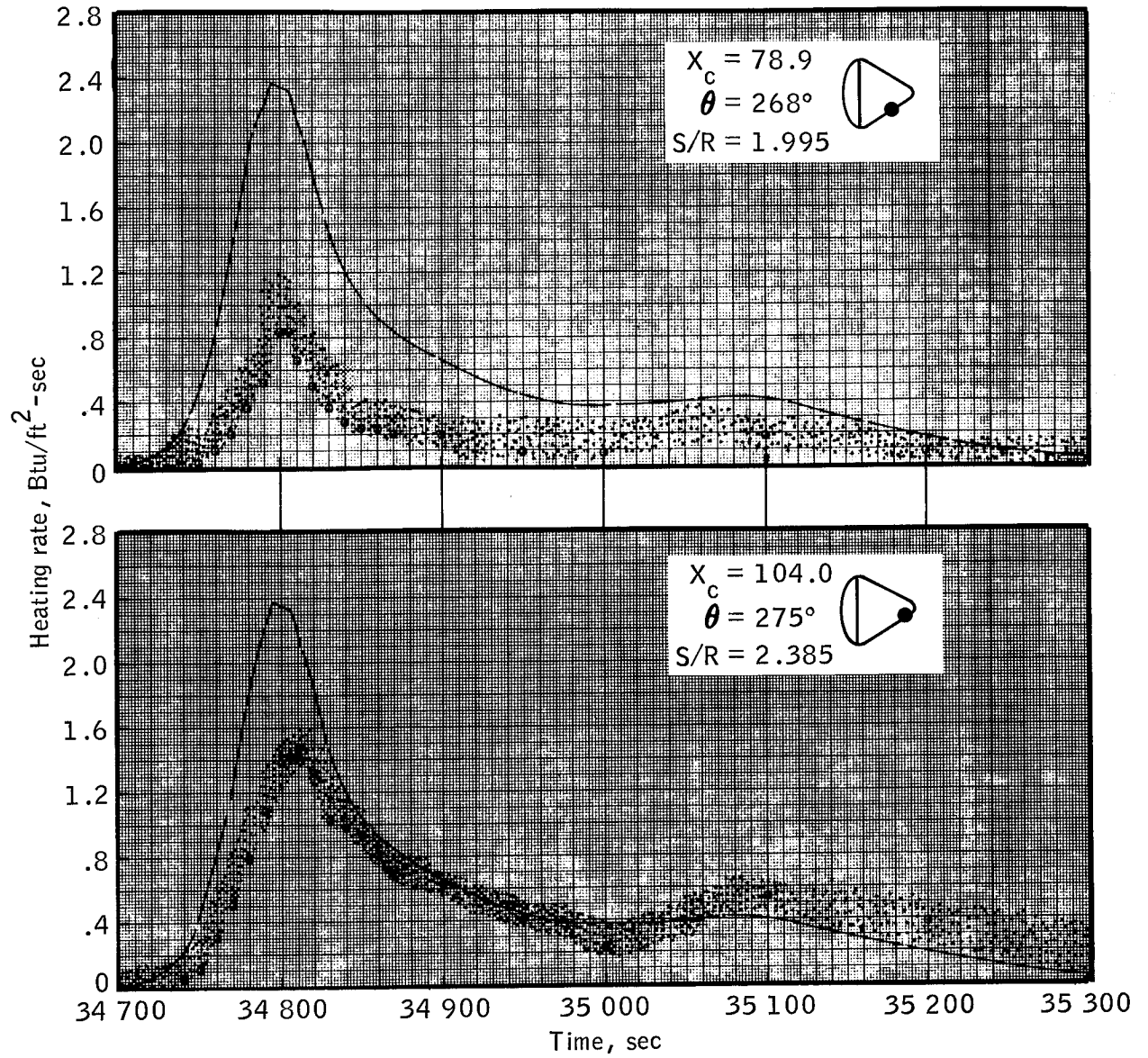
——— Laminar cold wall prediction
 Flight data
 ○ Corrected flight data



(c) Continued.

Figure 18. - Continued.

——— Laminar cold wall prediction
 Flight data
 ◦ Corrected flight data



(c) Concluded.

Figure 18. - Concluded.

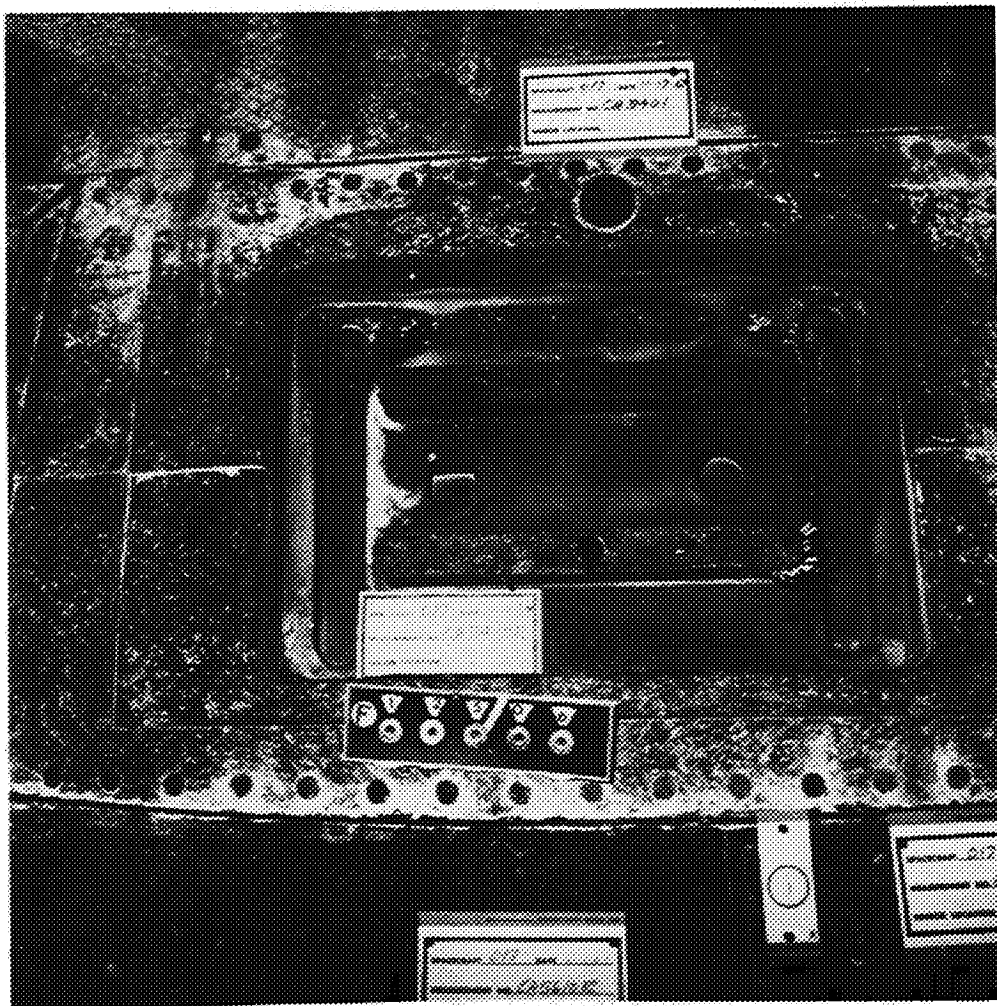


Figure 19. - Photograph of dummy umbilical on spacecraft 017.

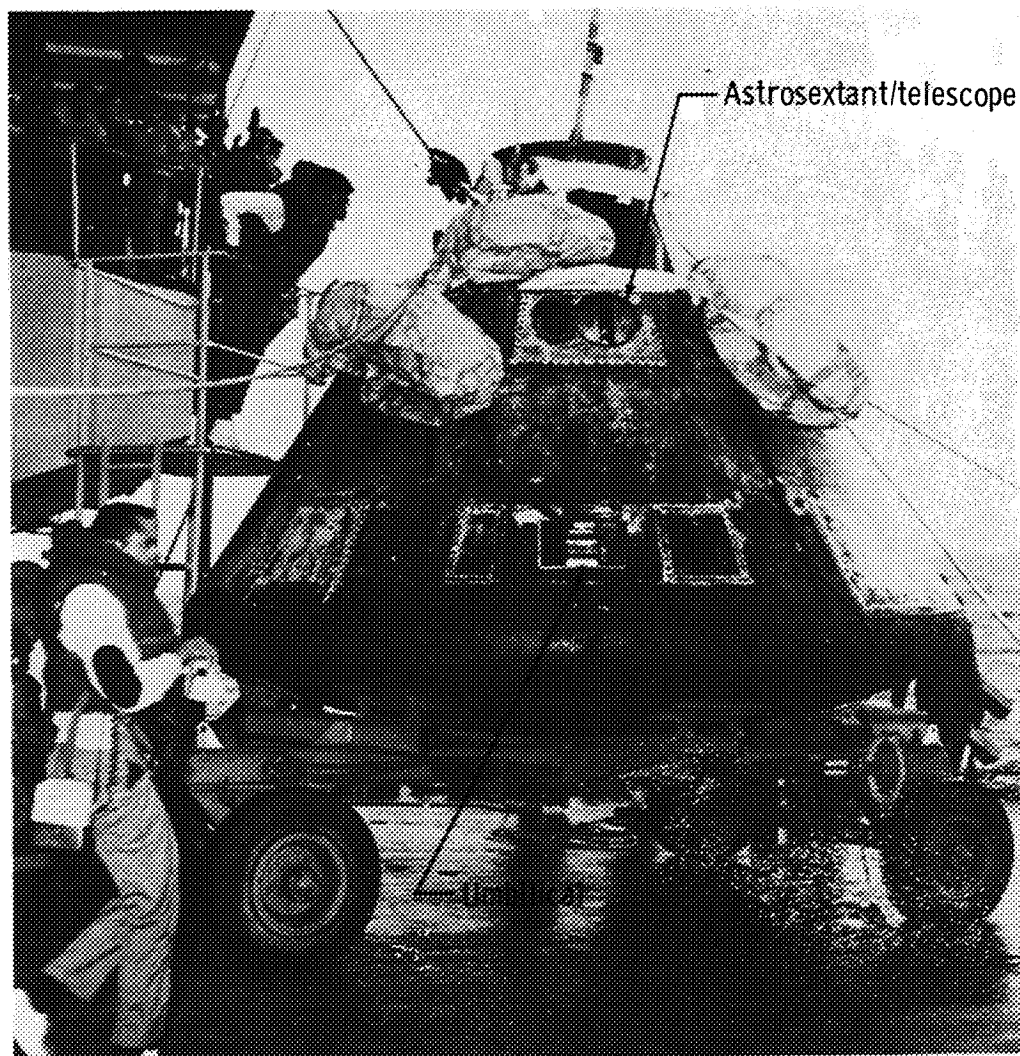
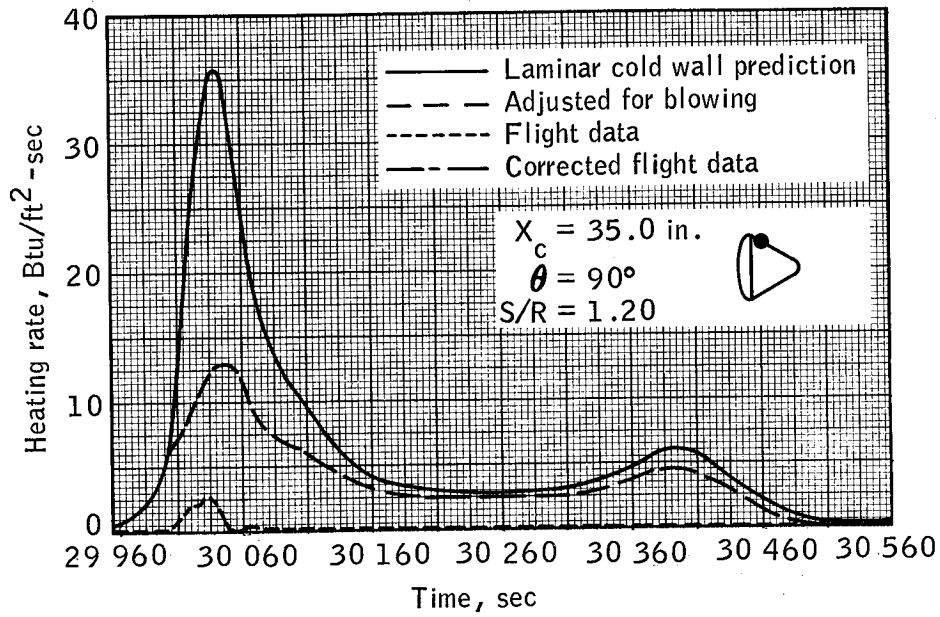
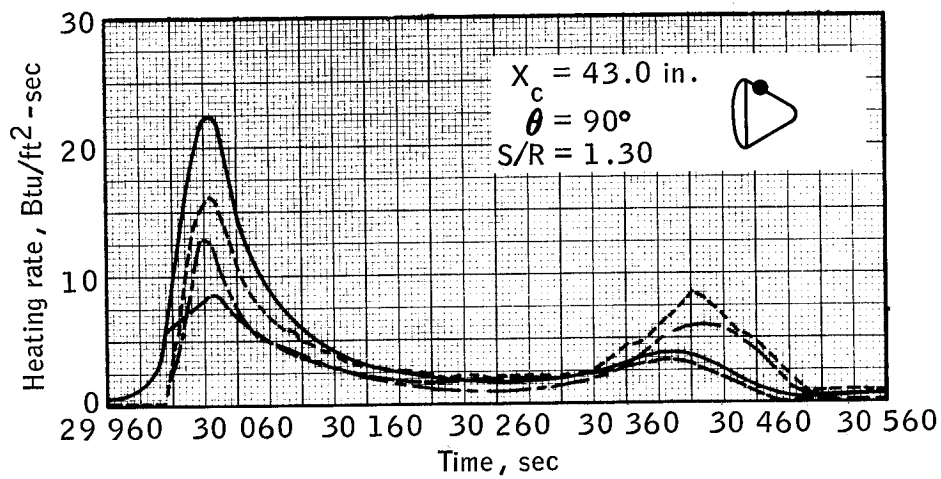


Figure 20. - Photograph of recovered spacecraft 020 showing umbilical and astro sextant.

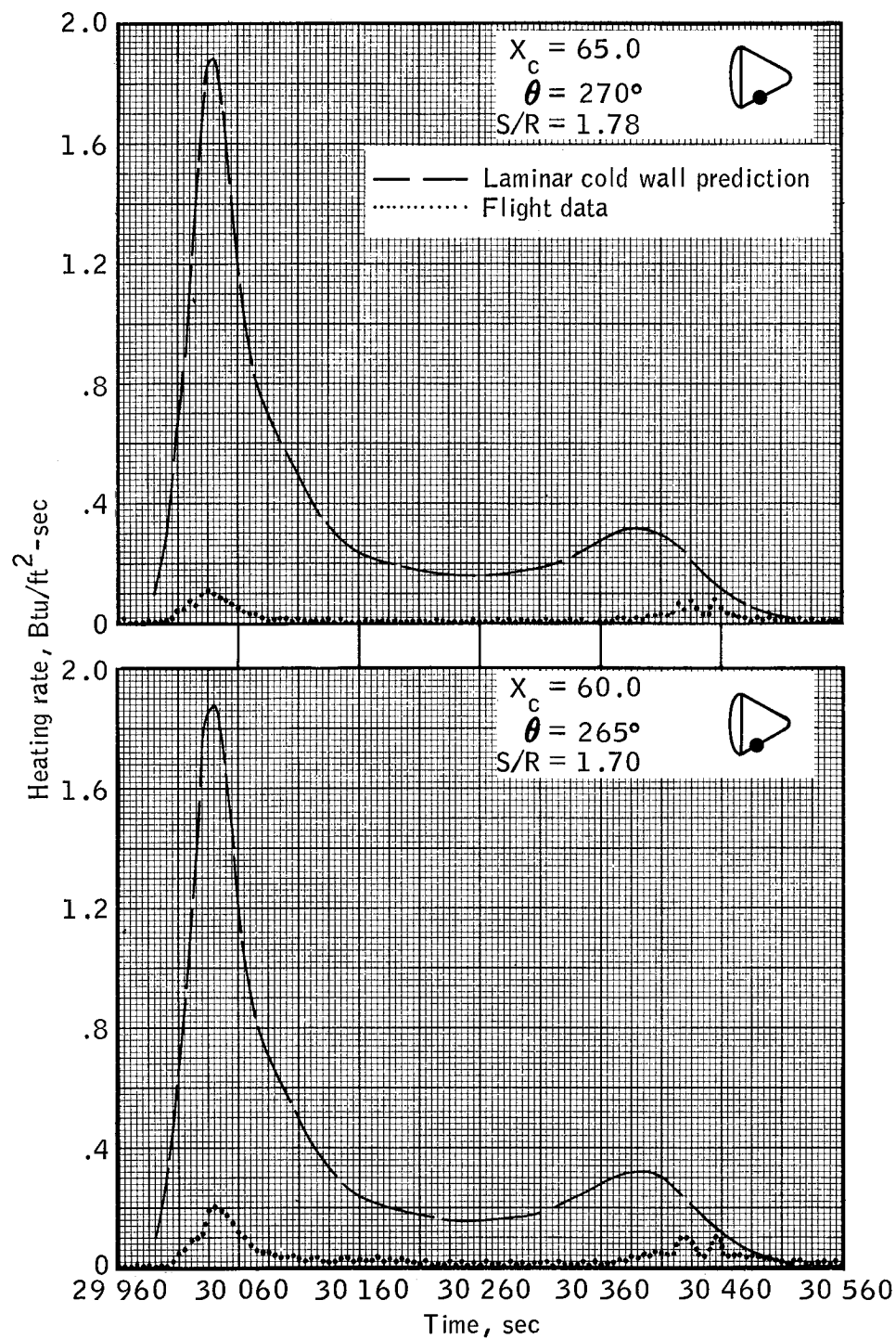


(a) Umbilical cavity.



(b) Umbilical frame.

Figure 21. - Heating-rate measurements on singularities of spacecraft 017.



(c) Hatch gap.

Figure 21. - Concluded.